ABSTRACT

Title of Document: BUOYANCY DRIVEN FLOWS AND HEAT TRANSFER WITHIN A VERTICAL POROUS ANNULUS ENCLOSED IN A CYLINDER.

Rabee Zuberi, M.S., 2011

Directed By: Professor Chandrasekhar Thamire, Department of Mechanical Engineering

Buoyancy driven flows and heat transfer within a vertical porous annulus enclosed in a cylinder are investigated. The inner wall of the annulus is maintained at an isothermal temperature T_c. The study is divided in two sections where the outer and bottom walls are subjected to a uniform heat flux separately. The fluid is assumed to obey the Darcy Law. Finite difference method is used to solve the partial differential equations governing the fluid flow and heat transfer behavior. The study is focused to investigate the effects of the convection, conduction, radiation, and geometry on the heat transfer within the annulus. Results are presented for different values of aspect ratio, Rayleigh number, Radiation parameter, and radius ratio. It is observed that variation in aspect ratio causes the flow to change from a highly conductive to convective regime. The Rayleigh number increases the convective effects in the cavity by increasing and decreasing the local Nusselt number for the top and bottom

region of the inner wall respectively. The Radiation parameter increases the conductive effects causing uniformity in local Nusselt number throughout the inner wall. The radius ratio tends to scale the entire cavity causing the inner average Nusselt number to grow while keeping the bottom Nusselt number constant.

The radial heat flux on the outer wall keeps Nusselt number constant for all *Ar*, *Ra* and *Rr* values while increasing for *Rd*. The bottom heat flux on the other hand increases buoyancy effects in all conditions. The inner Nusselt number fluctuates based on *Ar* and *Rd*. while the bottom Nusselt number remains constant for all values.

BUOYANCY DRIVEN FLOWS AND HEAT TRANSFER IN A VERTICAL POROUS ANNULUS ENCLOSED IN A CYLINDER

By

Rabee Zuberi

Thesis submitted to the Faculty of the Graduate School of the
University of Maryland, College Park, in partial fulfillment
of the requirements for the degree of
Master of Science
2011

Advisory Committee:
Professor Chandrasekhar Thamire, Chair
Professor Amir Riaz
Professor James Duncan

Dedication

To my parents

Yemeen and Ghazala Zuberi

and my siblings

Rida and Zaki

finally,

my close group of friends

Your love and support have been the most important factor in my achievements.

Acknowledgements

I would like to thank my advisor Dr. Chandrasekhar Thamire for all his hard work and guidance. The most important lessons I learned from him were that patience and dedication to work are the key factors in success.

I would also like to thank my office and lab mates for their constant support. Either directly or indirectly, your help was invaluable in my research.

Additionally, I would like to thank Darin Sharar for his help in derivation of the governing equations. His work was very useful in my research.

Table of Contents

List of Tables

List of Figures

Chapter 1: Introduction

In the 21st century, the human population is facing some very difficult problems. Political, economic, environmental, and human health problems are rampant almost everywhere in the world today. One of the major reasons for all these crises is the lack of available natural resources. Depleting natural resources like oil, coal, and gas are used to provide energy that can be used to create other things. Vital industries including food, medicine, transportation, communication, and many others, depend on a constant and sustainable source of energy. These natural resources are not only reducing in amount but also harmful to the environment. As these resources decline, competition between people, communities, and even countries grows leading to all sorts of tensions. To curb the world's need of natural resources, scientists have been working to find alternative ways to create energy. One of the most abundant and most sustainable energy resources is solar energy. The sun has existed billions of years before the existence of earth and continues to provide vast amount of energy to all life on our planet. The amount of solar energy incident upon the Earth in one hour is enough to power everything on Earth for one whole year [1]. So logically it would be beneficial to harness as much of this energy as possible and use it to perform work. The two most popular ways to utilize solar energy today are photovoltaic solar panels, that use solar rays to produce electricity, and sun tracking mirrors called heliostats that concentrate solar radiation on a small area to provide a large heat flux. This study concentrates on the former method of capturing solar energy through solar power tower receivers.

1.1: Solar Power Tower Receivers

A solar power tower receiver stores heat from solar radiation to power mechanical or electrical systems. Most commonly, the solar tower receiver is part of a thermal storage system that is connected to a Rankine cycle turbine generator system to produce electrical energy [2].

As shown in *Figure 1* below, the basic functioning concept of a solar power tower consists of thousands of heliostats that concentrate the sunlight onto a center tower. As the tower heats up, a heat transfer fluid like molten salt or oil is pumped through the tower to absorb all that heat. The liquid is then pumped to a nearby steam generator to produce super-heated steam. The steam is then used to power the turbine generator system [2].

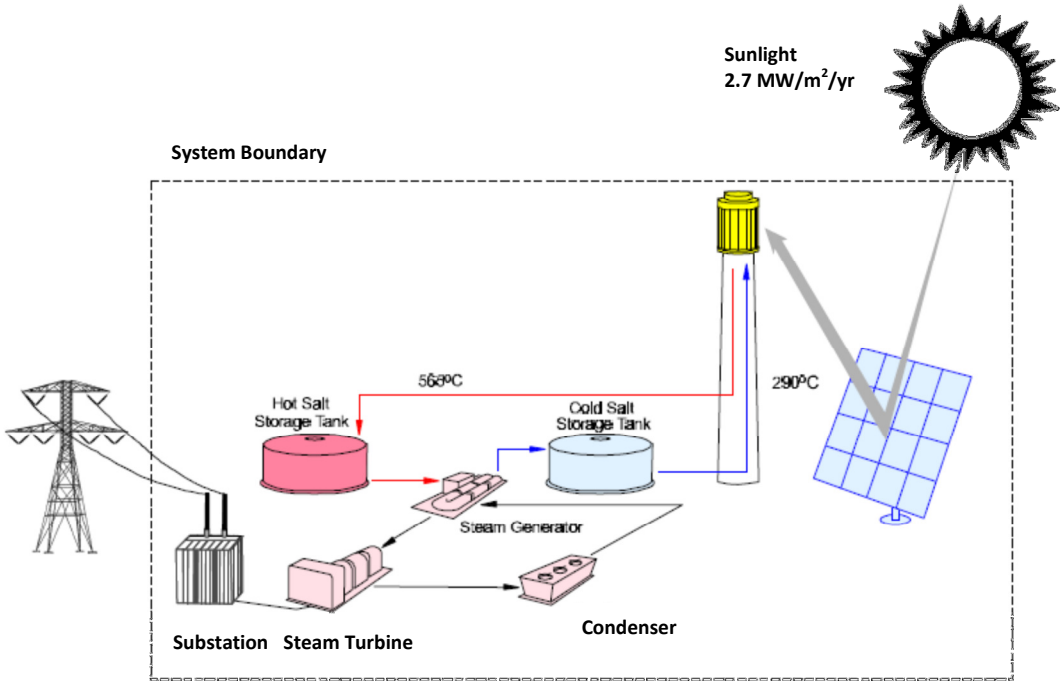

Figure 1: Schematic of a solar tower receiver system. [2]

Next, the heat transfer fluid is cooled upon exit from the steam generator then pumped back into the solar tower for the cycle to repeat. In certain cases, the thermal

storage system and steam generator system are combined by using water rather than molten salt. The water is directly converted into superheated steam in the solar tower receiver and pumped straight into the turbine generator system.

There are four main ways to increase the solar power tower capacity: increase the number of heliostats, raise the tower, enlarge the thermal storage tanks, and increase the receiver dimensions [2]. This study will concentrate on increasing the receiver dimensions through the use of porous media.

1.2: Porous Media

A porous material is "a material consisting of a solid matrix with an interconnected void" [3]. Some natural porous materials include beach sand, sandstone, coal, among others, and some artificial porous materials are concrete, fiberglass, construction insulation, metal foams, etc. The first study conducted on fluid behavior in a porous medium was by Henry Darcy in 1856 [3]. He observed a relationship between fluid flow rate and the applied pressure difference on the medium. But it was not until about 50 years ago that porous media gained popularity in heat transfer applications. Due to recent advancements in computer modeling, investigations of heat transfer in porous media were able to study complex geometries with many different porous parameters for a wide array of applications to support the modern needs.

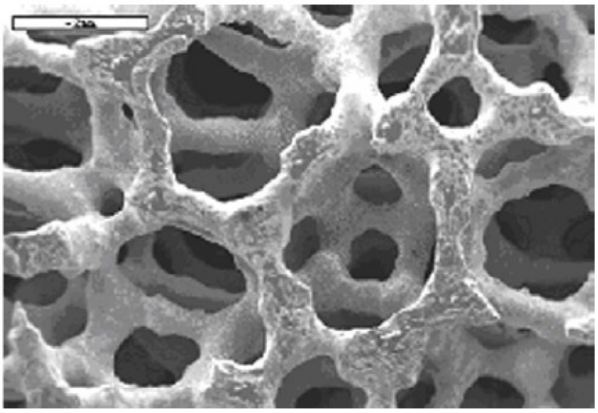

Figure 2: Close up view of a porous material [4].

In the past decade there have been many studies to incorporate a porous sleeve on pipes for either insulation or heat dissipation. Most studies were conducted for geothermal energy technology, thermal insulation, food storage, porous heat exchangers, solar power collectors, etc. [5], [6]. The basic function of porous media in heat transfer applications is that both convection and conduction effects are present in the porous system. Therefore by varying the characteristics of the porous media, such as porosity, permeability, etc., the heat transfer can be controlled for desired application [7].

Specifically, in the solar tower receiver application, a cylindrical annulus porous sleeve is attached around a cylindrical receiver to provide a larger surface area for greater solar energy to be stored and transferred to the fluid (see *Figure 3*). In this application both convection and conduction effects are utilized to transfer the heat from the outer boundary to the inner. Heat transfer through pure conduction usually causes the material to absorb some of the energy, therefore reducing efficiency. Convection on the other hand is through momentum transport and transfers the heat with less absorption.

1.3: Motivation

The motivation for this study is driven by the concept that inclusion of a porous sleeve on a solar tower receiver can affect the local heat flux within the receiver. By varying the geometry and convection and conduction effects of the system, a desired heat flux gradient can be achieved for higher efficiency. In addition, this research focuses on the effects of side and bottom external heat flux on the system.

Chapter 2: Literature Review

This chapter reviews the research conducted on natural convection in vertical annuli filled with a porous medium. The first section reviews papers on effects of radial heating while the second section reviews the research on effects of bottom heating on natural convection and heat transfer in vertical annuli.

It should be noted that almost all the results in all papers are quantified by the average Nusselt number ($\overline{Nu}$) and local Nusselt number (Nu). It is a non-dimensional number that represents the ratio of convection to conduction effects. The basic definition of the Nusselt number can be seen in [8] while its derivation specific to this study can be seen in *Appendix C: Non-Dimensionalization.*

2.1 Background Information

An extensive study by Nield and Bejan [3] provides great insight on the topic of convection in porous media. The mass, momentum, and energy equations are derived based on Darcy's law. The book covers everything from fundamental topics like basic derivation of energy and momentum equations for porous media and a study on forced, internal, and external convection.

2.2 Side Heating

Side heating is a popular topic for natural convection in porous media studies. This is due to the fact that most applications require thermal management of cylindrical vessels by attaching porous materials around them. As stated above, this includes, geothermal technology, storage of nuclear waste, underground piping etc.

Some of the earlier investigators studied natural convection in rectangular cavities without a porous medium. These studies play a vital role in developing an understanding of natural convection in porous media. A paper by Said and Trupp [9] studied free convection with air filled rectangular cavities with a heat flux on a side wall while the other is held at a constant temperature. The top and bottom walls are adiabatic. They used an implicit finite difference method using the Gauss-Seidel method to solve the energy and momentum equations with the Boussinesq approximation (see *Appendix B: Derivation* for definitions). Their main analysis was based on varying the aspect ratio (Ar) and they reported that the average Nusselt number peaks at around an aspect ratio of 1.5 and decreases as Ar changes in either direction.

A few years later porous media was introduced in a rectangular cavity with various boundary conditions. Prasad and Kulacki conducted numerical investigations of natural convection in a rectangular cavity with isothermal vertical walls of different temperatures [10] and with heat flux on one wall while the other is isothermal [11]. In both studies, the top and bottom walls were kept adiabatic. For [10], they reported that the flow regimes change as Ar changes. At low Ar the flow is driven by conduction, while at high Ar convection dominates. The average Nusselt number always increases when Ar is increased. As for the paper with heat flux on one wall, an increase in heat flux increases convective effects. The temperatures though do not increase proportionally. A large fraction of heat escapes from the top region of the cold wall. The average Nusselt number reaches a maximum within $1 \leq Ar \leq 2$.

Additionally, Jue [7] conducted a numerical study on natural convection in a porous rectangular cavity with isothermal walls and internal heat generation. The main analysis was conducted by varying the characteristics of the porous medium. He reported that a smaller permeability of the porous medium retards the circulation. While a larger porosity provides more flow area and results in stronger flow circulation and higher heat transfer.

Prasad and Kulacki also published two other papers for vertical annuli. One was an experimental paper on natural convection in a non-porous vertical annulus with isothermal walls [12]. While the other one was a numerical study of natural convection in a vertical annulus with porous medium and isothermal walls [6], both papers had very similar results. They concluded that the sink temperature for the boundary layer on the inner wall decreases as radius ratio (Rr) increase resulting in enhancement of heat transfer rate. The maximum $\overline{Nu}$ depends on Ar and Rayleigh number (Ra). The higher the Ra and/or Rr, the lower the Ar for maximum $\overline{Nu}$. This shows that porous media does not have much effect on the temperature distribution.

In the past decade, the effects of viscous dissipation have been included in the study of natural convection in porous media. A study by Saeid and Pop [13], on the effects of viscous dissipation in a rectangular cavity with isothermal walls with different temperatures, states that the fluid inside the cavity heats up due to the viscous dissipation of the momentum. High viscous dissipation parameter (ε) yields temperatures greater than T_{hot}. They report that the local Nusselt number (Nu) at the hot wall decreases as ε increases. Additionally, increase in ε leads to increase in Nu at the cold wall.

A very recent paper studied the effect of entropy generation by Chen et al. [14], in vertical annulus with isothermal walls at different temperatures. This study is based on the second law of thermodynamics which has not been done before. The maximum entropy generation number jumps from inner wall to outer wall as *Ra* increases. Radiation effects were also included into the natural convection in porous media study by Badruddin et al. [15] for a vertical annulus with isothermal walls of different temperature. They state that radiation plays an important role in the heat transfer when convection effects are low. The study reports that $\overline{Nu}$ increases with an increase in radiation parameter (*Rd*) and *Ra*.

Another paper by Badruddin et al. [16], studies the effects of radiation and viscous dissipation in a vertical annulus with isothermal walls of different temperatures. They report that $\overline{Nu}$ at the hot wall decreases with an increase in ε. While *Rd* leads to an increase in $\overline{Nu}$ at both walls.

2.3 Bottom Heating

As stated earlier, unfortunately there are not many papers on the topic of bottom heating. The papers reviewed in this section are mostly for a rectangular cavity with similar boundary conditions as the current problem. These papers are an appropriate source because the current problem is axisymmetric therefore the results will resemble a two dimensional rectangular problem.

To develop a good understanding of natural convection in a porous medium with bottom heating, the Rayleigh-Bénard problem has to be studied first. A book by E. L. Koschmeider called “Bénard Cells and Taylor Vortices” [17] provides a good basic understanding of the problem. Additionally, a study by Ahlers [18] also provides a

background on this problem while also going into detail on some selected topics. A study by Silano et al. [19] on numerical simulation of Rayleigh-Bénard convection for Prandtl and Rayleigh numbers provides a good understanding of the effect of *Ra* on the system. The paper states that *Ra* is the ratio of thermal forces versus the viscous forces acting on the fluid. Finally, Umla et a. [20] studies the roll convection of binary fluid mixtures in porous media. Their study consists of a fluid layer in a porous medium heated from below. The study compares flow with and without porous media. They report that the streamlines with porous media are deformed in the Soret regime due to the Darcy equation.

A numerical study by Sezai and Mohamad [21] studies the Rayleigh-Bénard convection for a two dimensional rectangular cavity. They state that the flow transitions from a single toroidal cell to two concentric counter rotating toroidal cells. They could not reach a convergent steady state solution for high *Ra* (~ $4x10^3$). Additionally, a study by Corcione [22] on the effect of thermal boundary condition on the side walls upon natural convection in rectangular two dimensional enclosures heated from below show a very comprehensive analysis on cell splitting due to Rayleigh-Bénard convection.

Next, a study by Saravanan and Sivaraj [23] on natural convection in a rectangular enclosure is reviewed. The boundary conditions consist of an adiabatic top wall with isothermal side cold wall and a non-uniform temperature on the bottom wall. The study reports that symmetrical temperature and flow fields exist about the center exist for uniform heating. They get distorted by non-uniform heating. The buoyancy and circulation grow as the heat flux below increases.

Rather than maintaining an isothermal hot wall, a heat flux is added at the bottom. A study by Ganzarolli and Milanez [24], on natural convection in rectangular enclosures heated from below while cooling from both sides with a heat flux on the bottom reports that there is no effect of uniform temperature or a uniform heat flux on the isotherms of a square cavity. Although for a shallow cavity, the isotherms fully occupy the cavity with a uniform heat flux on the bottom compared to a partial active cavity for uniform temperature. Another study by Sharif and Mohammad [25] on the same conditions concludes that diffusion dominates for a low Grashoff number ($Gr \leq 10^4$), while buoyancy driven convection dominates for $Gr = 10^5$. Additionally, the maximum temperature does change for diffusion dominated case but decreases as convection dominates. The average Nusselt number and maximum temperature do not change with aspect ratio.

The review of previous research for both heating orientation cases provides a good understanding of basic concepts that govern natural convection in a porous medium. This is highly valuable information that will be vital in deciding the validity of the results of this experiment.

Chapter 3: Research Setup

The study of natural convection in a vertical cylindrical annulus filled with a porous medium is conducted for two different boundary conditions. The system is subjected to an external radial flux and a bottom heat flux boundary condition. The radial heat flux is incident on the outer wall over all 360 degrees and the bottom heat flux is incident on the entire bottom wall simulating the horizontal and vertical components of incident solar radiation directed by heliostats.

This first step in this study was to set up a problem schematic and define physical parameters. Next, the governing mass, momentum, and energy equations for porous media were derived. The equations were non-dimensionalized and numericalized using finite difference method following the implicit scheme method. The non-dimensional variables are extracted from this process to be used in the main analysis. Next, the non-dimensional variables were assigned values base on the thermo physical properties of appropriate porous solid and fluid materials of the system. The validity of the code was checked by conducting grid generation analysis. In addition, verification was also done by conducting benchmarking experiments to check the accuracy of the results compared to previous studies. Finally, the main analysis was executed by varying the non-dimensional variables to observe the heat transfer within the annulus. The results are presented by obtaining average and local Nusselt number values for all boundaries. Isotherms and streamlines are presented as part of the results as well.

3.1 Problem Schematic

The problem consists of a vertical cylindrical annulus housing a porous medium saturated with a fluid. The diagram below shows the schematic in detail.

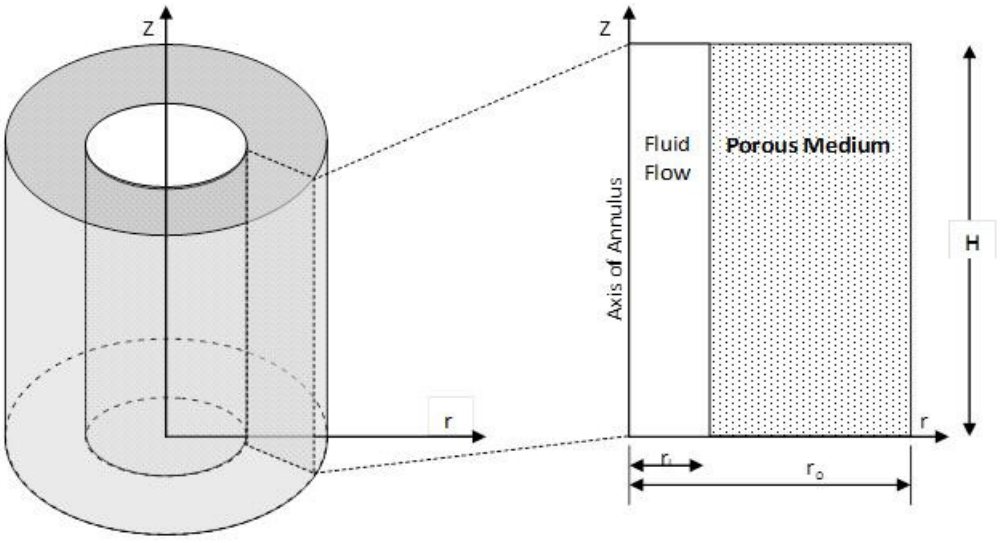

Figure 3: Problem Schematic

The figure on the right shows a front view cross section of the porous annulus. Axial symmetry is assumed in the entire problem. The aspect ratio Ar is defined as (H/L). The radius ratio Rr is defined as $\left(\frac{r_o - r_i}{r_i}\right)$.

The side heat flux is applied at $r = r_o$ and bottom heat flux is applied at $z = 0$. Constant temperature T_c is maintained at the inner surface due to heat absorbing fluid flowing through the center of the annulus. The top boundary is kept insulated. From this point on all references are made to the rectangular figure on the right due to axial symmetry of the problem.

3.2 Equations

The governing equations of the system are based on Darcy's law involving Boussinesq approximations [16]. The dimensional and non-dimensional continuity,

momentum, and energy equations are presented below. Full derivation of these equations can be seen in *Appendix B***:** *Derivation.*

3.2.1 Continuity Equation

The continuity equation is

$$\frac{\partial(ru)}{\partial r}+\frac{\partial(rw)}{\partial z}=0 \tag{3.1}$$

where *u* and *w* are the velocities in the *r* and *z* directions in polar coordinates.

3.2.2 Momentum Equation

The momentum equation is

$$\frac{du}{dz}-\frac{dw}{dr}=-\frac{g\beta_t K}{\nu}\frac{dT}{dr} \tag{3.2}$$

where β_t is the coefficient of thermal expansion, *K* is the permeability of porous medium, ν is the coefficient of kinematic viscosity, and *g* is the gravitational constant.

3.2.3 Energy Equation

The energy equation is taken from [16] although in this case, the radiation term is applied in both *r* and *z* directions.

$$\left(u\frac{\partial T}{\partial r}+w\frac{\partial T}{\partial z}\right)=\alpha\left(\frac{1}{r}\frac{\partial}{\partial r}\left(r\frac{\partial T}{\partial r}\right)+\frac{\partial^2 T}{\partial z^2}\right)-\frac{1}{\rho c_p}\left(\frac{1}{r}\frac{\partial}{\partial r}(rq_r)+\frac{\partial}{\partial z}(q_r)\right) \tag{3.3}$$

$$+\frac{\mu}{K}(u^2+w^2)$$

where

$$q_r=\frac{16\sigma}{3\beta_r}\frac{\partial T}{\partial \chi} \tag{3.4}$$

In this equation σ is the Stephan Boltzmann constant, β_R is the absorption coefficient and μ is the dynamic term. The left hand side of the equation accounts for energy transport through convection and the first term on the right side corresponds to conduction transport. The radiation transport is represented by q_r (*Equation 3.4)* where χ represents the respective axis of radiation transport. This term represents the heat transfer occurring through radiation within the cavity. The porous solid radiates heat to within itself. It is derived by using the Roseland approximation and Taylor series expansion [16] (see *Appendix B*). Finally, the viscous dissipation effect is represented by the last term in *Equation 3.3*. This term represents the heat generated by the friction of fluid and porous solid interface [26].

3.2.4 Boundary Conditions

In total, three main types of boundary conditions are used at various boundaries: constant temperature, adiabatic, and heat influx. The constant temperature boundary condition is

$$T = T_{const} \tag{3.5}$$

where T_{const} represents a certain constant temperature. The adiabatic boundary condition is

$$\frac{\partial T}{\partial \chi} = 0 \tag{3.6}$$

While the incident heat flux on the boundary is equated to condition and radiation within the porous region. It is described as

$$\frac{\partial T}{\partial \chi} = \frac{q"}{\left(-k - \frac{4\sigma}{3\beta_R \rho c_p} 4T_\infty^3\right)} \tag{3.7}$$

where *q"* is in the incident heat flux on the porous region (see *Appendix B.4.2*).

3.2.5 Nusselt and Energy Numbers

The results were quantified by obtaining a Nusselt number for all four walls. The Nusselt number is defined by (*hL*/*k*). It is the ratio of convection over conduction. The derivation of *Nu* can be seen in *Appendix C.6 Nusselt and Energy Number*. A local Nusselt number is calculated for each node on a wall. Next, all the local Nusselt numbers are added together to obtain an overall average Nusselt number for each boundary. The equation used for the average Nusselt number is based on a temperature difference between the respective wall (T_w) and the outside environment (T_∞) for the left hand side of the equation (see *Appendix C.6.1*).

$$h(T_w - T_\infty) = -\left[\left(k + \frac{16\sigma T_\infty^3}{3\beta_R}\right)\frac{\partial T}{\partial \chi}\right]_{\chi_{wall}} \tag{3.8}$$

The heat transfer is calculated and identified as the Energy number. It is derived using this equation (see *Appendix C.6.3*):

$$\mathrm{Q} = \left(k + \frac{16\sigma T_\infty^3}{3\beta_R}\right)\frac{\partial T}{\partial \chi} A_{wall} \tag{3.9}$$

where A_{wall} represents the area of the respective wall. The mass flow rate is derived similarly since it is based on the amount of energy entering the inner pipe. The derivation can be seen in *Appendix C.6.4*

$$\dot{m}\mathrm{h}_{fg} = \left(k + \frac{16\sigma T_\infty^3}{3\beta_R}\right)\frac{\partial T}{\partial r}(2\pi r \Delta \mathrm{z} L) \tag{3.10}$$

3.2.6 Non-Dimensionalized Equations

Prior to non-dimensionalization, the velocities are converted into streamlines using these relationships,

$$u = -\frac{1}{r}\frac{\partial \psi}{\partial z}, \qquad w = \frac{1}{r}\frac{\partial \psi}{\partial r} \tag{3.11}$$

Next, all the equations are non-dimensionalized by using a relationship for the basic physical dimensions. The non-dimensional parameters are noted with a bar above them (i.e. $\bar{r}$)

$$\bar{r} = \frac{r}{L}, \quad \bar{z} = \frac{z}{L}, \quad \bar{\psi} = \frac{\psi}{\alpha L}, \quad \bar{T} = \frac{(T - T_c)}{\Delta T}, \quad \Delta T = \frac{q"L}{k\left(1 + \frac{4}{3}R_d\right)} \tag{3.12}$$

where T_c is the temperature for the inner cold wall.. The ΔT for this study is based on the heat flux incident on the cavity. The dimensional heat flux is represented by *q"*. After substitution and simplifying the resultant non-dimensional parameters are extracted from the equations:

$$Ra = \frac{gK\beta_t L\Delta T}{\nu\alpha}, \qquad Rd = \frac{4\sigma T_\infty^3}{\beta_R k}, \qquad \varepsilon = \frac{\alpha\mu}{(\Delta T)K\left(\rho c_p\right)_f} \tag{3.13}$$

Ra, *Rd*, and ε are considered the Rayleigh number, radiation parameter, and viscous dissipation parameter respectively.

Momentum Equation

Using these relationships the final momentum equation looks like

$$\bar{r}\frac{\partial}{\partial \bar{r}}\left(\frac{1}{\bar{r}}\frac{\partial \bar{\psi}}{\partial \bar{r}}\right) + \frac{\partial^2 \psi}{\partial \bar{z}^2} = \bar{r}Ra\frac{\partial \bar{T}}{\partial \bar{r}} \tag{3.14}$$

Energy Equation

The final non-dimensionalized energy equation:

$$\frac{1}{\bar{r}}\left[\frac{\partial\bar{\psi}}{\partial\bar{r}}\frac{\partial\bar{T}}{\partial\bar{z}}-\frac{\partial\bar{\psi}}{\partial\bar{z}}\frac{\partial\bar{T}}{\partial\bar{r}}\right] \tag{3.15}$$

$$=\left[1+\left(\frac{4}{3}\right)R_d\right]\left[\frac{1}{\bar{r}}\frac{\partial\bar{T}}{\partial\bar{r}}+\frac{\partial^2\bar{T}}{\partial\bar{r}^2}+\frac{\partial^2\bar{T}}{\partial\bar{z}^2}\right]$$

$$+\varepsilon\left(\frac{1}{\bar{r}^2}\right)\left[\left(\frac{\partial\bar{\psi}}{\partial\bar{r}}\right)^2+\left(\frac{\partial\bar{\psi}}{\partial\bar{z}}\right)^2\right]$$

Boundary Conditions

The non-dimensional boundary conditions are stated as follows.

The non-dimensional constant temperature boundary condition is

$$\bar{T}=\bar{T}_{const} \tag{3.16}$$

The non-dimensional adiabatic boundary condition is

$$\frac{\partial\bar{T}}{\partial\bar{\chi}}=0 \tag{3.17}$$

where χ represents the respective axis. The non-dimensional heat flux boundary condition is

$$\frac{\partial\bar{T}}{\partial\bar{\chi}}=-\frac{q"L}{k\Delta T}\frac{1}{\left(1+\frac{4}{3}R_d\right)}=\bar{q} \tag{3.18}$$

where $\bar{q}$ represents the non-dimensional heat flux. For simplicity, the radiation and conduction effects are combined into one term: $k_{eff}=k\left(1+\frac{4}{3}R_d\right)$

Nusselt Number

The local non-dimensional Nusselt number for the inner wall is defined as:

$$Nui=\frac{hL(\bar{T}_\infty)}{k}=\left(1+\frac{4R_d}{3}\right)\frac{\partial\bar{T}}{\partial\bar{r}}\bigg|_{r_i} \tag{3.19}$$

where the $\bar{T}_\infty$ is defined as

$$\bar{T}_{\infty} = \frac{T_{\infty} - T_w}{\Delta T} \tag{3.20}$$

This is a modified version of *Equation 3.10* with the same ΔT. While the non-dimensional average inner Nusselt Number equation is

$$\overline{Nu_i} = -\frac{\int_0^{Ar} \left(1 + \frac{4R_d}{3}\right) \frac{\partial \bar{T}}{\partial \bar{r}} dz \Big|_{r_i}}{Ar} \tag{3.21}$$

Additionally, the Nusselt number for the active wall with an incident heat flux is defined as:

$$Nu_{\chi} = \frac{\mathrm{h}L}{k} = \left(1 + \frac{4Rd}{3}\right) \left(\frac{\partial \bar{T}}{\partial \bar{\chi}}\right)\Big|_{\chi_{wall}} \tag{3.22}$$

The average Nusselt number is

$$\overline{Nu_{\chi}} = \frac{\int_0^{\lambda_{ratio}} \left(1 + \frac{4Rd}{3}\right) \left(\frac{\partial \bar{T}}{\partial \bar{\chi}}\right) d\lambda \Big|_{\chi_{wall}}}{\lambda_{ratio}} \tag{3.23}$$

Where χ represents the respective axis for the boundary and λ represents the axis orthogonal to χ . While λ_{ratio} is the aspect ratio for that axis.

For convenience, the average Nusselt number is referred to as simply the Nusselt number using the symbol '$\overline{Nu_i}$', the subscript indicates the respective wall (i.e. inner, outer, top, or bottom). The local Nusselt number is referred to as itself with the symbol being '*Nui*.'

Energy Number

The average energy for a wall can be found by

$$En = \int_0^{\lambda_{ratio}} \left(\frac{\partial \bar{T}}{\partial \bar{\chi}}\right) \bar{A}_{wall} d\lambda \tag{3.24}$$

where $\bar{A}_{wall}$ is the non-dimensional area of the respective wall.

Mass Flow Rate Number

The local Mass Flow Rate (*MFR*) is only calculated for the inner wall by

$$\Delta MFR = \frac{\dot{m}\mathrm{h}_{fg}}{q"L^2} = \frac{\partial \bar{T}}{\partial \bar{r}}(2\pi r_i \Delta \bar{z}) \tag{3.25}$$

The average *MFR* for the inner wall can be found by

$$MFR = \int_0^{Ar} \left(\frac{\partial \bar{T}}{\partial \bar{r}}\right)(2\pi r_i \Delta \bar{z})dz\Big|_{r_i} \tag{3.26}$$

These are the equations used in this study. The boundary conditions are changed based on different experiments and are stated for each experiment.

3.3 Porous Materials and Properties

The assumptions for the system are that the porous cylinder is saturated with a liquid which is gray emitting, absorbing, and non-scattering. The solid porous material is isotropic and homogenous while being in thermal equilibrium with the fluid

The non-dimensional parameters are based on the physical and thermo physical properties of the system. The range of the non-dimensional parameters is chosen from [16]. The range for Rayleigh number is between $50 \leq Ra \leq 1000$. The range of the Radiation parameter is between $1 \leq Rd \leq 10$. The viscous dissipation parameter was considered negligible with ε = 1e-6 remaining constant.

The range of these values was verified by picking sample materials and system properties. Fortunately there is a wide range of materials that can satisfy a successful operation of a solar power tower [27]. It is not feasible to list all the combinations in this paper. Therefore the sample materials chosen are aluminum and air as the porous solid and fluid materials respectively.

All the thermo physical properties of air are taken from [8]. The density and specific heat of pure aluminum are taken from [8] as well. The thermal conductivity, permeability, porosity, pore size, and pore density (pores per inch – PPI) of a porous aluminum are taken from [28]. The absorption coefficient is presented in [29]. The table below shows all the properties for the porous solid and fluid materials.

Table 1: Thermo physical properties and don-dimensional parameters.

Material Properties				System Properties			
Property	**Symbol**	**Units**	**Est. Value**	**Property**	**Symbol**	**Units**	**Est. Value**
Porous Solid - Aluminum							
Specific Heat	cp	J/(KgK)	903	Ambient Temperature	T?	K	3.50E+02
Densiy	ρ	kg/m^3	2702	Wall Temperature	Tw	K	6.64E+04
Thermal Conuctivity	k	W/(mK)	3	Different Temperature	ΔT	K	6.60E+04
Thermal Diffusivity	α	m^2/s	1.2296E-06	Heat Flux	q"	W/m^2	1.50E+04
Absorption Coefficient	βr	1/m	100				
Permeability	K	m^2	1.00E-10	delta r	dr	m	2.50E-02
Porosity	?		0.94	Characteristic Length	L	m	1.00E+00
Pore Size	dp	m	4.20E-03	Boltzmann constant	σ	W/m^2K^4	5.67E-08
Pores Per Inch	PPI		4.00E+00	Gravity	g	m/s^2	9.80E+00
Fluid - Air				**Non-Dimensional Parameters**			
Specific Heat (fluid)	cpf	J/(KgK)	1.01E+03	**Radiation Parameter**	**Rd**	4σT?^3/βrk	**9.98E-01**
Density	ρ	kg/m^3	7.70E-01	**Rayleigh Number**	**Ra**	gβtq"KL^2/(vα(keff))	**9.63E+01**
Thermal Conductivity	k	W/(mK)	3.38E-02	**Viscous Dissipation**	**ε**	αμ/ΔTKcpf	**2.22E-07**
Thermal Diffusivity	α	m^2/s	4.33E-05	**Flux Constant**	**q**	q"L/kΔT(1+4Rd/3)	**1.00E+00**
Viscosity	μ	kg/ms	2.64E-05				
Coeff. Kinematic Viscosity	v	m^2/s	3.43E-05	k (Porous Medium)	kp	W/(mK)	0.0974757
Coeff. Thermal Expansion	βt	1/K	2.21E-03	k effective	keff	k(1+4Rd/3)	2.27E-01

The main non-dimensional parameters are bolded on the bottom right corner. The Rayleigh number is calculated out to be 96.3, and the Radiation parameter is calculated to be 0.99. Both of them can be rounded to $Ra = 100$ and $Rd = 1$, falling within the range chosen. The viscous dissipation parameter results in 2.2e-7 but the value is set to be ε = 1e-6 because $\varepsilon \leq$ 1e-4 has a negligible effect on the results.

3.4 Analysis

The main analysis was conducted by varying *Ar*, *Rr*, *Ra*, and *Rd*. The physical parameters *Ar* and *Rr* are varied to observe the effect of geometry change on the heat transfer. While changes in *Ra* and *Rd* highlight the convective and conductive effects on the system.

The range of *Ar* is varied from $0.125 \leq Ar \leq 10$ to simulate geometries from a flat to a tall annulus. This helps in determining the most efficient height for the annulus. To make the analysis simple, three main values of *Ar* are chosen to represent three different geometries. A flat geometry is represented by $Ar = 0.125$, a square geometry is represented by $Ar = 1$, and a tall geometry consists of $Ar = 8$.

The variations in *Rr* are made to observe the effect of radius changes on natural convection in the annulus. It should be noted that changes in *Rr* affect the height of the annulus as well. The equations can be seen below.

$$R_r = \left(\frac{r_o - r_i}{r_i}\right) = \frac{L}{r_i}, \quad \text{and} \quad A_r = \frac{H}{L} \tag{3.27}$$

In this study, r_i is always held constant at $r_i = 1$. Therefore variations in *Rr* directly affect *L*. Since *Ar* is held constant for the *Rr* analysis, *H* has to vary proportionally with *L* causing the cavity to shrink or expand in its entirety.

The Rayleigh number and Radiation parameter control the convective, conductive, and radiation aspects of the system. The latter two are controlled by *Rd*. The range for *Ra* is $100 \leq Ra \leq 1000$ while the range for *Rd* is $1 \leq Rd \leq 10$. The results are presented by average and local Nusselt number values for all boundaries. Isotherms and streamlines are presented in the results as well.

Chapter 4: Numerical Method

To perform the simulation, these final equations and boundary conditions are numericalized using second order finite difference method and Taylor's series expansion. All coding and calculations were executed in MATLAB® 2011a.

4.1 Numericalized Equations

The temperature ($\bar{T}$) and streamline function ($\bar{\psi}$) are solved for steady state solutions using implicit iterative scheme. The numerical equations are shown below.

The numerical momentum equation:

$$\bar{\psi}_{i,j} = \left[\frac{\bar{\psi}_{i,j+1} + \bar{\psi}_{i,j-1}}{\Delta\bar{z}^2} - \frac{1}{\bar{r}}\frac{\bar{\psi}_{i+1,j} - \bar{\psi}_{i-1,j}}{2\Delta\bar{r}} + \frac{\bar{\psi}_{i+1,j} + \bar{\psi}_{i-1,j}}{\Delta\bar{r}^2} - \bar{r}Ra\frac{\bar{T}_{i+1,j} - \bar{T}_{i-1,j}}{2\Delta\bar{r}}\right] * \frac{1}{\left[\frac{2}{\Delta\bar{r}^2} + \frac{2}{\Delta\bar{z}^2}\right]} \quad 4.1$$

The numerical energy equation:

$$\bar{T}_{i,j} = \left[\left(\frac{\bar{\psi}_{i,j+1} - \bar{\psi}_{i,j-1}}{2\Delta\bar{z}}\right)\left(\frac{\bar{T}_{i+1,j} - \bar{T}_{i-1,j}}{2\Delta\bar{r}}\right) - \left(\frac{\bar{\psi}_{i+1,j} - \bar{\psi}_{i-1,j}}{2\Delta\bar{r}}\right)\left(\frac{\bar{T}_{i,j+1} - \bar{T}_{i,j-1}}{2\Delta\bar{z}}\right)\left(1 + \frac{4}{3}R_d\right)\frac{\bar{T}_{i+1,j} + \bar{T}_{i-1,j}}{\Delta\bar{r}^2} + \frac{\bar{T}_{i,j+1} + \bar{T}_{i,j-1}}{\Delta\bar{z}^2} + \varepsilon\left(\frac{\bar{\psi}_{i,j+1} - \bar{\psi}_{i,j-1}}{2\Delta\bar{z}}\right)^2 + \varepsilon\left(\frac{\bar{\psi}_{i+1,j} - \bar{\psi}_{i-1,j}}{2\Delta\bar{r}}\right)^2\right] / \left[\left(1 + \frac{4}{3}R_d\right)\left(\frac{2}{\Delta\bar{r}^2} + \frac{2}{\Delta\bar{z}^2}\right)\right] \quad 4.2$$

4.2 Grid Generation

A uniform square grid is generated for *r* and *z* axes. Grid convergence analysis was performed on a square cavity with equal size of *r* and *z* axes by gradually increasing the grid size to achieve an accurate solution while utilizing minimum computation time. The grid size is varied from 41x41 to 121x121 points. The parameters for this experiment were set to $Rr = 1$, $Ar = 1$, $Ra = 100$, $Rd = 1$, $\varepsilon = 1e\text{-}6$, $\bar{q} = 1$. The average inner Nusselt numbers and computational time for each experiment were recorded for analysis.

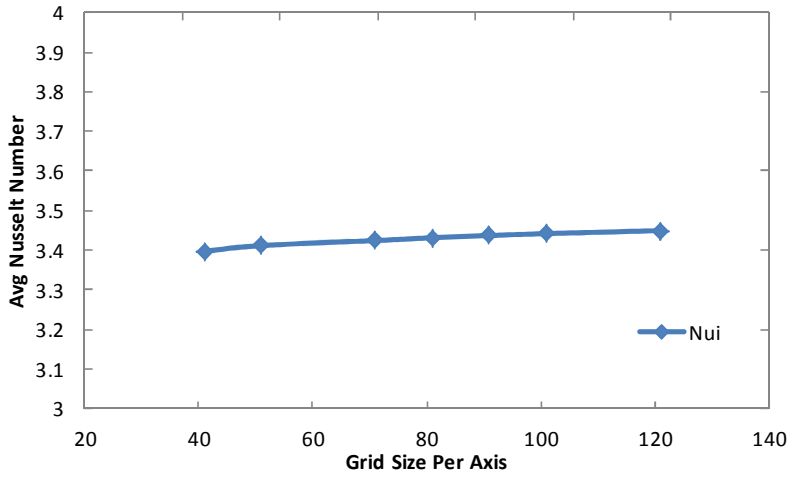

Figure 4: $\overline{Nu_i}$ with variation of grid size

The diagram above (*Figure 4*) shows a gradual increase in the average inner Nusselt number as the grid size for each axis increases. The increase in Nusselt number from 41 to 81 points is about 1% while the change from 81-121 points is about 0.5%. Therefore, grid sizes greater than 81 points per axis are more desirable.

Computation time was also recorded to further refine the results. The convergence time taken by each grid size is plotted below.

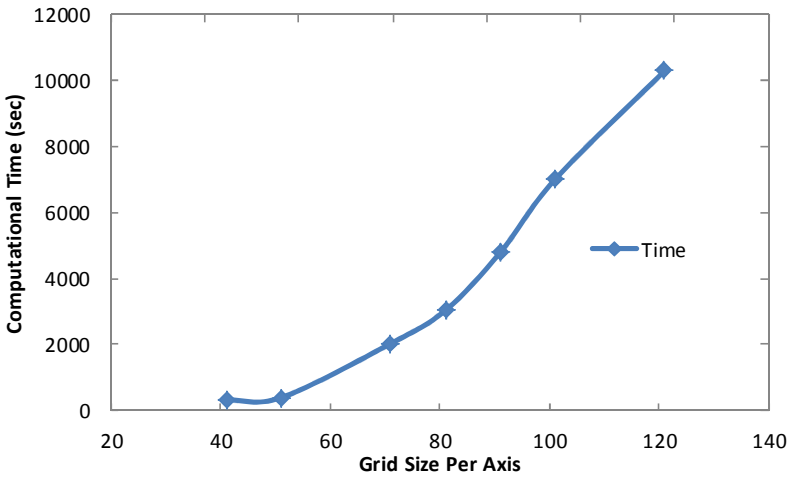

Figure 5: Computation time with variation in grid size.

The *Figure 5* shows the increase in computation time for 121 points is 3 times greater than the time for 81 points. Since the Nusselt number difference is only .5% in this range, it would be best to choose the grid size of 81x81 points.

A larger number of grid size points were necessary for higher *Ar, Rr,* and *Ra* values. For tall or flat geometries, the longer axis is increased to 8 while the shorter is set to1. Therefore the grid size for the larger axis is increased to 121 while the other axis is decreased to 31.

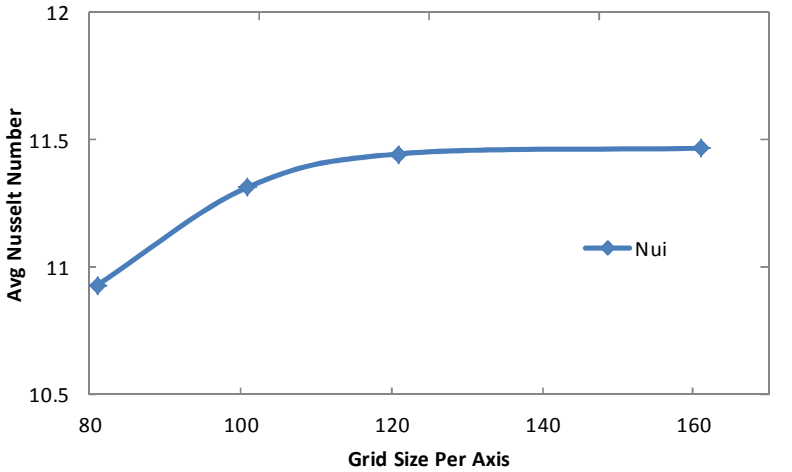

Figure 6: $\overline{Nu}_i$ with variations in grid size for larger axes.

The grid convergence plot for $Rr = 8$ and $Ar = 1$ in *Figure 6* shows that $\overline{Nu}_i$ converges at 121 grid points. The shorter axis is reduced to 31 points. Additionally,

since all the equations are bi-directional, these results can also be applied to $Ar = 8$ and $Rr = 1$ geometry.

Grid points were also increased for high *Ra* numbers regardless of aspect or radius ratios. The square geometry increased to 181x181 grids points and the flat or tall geometries increased to 161x51 grid points.

The criteria to accept the iterative convergence was set as

$$max\left(\left|\frac{\emptyset_{i,j}^{n} - \emptyset_{i,j}^{n-1}}{\emptyset_{i,j}^{n-1}}\right|\right) * 100 \geq \gamma \tag{4.3}$$

It is taken from [13] where ∅ represents $\bar{T}$ or $\bar{\psi}$ and γ represents the acceptance error value. Each node of the previous ∅ is subtracted from each node of the current ∅. The quantity is divided by each node of ∅ from the previous time step. The maximum value of the resulting matrix is then multiplied by 100 to get a percentage value.

The γ for $\bar{T}$ and $\bar{\psi}$ was set to 10^{-2} to cut computation time. While the γ was obtained through this equation:

$$error = \gamma = \frac{(min[dr\ dz])^2}{4} \tag{4.4}$$

Square the smallest grid spacing value (minimum of *dr* or *dz*) , then divide by 4. Generally the overall acceptance error was around 10^{-5}-10^{-6}. In addition to error checks, energy balance analysis was conducted on each experiment by adding the Energy number from all four walls. Since the system is at steady state and no energy is generated within the cavity the stored energy is ignored.

$$\left(\frac{En_{in} + En_{out} + En_{top} + En_{bot}}{En_{flux}}\right) * 100 \tag{4.5}$$

En_{flux} is the energy generated at the wall with the incident heat flux. This information is valuable in determining a quantifiable error of the result.

Chapter 5: Side Heating

This section analyzes the vertical porous cylinder annulus subjected to external side heating. Prior to the main analysis, a benchmark analysis is conducted by following [16] to verify the accuracy of the current code.

5.1 Benchmark Problems

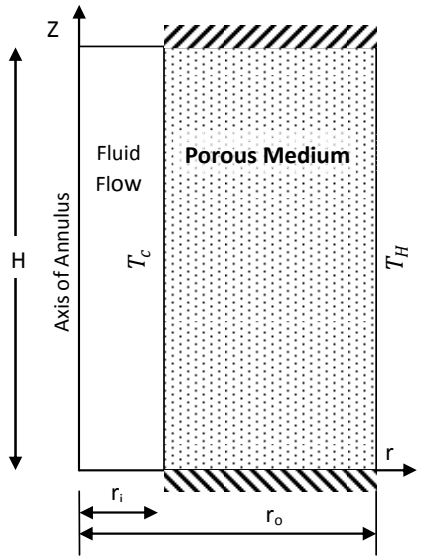

Figure 7: Vertical annulus with isothermal hot inner wall and outer call wall.

Reproducing the results provided in [16] proves that the current code is accurate and reliable. The current code is modified to fit the boundary conditions listed in [16]. The inner wall is set as the hot wall, $T_h = 1$, and the outer wall is the cold wall, $T_c = 0$ [*Figure 7*]. The top and bottom walls are adiabatic.

The boundary conditions are:

$$\text{At } \bar{r} = \bar{r}_i, \qquad \bar{T} = 1, \qquad \bar{\psi} = 0 \tag{5.1}$$

$$\text{At } \bar{r} = \bar{r}_o, \qquad \bar{T} = 0, \qquad \bar{\psi} = 0 \tag{5.2}$$

$$\text{At } \bar{z} = 0, \quad \text{and} \quad \bar{z} = Ar \qquad \frac{\partial \bar{T}}{\partial \bar{z}} = 0 \qquad \bar{\psi} = 0 \tag{5.3}$$

This flow is driven by a temperature gradient between the outer and inner boundaries. Therefore, ΔT is fixed to 300 K. The grid size was varied between 81x81 and 161x21 for convergence based on the axes lengths. Higher *Ra* values also required higher grid sizes for proper convergence.

Average Nusselt numbers for the inner wall are calculated and compared with the results of [16] plus results from previous papers provided in [6], [30], [31]. In the first comparison analysis, A_r is set to values of 3, 5, and 8 while $\varepsilon = 1x10^{-6}$, $Rr = 1$, $Ra = 100$, and $Rd = 0$, are held constant. The *Table 2* below shows the values.

Table 2 Benchmark Solution

Ar	Rajamani et al. [30]	Nath and Satyamurthy [31]	Prasad and Kulacki [6]	I.A. Badruddin et al. [16]	Present
3	3.868	3.81	3.7	3.88	3.859164
5	3.025	3.03	3	3.06	3.070574
8	2.403	2.45	2.35	2.42	2.488246

As it can be seen, the results obtained by the current code are on average about 2.13% greater than the average of the values from the stated papers.

5.2 Side Heating

The schematic diagram below shows a front cross section view of the vertical annulus. The outer boundary experiences an incident heat flux while the inner boundary is held at a constant temperature T_c. The top and bottom boundaries are adiabatic.

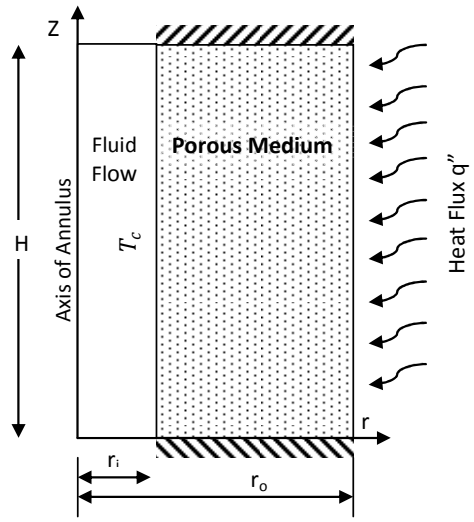

Figure 8: Vertical annulus with radial heating.

The boundary conditions are:

$$\text{At } \bar{r} = \bar{r}_i, \qquad \bar{T} = 0, \qquad \bar{\psi} = 0 \tag{5.4}$$

$$\text{At } \bar{r} = \bar{r}_o, \qquad \frac{\partial \bar{T}}{\partial \bar{r}} = \bar{q}, \qquad \bar{\psi} = 0 \tag{5.5}$$

$$\text{At } \bar{z} = 0, \quad \text{and} \quad \bar{z} = Ar \qquad \frac{\partial \bar{T}}{\partial \bar{z}} = 0, \qquad \bar{\psi} = 0 \tag{5.6}$$

In this analysis, the heat flux creates a temperature gradient that drives the flow. Therefore $\bar{q} = -1$, and ΔT is based on *Equation 3.10*. The standard grid size used in this analysis was 81 x 81. Grid size per axis was varied between 41 and 222 points depending on axis length, *Ra*, and *Rd* values. Generally, long axes and high *Ra* values required high grid sizes for proper convergence.

The study begins with an analysis of the *Ar* parameter, next the effects of *Ra* and *Rd* are observed, finally a short analysis of the *Rr* parameter is conducted. Average and local Nusselt numbers are calculated for all four walls to compare for results. In this case, the results are only provided for the active inner and outer walls since the top

and bottom walls are adiabatic. Isotherms and streamlines are also presented as part of the results. The values used for all the parameters are shown below.

Table 3: Values for non-dimensional parameters.

Ar	0.125	0.2	0.5	1	2	4	6	8	10
Ra	50	100	200	300	400	500	600	800	1000
Rd	1	2	4	6	8	10			
Rr	0.25	0.5	1	2					

5.2.1 Aspect Ratio Analysis

The Aspect ratio analysis is conducted for $0.125 \leq Ar \leq 10$, $Rr = 1$, $Ra = 100$, and $Rd = 1$. The study begins by analyzing the reference square geometry ($Ar = 1$). Then, the extreme cases of flat ($Ar = 0.125$) and tall ($Ar = 10$) geometries are observed.

At $Ar = 1$, the isotherms start off with a diagonal gradient with the highest temperature located at the outer top corner and the lowest temperature mostly concentrated at the inner bottom corner. This is because the outer top corner is the junction of the heated outer wall and the adiabatic top wall while the inner bottom corner holds the cold inner wall and the adiabatic bottom wall. As seen in *Figure 13a*, the temperature gradient on the bottom wall increases travelling in the positive r direction. The opposite is true for the top wall. This results in the isotherms forming a shape of a diagonal "S." The temperature gradient at the outer, top, and bottom walls is a clear evidence of an existence of a circular flow. This behavior is very similar to the benchmark problem in [16], [6]. The isotherms are in a diagonal shape with the highest temperatures concentrated in the upper hot wall region. Although in the current problem the hot wall has a vertical temperature gradient whereas the hot wall is held constant in [16]. The maximum temperature is $\bar{T}_{max} = 1.06$.

The streamlines show a unicellular flow rising at the outer wall and falling at the inner wall as the isotherms suggested. The velocity is the greatest at the edges of the cavity. The core of the cell seems stretched towards the top inner corner where the temperature gradient is the largest. A prominent boundary layer is observed at the inner wall.

The average inner Nusselt number value is 4.61. It is 100% greater than $\overline{Nu}_o$ based on the proportion of surface areas. The average Nusselt number for all Ar values remains constant as seen in *Figure 9*. This is due to the fact that the constant heat flux at the outer wall is fixed for all Ar values; therefore the average heat flux on the inner wall will always remain constant as well. The local inner Nusselt number on the other hand increases parabolically by a factor of 10 from $z = 0 \rightarrow z_{max}$ (see *Figure 15*). This shows that the heat transfer increases as z increases along the inner wall due to convection effects. The average En for both walls is $En = 12.41$ with an error of 0.2% in the energy balance.

Next, the height is reduced by decreasing Ar from $1 \rightarrow 0.125$. In this analysis, the isotherms begin straightening out vertically and at $Ar = 0.125$, the isotherms are almost vertical with a uniform horizontal temperature gradient. It can be seen in *Figure 18a* that the conductive effects are mainly driving the heat flow. Additionally, $\bar{T}_{max}$ increases by 29.6% from $\bar{T}_{max} = 1.06 \rightarrow 1.377$. The increase in $\bar{T}_{max}$ is indicative of an increase in T. This is because in *Equation 3.7*, the ΔT remains constant since q'', L, and k_{eff} remain constant. Additionally, T_∞ also remains constant; therefore T has to increase as $\bar{T}_{max}$ increases.

In physical terms, the increase of *T* is due to the characteristics of the flat geometry and the flow. The flow remains unicellular rotating counter clockwise covering the entire cavity. The cell becomes symmetric about the cavity *r* and *z* mid planes signaling uniform conduction effects. The average magnitude of *u* velocities on the top and bottom decreases by 46.7% while the average magnitude of *w* velocities on both sides decreases by 94.17%. The fluid in the upper half of the cavity flows towards the cold wall while the fluid on the bottom of the cavity flows towards the hot wall. Due to a small height and low velocities, both layers of fluid are in thermal equilibrium at any point on the *r* axis. This means that despite the presence of fluid flow, the general heat flow is based on conduction. Therefore it is not surprising to see that thermal conduction, which is based purely on molecular transport of energy, leads to higher local temperatures compared to convection, which is based on mass transport; such as the case in the square geometry.

As stated earlier, the reduction in height has no effect on the average Nusselt numbers (*Figure 9*). The inconsistency in the curve for low *Ar* values is due to the changes in grid size. The difference in $\overline{Nu_i}$ from $Ar = 1$ to 0.125 is 1.5%.The outer Nusselt number remains constant and $\overline{Nu_i}$ remains 100% greater than $\overline{Nu_o}$ since there is no change in radius.

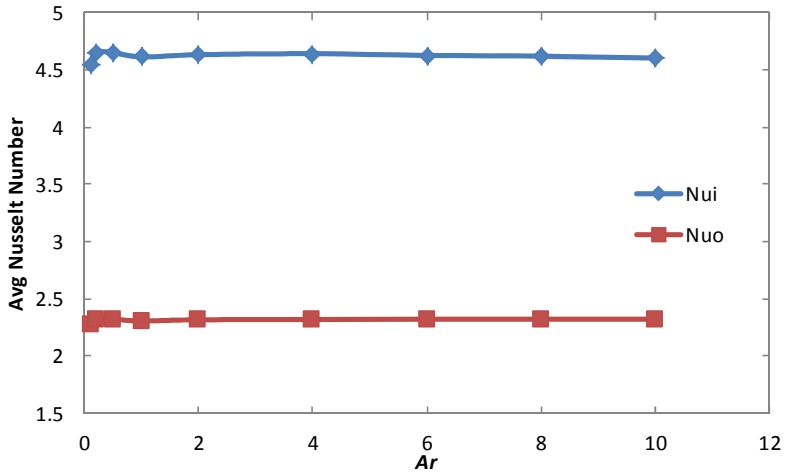

Figure 9: $\overline{Nu}$ with variation in *Ar*.

The effect of *Ar* is readily apparent for local *Nui*. Although the conduction effects increase in the flat geometry, the convection effects are present as well. As it can be seen in *Figure 10*, there is an increase of 17% in *Nui* travelling up from $z = 0$ to z_{max}. This indicates that the fluid gradually loses heat as it flows down along the cold wall. Additionally, reducing the height while keeping a constant heat flux leads to an increase in local temperatures within the cavity as stated above.

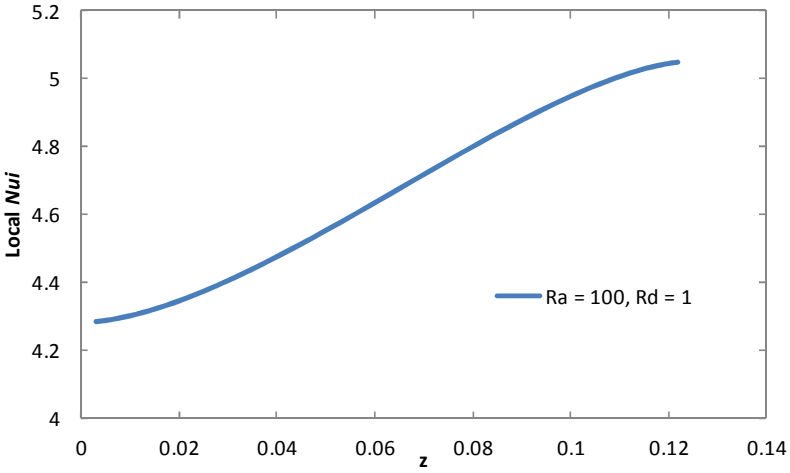

Figure 10: *Nui* along the *z* axis for the flat geometry (*Ar* = 0.125).

While the change in *Ar* has no effect on the Nusselt number, it does directly affect the overall heat transfer in the cavity. As the outer wall height varies, the heat transfer varies. It can be seen in *Figure 11* that *En* reduces by 87.6% to *En* = 1.59 due to the

reduction in height. The average error in the energy balance within $0.125 \leq Ar \leq 1$, is 0.39%.

Finally, the effects of increasing the height are observed by increasing Ar from $1 \rightarrow 10$. As a reference, the isotherms and streamlines for a tall geometry ($Ar = 8$) are shown in *Figure 21a*. The isotherms in the top region fall towards the cold wall. The middle 80% of the region seems like it got stretched out. The isotherms drop down almost vertically, and then change direction towards the heated wall in the bottom region. The close proximity of the hot and cold wall causes the temperature gradient to increase horizontally in the center of the cavity. The maximum temperature increases is from $1.06 \rightarrow 1.75$, an increase of 64.8%.

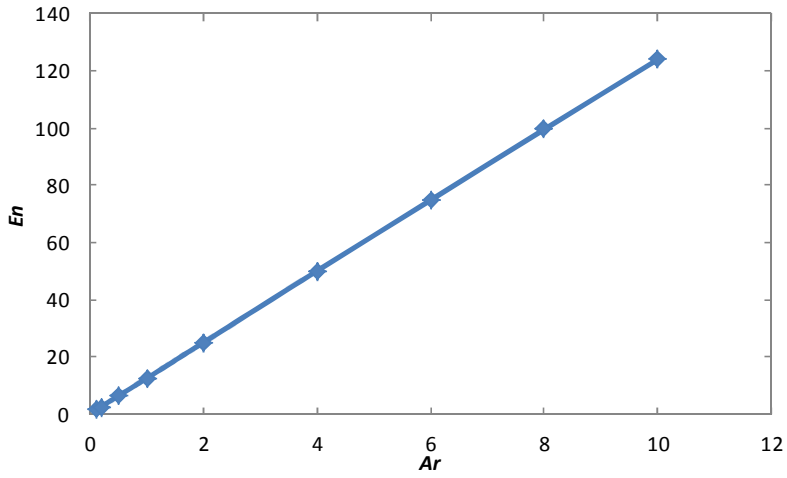

Figure 11: *En* number with variations in *Ar*.

The flow remains unicellular but the core moves up close to the top wall. This is because as the fluid falls along the cold wall, it slowly begins to heat up due to a close proximity to the hot wall and it slowly starts circulating back to the top even before it reaches the bottom wall. The average magnitude of u velocities decreases by a factor of 0.7 while it increases in the w direction by 3 times. Additionally, there is a reduction in boundary layer in comparison to the square geometry. This is evident by

observing that the streamlines closest to the heated wall, are parallel to the wall in *Figure 21* [11]. Similar to this result, the movement of the core and reduction in the boundary layer can be seen in [6].

Similar to the previous geometries, the Nusselt numbers for the active walls remain constant. Locally the *Nui* gradient is 0.8 for the bottom 83% of the inner wall, while it is 22.04 for the top 17%. The highest heat flux is found where the highest temperature gradient exists. This behavior can be observed *Figure 17*, and is also reported in [6]. Due to such a large height, the *En* number for the walls increases by a factor of 10 to $En = 123.89$.

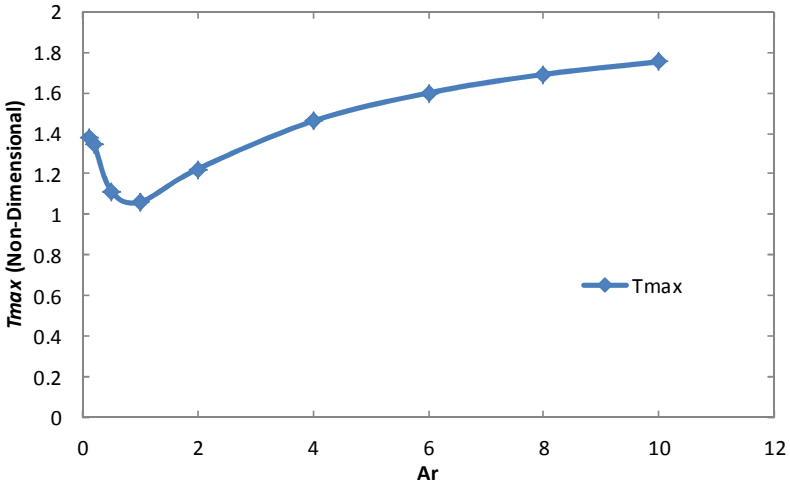

Figure 12: $\overline{T}_{max}$ with variations in *Ar*.

The increase in heat transfer is one of the main reasons for the rise of maximum temperature in the upper outer corner of the cavity. This can be explained by looking at a differential segment of fluid at the bottom of the outer wall. As this segment is heated from the outer wall, it travels up along it. The segment gains more and more energy on its way up. Therefore by the time it reaches the top, it achieves a temperature that is not achievable for geometries $Ar \leq 10$.

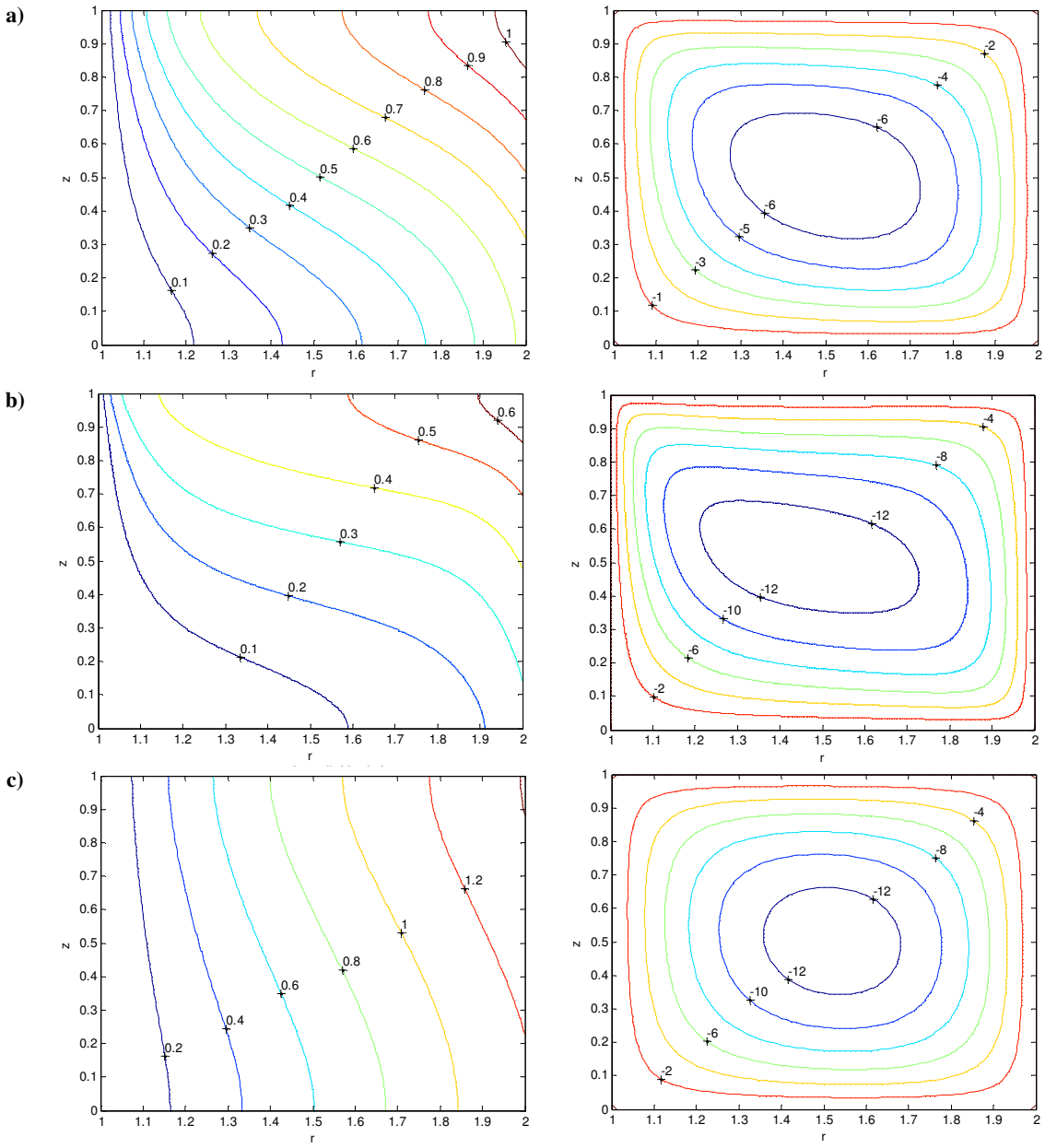

Figure 13: Isotherms and streamlines for a square geometry (*Ar* = 1 and *Rr* = 1) a) *Ra* = 100 and *Rd* = 1; b) *Ra* = 500, *Rd* = 1; and c) *Ra* = 100, *Rd* = 10

In conclusion, a few behavioral patterns are observed. The isotherms start from either the hot or the bottom wall and end somewhere on the top wall [11]. Similar formations have been observed in a nonporous vertical cavity by [9]. A change in Ar has no effect on $\overline{Nu}$ at any wall due to a fixed constant heat flux. On the other hand, the local *Nui* increase in the positive z direction at the inner wall which leads to a

higher heat transfer coefficient in those areas. This is based on *Equation 3.19*, where the increase in $\frac{\partial \bar{T}}{\partial \bar{r}}$ causes h to rise, since all the other parameters are held constant. Higher heat transfer rates are found near the top of the cavities due to convection. The heat transfer regimes are different for all three geometries. An increase in conduction effects is observed for low Ar values, while higher convection is observed for the tall geometry. The maximum temperature is lowest for the square cavity (Ar = 1) and increases by 29% for $0.125 \leq Ar \leq 1$ and by 65% for $1 \leq Ar \leq 10$ as seen in *Figure 12*.

Any geometry around Ar = 8 +/- 2 seems to provide the highest heat transfer rates. Although when the local heat flux gradients are taken into account, the same geometries tend to waste about 80% of the bottom cavity with really low heat fluxes. Flat geometries between $0.125 \leq Ar \leq 0.5$ provide very low heat transfer rates but a uniform heat flux. In this particular application, the best geometry would be around $6 \leq Ar \leq 10$.

5.2.2 Rayleigh Analysis

The Rayleigh number analysis is conducted for $50 \leq Ra \leq 1000$ while Rr = 1 and Rd = 1. The analysis was conducted for the square geometry (Ar = 1) first, followed by extreme cases of flat (Ar = 0.125), and tall (Ar = 8) geometries. Due to convergence issues and time constraints, the simulations for the square geometry were only conducted for $50 \leq Ra \leq 500$ with increments of 100 (except for Ra = 50). The flat and tall geometries are analyzed for $100 \leq Ra \leq 1000$ with increments of 200.

As Ra increases from 50 to 500 for the square geometry, the isotherms shift towards the outer top corner. As seen in *Figure 13b*, the temperature gradient near the outer

wall increases while the opposite is true for the inner wall. The maximum temperature decreases by 45.6 % from $\bar{T}_{max}$ = 1.23 → 0.67. This behavior can be understood conceptually considering that higher convection effects generally lead to higher velocities which in turn decrease local temperature. As a segment of fluid moves faster it is not able to absorb as much energy. Additionally, high temperatures usually form near the corners due to change in the velocity direction. A buoyant segment of fluid rises vertically while heating up along the hot wall of the cavity until it hits the top wall. This behavior results in hot fluid collecting in the corner while in the process of changing direction.

Mathematically speaking, this decrease in temperature can be understood by looking at the Rayleigh number definition. The increase in *Ra* can be achieved by increasing any of the 7 variables in *Ra*. Although in experimental conditions it is easier to vary the physical parameters of the system (i.e. initial temperature and length) compared to the thermo physical properties of the materials. Therefore this study will consider the thermo physical properties to remain constant while varying the physical parameters. The two main variables that can be changed easily in *Ra* are ΔT and *L*. Consequently the increase in *Ra* will result in the increase of the product of ΔT and *L* or either of them individually. When keeping *L* constant the increase in ΔT will result in the decrease of $\bar{T}$ based on *Equation 3.12*. Therfore, the increase in *Ra* causes $\bar{T}$ to decrease.

The flow is unicellular with the core stretching towards the inner top corner. The magnitude of the average *u* velocity in the upper and lower portion of the cavity increases by a factor of 3.3 while the magnitude of average *w* velocity increases by

4.2 times near both sides of the cavity. This is due to the momentum equation that causes the velocity to increase as *Ra* increases.

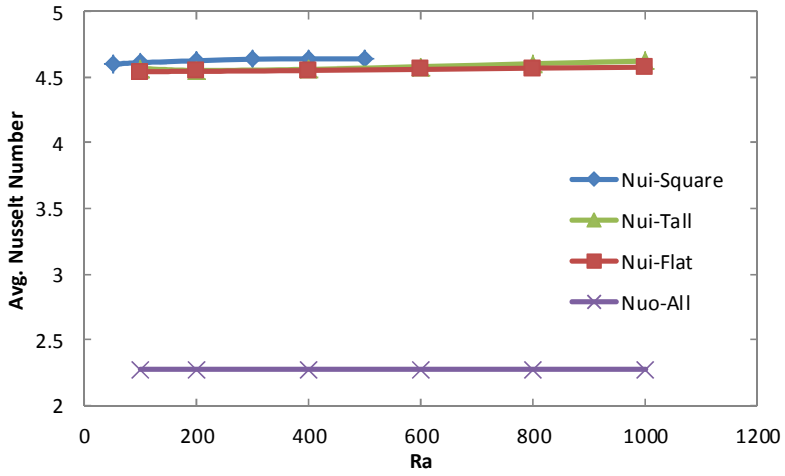

Figure 14: $\overline{Nu}_i$ with variation in *Ra*.

The average Nusselt numbers remain constant for all *Ra* values for all three geometries (*Figure 14*). This concept can be intuitively understood by the fact that the heat flux at the inner wall will remain constant as long as the heat flux at the outer wall remains constant. Similar to before, $\overline{Nu}_i$ is 100% greater than $\overline{Nu}_o$ due to difference in surface areas of the active walls.

The real effect of *Ra* can be seen in the heat flux distribution at the inner walls in *Figure 15*. It can be seen that the increase in *Ra* causes the *Nui* values to increase in the upper region of the annulus while lowering in the bottom region. The *Nui* rises by 48.9 times over the inner wall for *Ra* = 1000 while rising 10.5 times for *Ra* = 100.The variation in *Nui* is directly related to *h*. Therefore *h* is greater in the top 20% region of the inner wall while lower in the bottom 80% compared to *Ra* = 100. This is simply due to the increase in velocity of the flow causing the fluid to expel heat as it flows down along the inner wall. A consistent heat loss from the fluid on its way down, leads to a gradual decline in heat flux shown in the figure. The non-dimensional

energy number, *En*, values remain constant for this flow resembling $\overline{Nu}$(see *Figure 20*). The *En* values are graphed with respect to *Ra* and *Rd*.

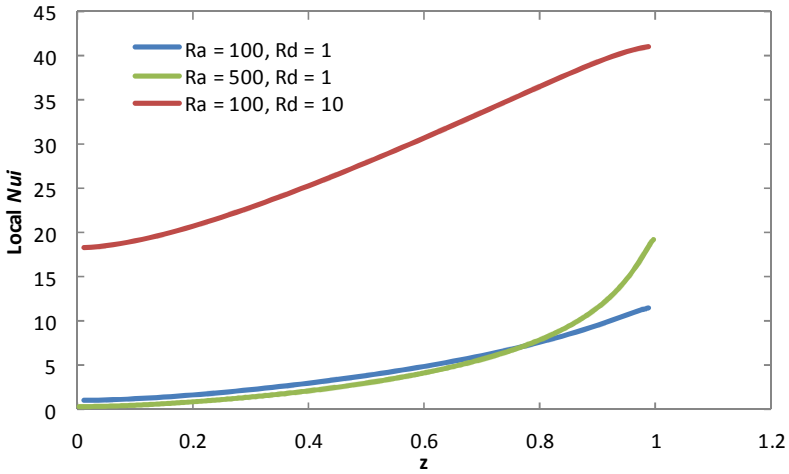

Figure 15: Local *Nui* along the *z* axis for the square geometry (*Ar* = 1).

For the flat geometry the range of the Rayleigh number is increased between $100 \leq Ra \leq 1000$ while $Ar = 0.125$, $Rr = 1$, and $Rd = 1$. As stated in the *Ar* analysis, at $Ra = 100$, the flat geometry behaves mainly based on conduction effects. As *Ra* increases, the convection effects become more apparent. As seen in *Figure 18b*, the isotherms form an '*S*' shape, indicating a slight temperature gradient in the vertical direction, with the bottom half of the isotherms directed towards the outer wall and the top directed towards the inner wall following the flow profile. This pattern is also reported in [10]. Similar to the square geometry, the maximum temperature decreases by 23% from $\bar{T}_{max} = 1.377 \rightarrow 1.05$.

The flow reacts to *Ra* with the core shifting towards the outer 25% of the annulus. The *w* velocity near the outer edge increases by a factor of 8.6 while increasing by a factor of 1.22 in the other 75% of the cavity. The *u* velocity increases by a factor of 6 near the top and bottom walls. This is due to the increase in convection effects. The

core is located in the region of high temperatures because that is where the fluid gains the most energy while it cools down in the rest of 75% of the cavity.

The convection effects can be observed in *Figure 16*, where the local *Nui* increases in the upper portion of the annulus while decreasing in the lower portion. It is interesting to note that the *Nui* curve shown in *Figure 10* seems completely flat in this figure. In comparison, the *Nui* increases by a factor of 3.22 from $0 \leq z \leq 0.125$ for $Ra = 1000$, while increasing 1.18 times for $Ra = 100$ for the same range of z. This increase in *Nui* is almost more symmetric about the z mid plane compared to the square geometry. This shows that the convection affects for the flat geometry are about equal in the top and bottom region of the inner wall. Secondly, the increase of *Ra* in the flat geometry leads to about half of the increase of *Nui* compared to the square geometry. Therefore it can be concluded that local convection effects are diminished in the flat geometry. Additionally, similar to the square geometry, there is negligible change in the average Nusselt numbers.

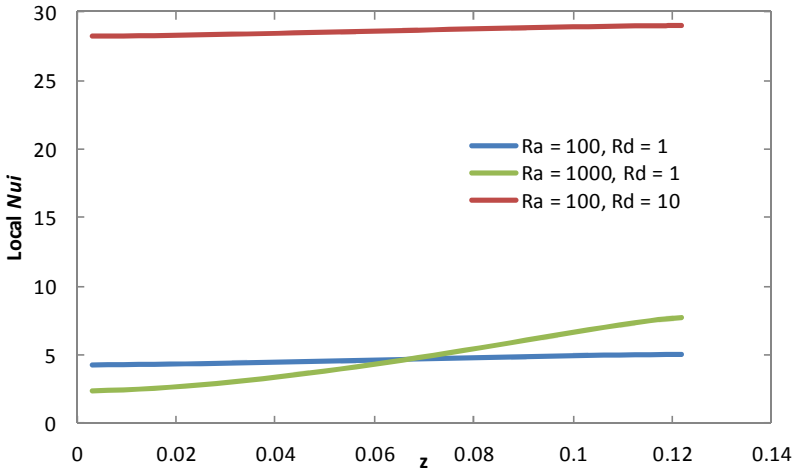

Figure 16: Local *Nui* along the z axis for the flat geometry ($Ar = 0.125$).

The tall geometry reacts to *Ra* similarly to the previous ones. The range for the Rayleigh number is $100 \leq Ra \leq 1000$ while $Ar = 8$, $Rr = 1$, and $Rd = 1$. In *Figure 21b*

the isotherms move diagonally towards the outer top corner moving in the same direction as the fluid. Similar to square geometry, the cold layer near the bottom wall gets thicker while higher temperatures move to the top [6]. The temperature gradient in the outer half of the annulus decreases, while the opposite is true for the inner half. The maximum temperature located in the outer top corner decreases by 45% from $\bar{T}_{max}$ = 1.69 → 0.929. The reason for this decrease is similar to the one for previous geometries.

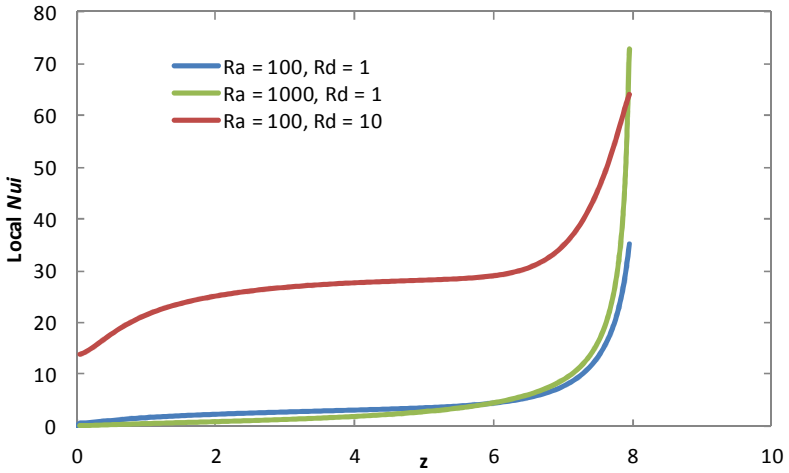

Figure 17: Local *Nui* along the *z* axis for the tall geometry (*Ar* = 8).

The core of the flow is in the upper half of the annulus. It remains stationary as *Ra* increases. The magnitude of *u* velocity increases by 2.63 times above the core, while increasing by a factor of 4.4 below the core. The magnitude of *w* velocities on the other hand, is about equal on both sides of the cavity increasing by 3.8 times as *Ra* increases from 100 to 1000. This is an indication of two things: first, the convection effects are getting stronger, and second that the outer wall is driving component of the flow.

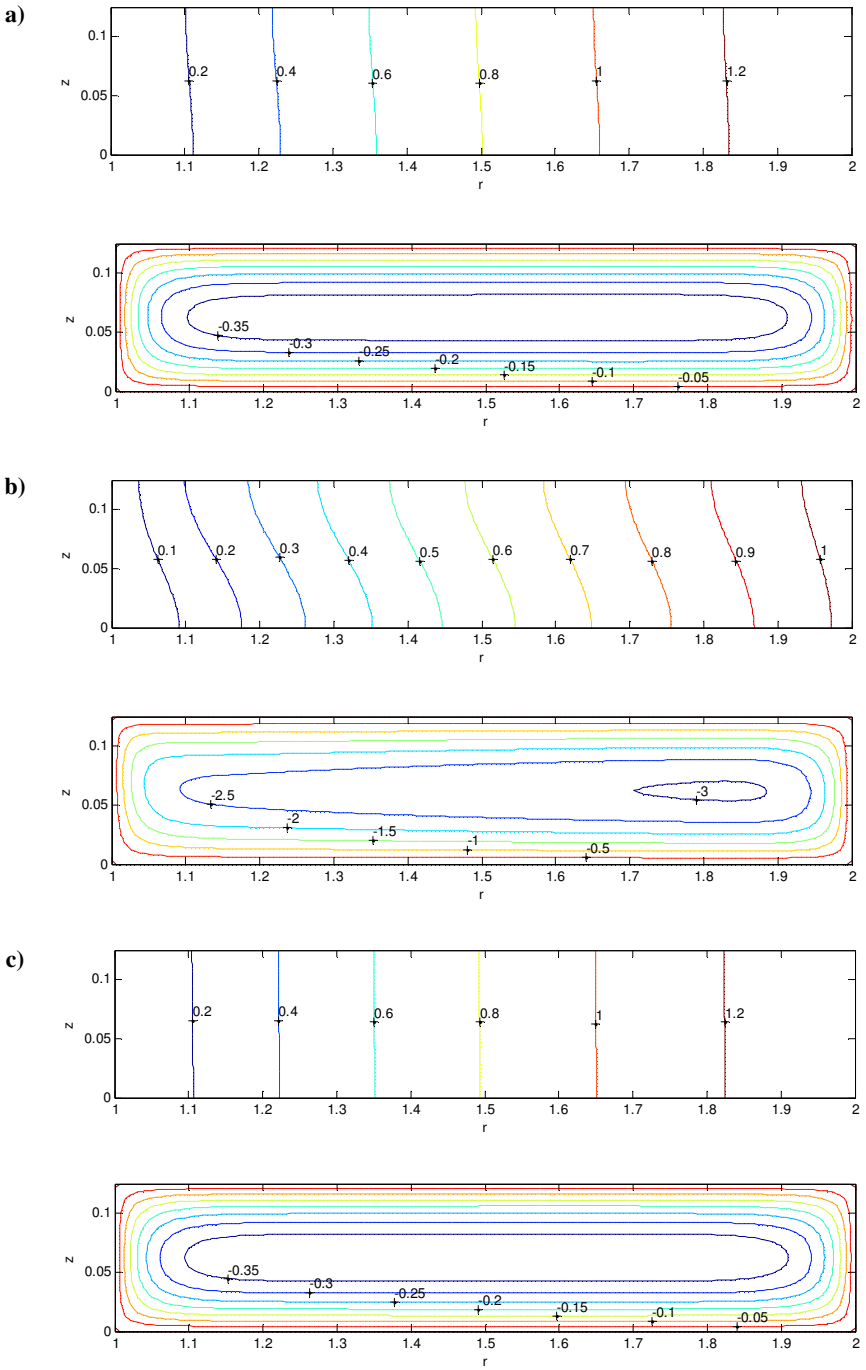

Figure 18: Isotherms and streamlines for flat geometry (*Ar* = 0.125) a) *Ra* = 100 and *Rd* = 1; b) *Ra* = 1000 and *Rd* = 1; and c) *Ra* = 100 and *Rd* = 10

The plot of local *Nui* in *Figure 17* shows that there is not a big effect of convection on the heat flux in the most of the lower half of the cavity from $0 \leq z \leq 6$. The *Nui* gradient between $0 \leq z \leq 6$ is 0.74 while it is 34.17 between $6 \leq z \leq 8$; increasing in

the positive direction. This highlights an increase in the heat transfer coefficient in the top region. There is negligible change in the average Nusselt numbers.

In conclusion, the effect of an increase in Rayleigh number can be outlined in three main points: the velocities of the flow increase due to the momentum equation, the local non-dimensional temperatures decrease due to increase in the product of ΔT and L, and a local Nusselt number gradient is created with the increase of Ra leading to an increase in h.

The increase of Ra has unique effects on the temperature change for the three geometries. The flat geometry is mostly dominated by conduction. An increase in convection causes the hot fluid in the outer half of the annulus to move towards the colder wall. Due to a low height restriction, flow cannot easily develop and it leads to the lowest temperature change of 23%out of all the geometries.

The temperatures for square and tall geometries on the other hand increase by about 45% each and are able to fully take advantage of convection effects due to relative larger heights.

Regarding the local Nusselt number, the tall geometry has the highest local Nusselt numbers in the top region in comparison to the other geometries. There is a drastic increase in heat flux in the top region of the inner wall. The flat geometry reacts in a symmetric increase and decrease of equal magnitude in the top and lower part of the inner wall respectively, with a smooth gradient in the middle. Finally the square geometry has a mixture of both where there is an increase the local Nui in the top region, while a very minimal reduction in Nui in the lower region of the inner wall.

On the other hand, the similarity between all the geometries is that most of the heat is

rejected in the upper 20% of the cold wall [11]. High *Ra* values (≈ 600 – 1000) with geometries of Ar ≥ 1 will be most beneficial in the current problem to produce high local Nusselt numbers in the top region of the inner wall.

5.2.3 Radiation Analysis

The Radiation parameter is ana1yzed for the range $1 \leq Rd \leq 10$ while $Rr = 1$ and $Ra = 100$. The effects of *Rd* on the cavity are first observed for a reference square geometry ($Ar = 1$), then the effects are observed on flat ($Ar = 0.125$) and tall ($Ar = 8$) geometries.

As $Rd = 1 \rightarrow 10$ in the square geometry, the general diagonal temperature gradient shifts to being mostly horizontal. The isotherms near the inner wall straighten out vertically, while the ones near the outer wall still show some curves. The patterns can be observed in *Figure 13c.* It is an evidence of conduction effects increasing within the cavity as *Rd* grows. The highest temperatures are concentrated at the top-outer corner. The maximum non-dimensional temperature rises from $\bar{T}_{max} = 1.06 \rightarrow 1.41$, a 32% increase. Theoretically speaking, increase in conductivity should not increase the internal temperature of the cavity. Therefore the rise in $\bar{T}_{max}$ is determined to be the effects of convection at play. An experiment described later in this section examines the relationship between *Ra* and *Rd* and explain the increase in $\bar{T}_{max}$ for this experiment.

Although this would be a good time to understand the effects of *Rd* mathematically. As stated earlier, due to a complex interplay between variables and non-dimensional numbers, there are many different ways an increase in *Rd* can affect the equations. A sample explanation is examined here that is specific to the solar tower receiver

problem at hand. First, let us consider the relationships between the each of the non-dimensional numbers. The Rayleigh number is related to *Rd* through ΔT (see *Equation 3.12* and *Equation 3.13*). Since *Ra* remains constant in this experiment, ΔT and *L* have to remain constant as well. On the other hand, ΔT is a function of *Rd*, *q"* and *L*. Since *L* appears in both *Ra* and ΔT, it will be held constant for simplicity. So this means that for ΔT to remain constant, *q"* has to increase with k_{eff}. The relationship can be seen in *Equation 3.12*. Therefore, it can be concluded that since ΔT remains constant, the increase in $\bar{T}$ should lead to an increase in the dimensional *T*. To summarize, this concept states the increase in *Rd* should have no effect on $\bar{T}$. Additionally, any changes that do happen to $\bar{T}$ due to other factors should be seen in *T* as well.

The flow remains unicellular with hot fluid rising at the outer wall and cold fluid falling at the inner wall. The core shrinks and shifts to the center of the cavity becoming symmetric about *r* and *z* axes. The general magnitudes of both velocities increase by about 70% which is also due to an increase in the heat flux. The boundary layers on the edges diminish.

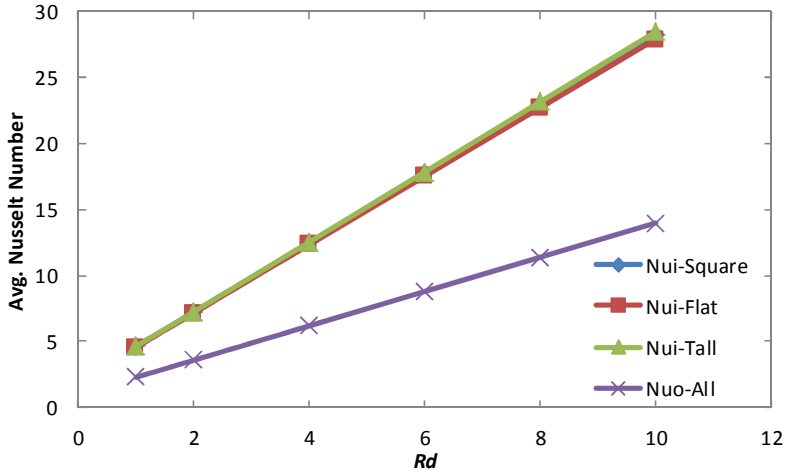

Figure 19: $\overline{Nu}_i$ for all geometries with variations in *Rd*.

The Nusselt numbers at the inner and outer walls increase by a factor 6.14 (see *Figure 19*). This result is purely based on the increase of the term (1+4*Rd*/3). The increase of *Rd* from 1 to 10 results in this term increasing by 6.14. This means that in actuality *h* for the inner and outer walls increases proportionally for all values of *Rd* due to the increase in *q"*. This can be intuitively understood since ΔT remains constant in *Equation 3.12*.

An evidence of increasing conduction effects is seen in the *Figure 15*. The local *Nui* increases 2.23 times between $0 \leq z \leq z_{max}$ for $Rd = 10$ while it increases by a factor of 10.43 when $Rd = 1$. The higher the conduction effects, the lower the heat flux gradient will be.

The non-dimensional energy number *En* remains constant as *Rd* increases. This is because *En* is a function of *q"* and the total energy *Q*. As *q"* increases *Q* increases proportionally. The *Figure 20* below shows the change in *En* with respect to *Ra* and *Rd* for all three geometries.

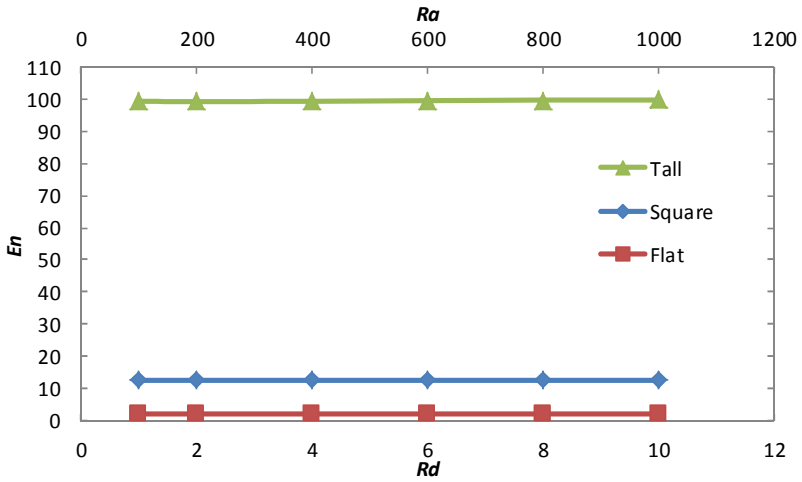

Figure 20: *En* with variations in *Ra* and *Rd*.

The increase of *Rd* on a flat geometry ($Ar = 0.125$) increases the conduction effects in the cavity. As explained in the *Ar* analysis, the flat geometry is initially mostly driven

by conductive effects. The increase of *Rd* from 1 to 10 intensifies those effects. As seen in *Figure 18a*, the isotherms are slightly slanted from the vertical and become completely vertical at *Rd* = 10 in *Figure 18c*. There is negligible change in the flow. A unicellular regime dominating the entire cavity and remains constant as *Rd* increases. The maximum temperature rises 0.5%. The temperature increase is much smaller in this case compared to the square geometry indicating that the system is in an almost purely conduction regime. As stated for the square geometry, the change in *Rd* has no effects on $\overline{T}$.

Similar to the square cavity the Nusselt numbers increase by 6.14. It can be seen in *Figure 16* that there is only a 2.8% change in the local *Nui* between $0 \leq z \leq z_{max}$. This shows that there is a very small heat flux gradient along the inner wall compared to the square cavity due to intense conduction effects.

The tall geometry (*Ar* = 10) behaves unlike the other two geometries. The isotherms look like they got stretched in the middle while the ends maintain the similar shape as the square geometry. As seen in *Figure 21c*, the increase in *Rd* from 1 to 10 transforms the isotherms to become parallel to the vertical boundaries in the middle while top region falls towards the cold wall, and the bottom region falls towards the hot wall. This pattern indicates that conduction effects dominate most of the middle region of the cavity while some convection effects are present near the top and bottom walls. The maximum temperature increases by 5% from $\overline{T}_{max} = 1.69 \rightarrow 1.77$. The increase in temperature is due to the same reasons as stated for the square geometry. But the temperature only increases by 5% because the conduction scheme dominates most of the middle cavity. Due to the close proximity of the side walls, the

heat can escape directly from the middle. At the same time the highest heat flux is present in the top inner corner due to convection. The reason goes back to the differential segment explanation. The convection effects and high heat flux cause temperature to collect near the outer wall and therefore produce high temperature gradients in the corner. The combination of convection and conduction leads to a minimal rise in temperature.

At *Rd* = 1, the flow looks like *Figure 21a* but as *Rd* increases to 10, the cell size increases expanding within the cavity (*Figure 21c*)see . The *u* velocities below the core increase by a factor 4.9. The magnitude of *w* velocities on both sides of the core increases by a factor of 1.22. This is due to the growing heat flux and the characteristics of the geometry. The long side walls provide room for high velocities to develop. It is also interesting to notice that the fluid layers in the middle region are distinctly horizontally stratified allowing for heat to flow in the horizontal direction. The Nusselt numbers are exactly the same as the other geometries. The relationship between *Nui* along the z axis is shown in *Figure 17*. It can be seen that the *Nui* values increase by a factor of 6.13 on average. This is a result of growing conduction effects and a growing heat flux. Most of the middle cavity shows a constant heat flux. The *En* values on the other hand, remain constant as shown in *Figure 20*.

An extra experiment was conducted to understand the effects of conduction without any convection involved. The motivation for this experiment is to understand the temperature increase when *Rd* is increasing. The experiment was conducted for all three geometries with *Rd* varying from 1 to 10 and a very low Rayleigh number (*Ra* =

1*)* to simulate minimum convection effects. The Rayleigh number is set to 1 because *Ra* = 0 led to numerical errors.

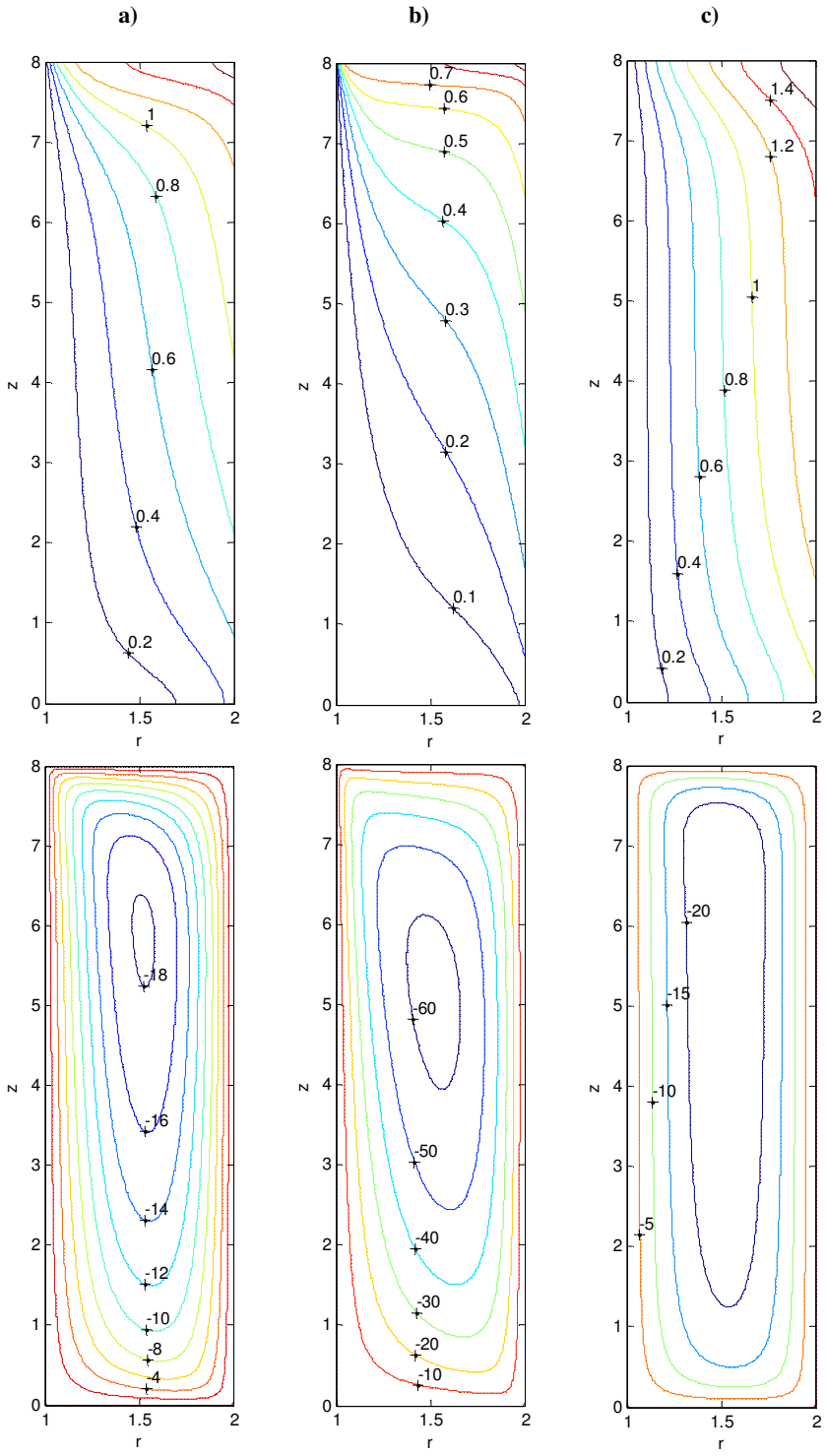

Figure 21: Isotherms and streamlines for tall geometry (*Ar* = 8) a) *Ra* = 100 and *Rd* = 1; b) *Ra* = 1000 and *Rd* = 1; and c) *Ra* = 100 and *Rd* = 10.

The results showed that there was a maximum of 3% decrease in $\overline{T}_{max}$ as Rd increased from 1 to 10. This verifies the earlier hypothesis, that increase in a pure conduction regime should not raise local temperatures.

Therefore the increase in local temperatures of the square and tall geometries is related to convection. This can be understood conceptually. As Ar increases, the fluid has more room to rise and gain momentum. Consequently the fluid moves up along the outer heat wall gaining heat. Once the fluid reaches the top outer corner of the cavity it has to turn in direction. As result, a concentration of high temperatures develops in that corner as seen by the isotherms of all three geometries. On the other hand, when Ar becomes really large ($Ar \geq 6$), the height to width ratio becomes too long. The distance between the side walls becomes much closer compared to the height. Therefore, the heat begins to conduct horizontally rather than travel by buoyancy. This phenomenon results in a lower temperature rise in taller geometries compared to the square one. In essence, the square geometry maintains the highest temperature because it has a height to width ratio of one. Buoyancy effects dominate in this geometry.

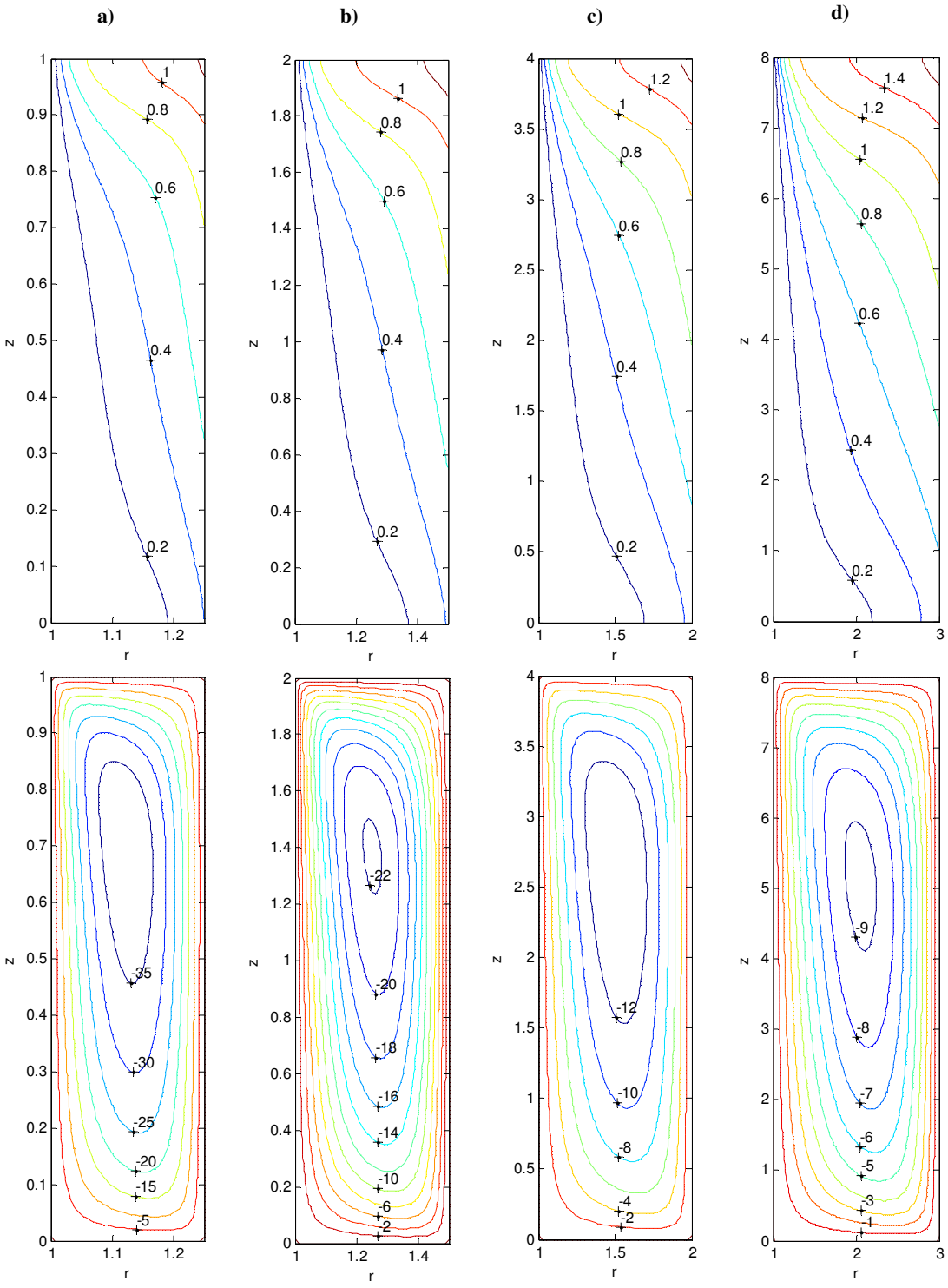

Figure 22: Isotherms and streamlines for a) *Rr* = 0.25; b) *Rr* = 0.5; c) *Rr* = 1; and d) *Rr* = 2.

In conclusion, the increase in *Rd* causes an increase in conduction effects. The average Nusselt number rises but the energy number remains constant. The heat transfer coefficient increases since *q"* and *Rd* are related. Once again, each geometry

behaves differently to changes in *Rd*. The flat geometry shows a pure conduction scheme while the tall geometry shows conduction in the middle and convection around the top and bottom. On the other hand, the square geometry shows growing effects of conduction, but is still mainly dominated by convection. The characteristics of the square geometry cause it to transfer heat mostly based on convection. This behavior leads to the highest temperature rise compared to all other geometries.

5.2.4 Radius Ratio Analysis

The range for *Rr* in this experiment is $0.25 \leq Rr \leq 2$ while $Ar = 4$, $Ra = 100$, and $Rd = 1$. The effects of increasing the radius on the heat transfer within the cavity are observed. Due to the scaling method, an increase in *Rr* increases the height and the outer radius proportionally while keeping the inner radius constant. This technique helps in understanding the effects of increasing or decreasing the width of the annulus. Since $Ar = 4$, the cavity's height is always 4 times greater than the effective width. Nonetheless, the effects of a growing radius are still evident.

As *Rr* increases, the isotherms expand by 13%. As seen in *Figure 22*, the temperature gradient is mostly horizontal with the highest temperatures located on the outer top corner. The highest temperature gradient is on the inner top corner. The maximum temperature rises from $\bar{T}_{max} = 1.23$ to 1.68, an increase of 36%. A higher cavity volume leads to higher heat storage with high temperatures.

The flow is unicellular with the core in the upper half of the cavity. Comparing with the tall geometry, the core is 1 unit lower in the current model due to a larger radius. An increase in *Rr* leads to bigger cell sizes. The average velocity decrease about 4 times. The low velocities are a result of the expansion in the cavity without any

change in the heat flux. This leads to heat storage within the cavity resulting in high temperatures.

The inner Nusselt number rises with *Rr*. While $\overline{Nu}_o$ stays constant, $\overline{Nu}_i$ increases by 138% (see *Figure 23*). This increase results from the growth in the radius and the height of the annulus. Locally, *Nui* increases by a factor of 45 between $0 \leq z \leq z_{max}$.

In conclusion, the *Rr* parameter seems to produce the most benefit out of all. A growth in $\overline{Nu}_i$ while keeping $\overline{Nu}_o$ constant is the exact aim of this problem. Coupling high *Rd* and *Ra* values will produce ever high $\overline{Nu}_i$ while maintaining low local temperatures.

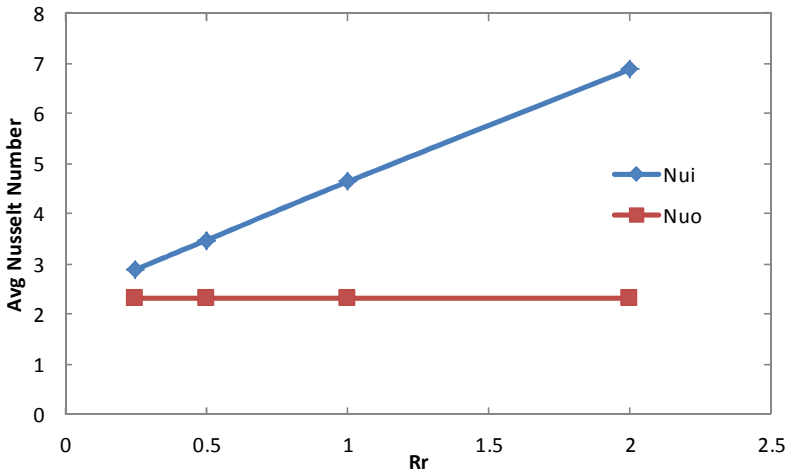

Figure 23: $\overline{Nu}_i$ with variations in *Rr* for *Ra* = 100 and *Rd* = 1.

5.2.6 Conclusion

The effects of varying *Ar*, *Rr*, *Ra*, and *Rd* on the cavity are observed in this chapter. Each variable has some unique effects on each of the three geometries. The results of each section are combined to create one system that should be most efficient for a solar tower receiver system.

The effects of varying *Ar* show that the average Nusselt number does not change for any *Ar* values due to a fixed heat flux at the outer wall. It can be seen that the overall

heat transfer grows as Ar increases based on the growth in the En number. The local heat flux is usually greater near the top of the inner wall. This also shows that h is higher for the upper inner wall region. Low Ar values ($Ar \leq 1$) lead to higher conduction effects while convection is more prevalent for the square geometry ($Ar = 1$). The maximum temperature is the lowest for square geometry. Although $Ar \geq 1$ geometries allow for increase in the flow, the increase in height to width ratio creates conduction effects in the middle of the cavity. The best geometry would be around $6 \leq Ar \leq 10$ since it provides the highest heat transfer.

The increase in the Rayleigh number results in an increase in the convection effects on the system. The velocities increase due to the inclusion of Ra in the momentum equation. All three geometries respond differently to the changes in Ra. The flat geometry is mostly dominated by conduction therefore it changes the least. The maximum temperature decreases by 23%, local Nui increases by a factor 3.22. The change is very symmetric where Nui decreases for bottom half of the cavity and increases about the same amount for the top half of the cavity. The tall and square geometry react similarly. The Nui for the top region of the inner wall increases drastically (more for tall geometry than square). There is minimal decrease in Nui for the lower 80% of the cavity.

The increase in Rr causes the entire cavity to expand. Since the outer heat flux is held constant and the outer radius increases, the inner heat flux rises with an increase in Rr. This is a much desired property since it results in the inner heat flux increasing. The drawback is that the size of the annulus cannot be easily changed in real life conditions.

As seen in the equation, the *MFR* number is directly related to the energy output. Higher energy outputs create high mass flow rates. The *MFR* number is also similar to the local Nusselt number. Therefore region of relatively high *Nui* lead to high *MFR* number. Any fluid can be chosen to flow within the pipe. For this specific application saturated water is used with an h_{fg} of 2257 x 10^3. Similar to the local *Nui* plots, the tall geometries tend to produce very high *MFR* values for the top 20% of the region but then the value drops almost to 0.

Chapter 6: Bottom Heating

This experiment is designed to study the effect of an incident heat flux at the bottom surface on natural convection inside the vertical annulus. The top and outer boundaries are kept adiabatic, while the inner boundary is held at constant temperature T_c.

Two preliminary benchmark solutions are presented by solving the Rayleigh- Bénard problem and then modifying it by adding a heat flux on the bottom. The results for all three experiments are quantified by calculation of average and local Nusselt numbers for all four walls. Isotherms and streamlines are also presented for visual understanding.

6.1 Benchmark Solutions

The bottom heating study is conducted in three steps. First a simple Rayleigh-Bénard problem is solved and compared with existing literature. Secondly, the problem is modified by adding a heat flux on the bottom wall. Finally, the main analysis is conducted with a heat flux on the bottom wall while the inner wall is held constant at T_c and the top and outer wall are kept adiabatic. This method improves understanding of the whole study by taking simple problems and increasing their complexities.

6.1.1 Rayleigh-Bénard Problem

A preliminary benchmark experiment is presented by solving the Rayleigh- Bénard problem. The inner, top, and outer wall boundary conditions are set to constant temperature T_c and the results are checked for comparison. The schematic is presented below.

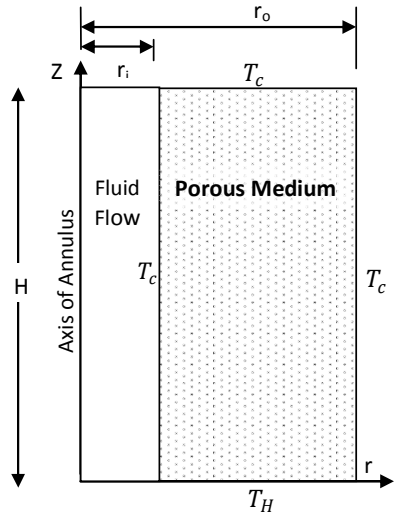

Figure 24: Rayleigh-Bénard Problem

The boundary conditions for this experiment are listed below:

$$\text{At } \bar{r} = \bar{r}_i, \quad \text{and} \quad \bar{r} = \bar{r}_o \qquad \bar{T} = 0, \qquad \bar{\psi} = 0 \tag{6.1}$$

$$\text{At } \bar{z} = 0 \qquad \bar{T} = 1, \qquad \bar{\psi} = 0 \tag{6.2}$$

$$\text{At } \bar{z} = H \qquad \bar{T} = 0, \qquad \bar{\psi} = 0 \tag{6.3}$$

This experiment was conducted with *Rr* held constant while *Ra* and *Rd* were varied for two geometries: square ($Ar = 1$) and flat ($Ar = 0.125$). The grid size was varied between 81x81 and 101x41 for convergence. The variation in grid size was in proportion to the axes lengths. Higher *Ra* values also required higher grid sizes for proper convergence. Since there is no heat flux in this experiment, ΔT is fixed to 300 K. The table below shows the range of all the variables used.

Table 4: Values for non-dimensional parameters.

Ar	0.125	0.2	0.25	0.5	1	
Rr	1					
Ra	100	200	400	600	800	1000
Rd	1	2	4	6	8	10

The investigation begins by analyzing the reference square geometry. At $Ar = 1$, the isotherms are symmetric about the vertical mid plane and mostly concentrated near

the hot wall (*Figure 25a*). The temperature profile is mostly symmetrical for all Rayleigh- Bénard convection simulations since both of the side walls are held at T_c. The profile represents a multidirectional conduction which acts in the direction of all three walls (top, inner, and outer). Similar behavior is also presented by Sharif and Mohammad [25] for a rectangular cavity bounded by an adiabatic top wall and cooled side walls. Although the top boundary condition is different, similar symmetric conduction effects are present in the bottom half of the cavity. This profile will be useful in understanding future simulations in this paper.

The flow consists of two counter rotating cells which rise along the vertical symmetry axis and fall along the side walls [25]. It can be seen in *Figure 25a*, that unlike [25], the flow is consistently asymmetrical with higher velocities in the outer half of the annulus. This is because the outer half of the annulus interacts with a greater heating area compared to the inner half. At steady state, the fluid in the outer region has to transport heat along a larger distance compared to the inner half in the same amount of time. This trend is consistent for all bottom heating experiments.

As the *Ar* decreases below 1 in *Figure 26a*, the isotherms flatten out and form a uniform temperature gradient in the vertical direction. At $Ar = 0.125$, the temperature gradient in the horizontal direction is only present near the inner and outer boundaries. The flow pattern on the other hand starts off as bi-cellular at $Ar = 1$ but then starts to show signs of a four cell regime at $Ar \leq 0.125$. Although no actual cells appear for low *Ra* values, the $\psi = 0$ lines emerge indicating stagnant flow in those regions [25].

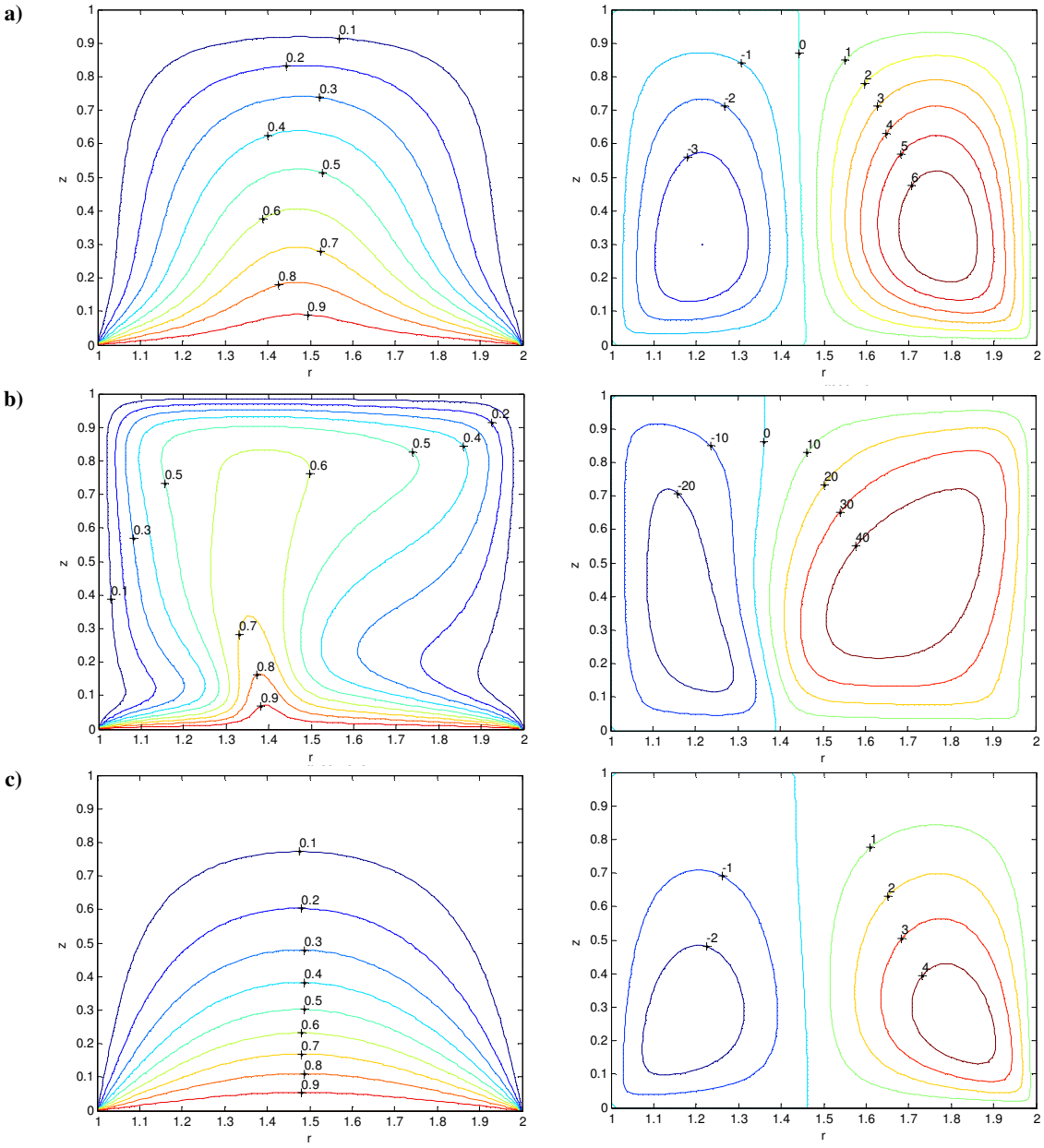

Figure 25: Isotherms and streamlines for a square geometry (*Ar* = 1 and *Rr* = 1) a) *Ra* = 100 and *Rd* = 1; b) *Ra* = 800, *Rd* = 1; and c) *Ra* = 100, *Rd* = 10

Unlike the isotherms, the flow is consistently asymmetrical with higher velocities in the outer half of the annulus. As *Ar* decreases, the velocities collectively decrease by a factor 1.4. The reduction in velocities is due to the splitting of cells. A study by Corcione [22] describes that the decrease in *Ar* causes the "breakdown of the density stratification in the fluid layers adjacent to the top and bottom walls." This results in emergence of columns that transport hot fluid up and cold fluid down.

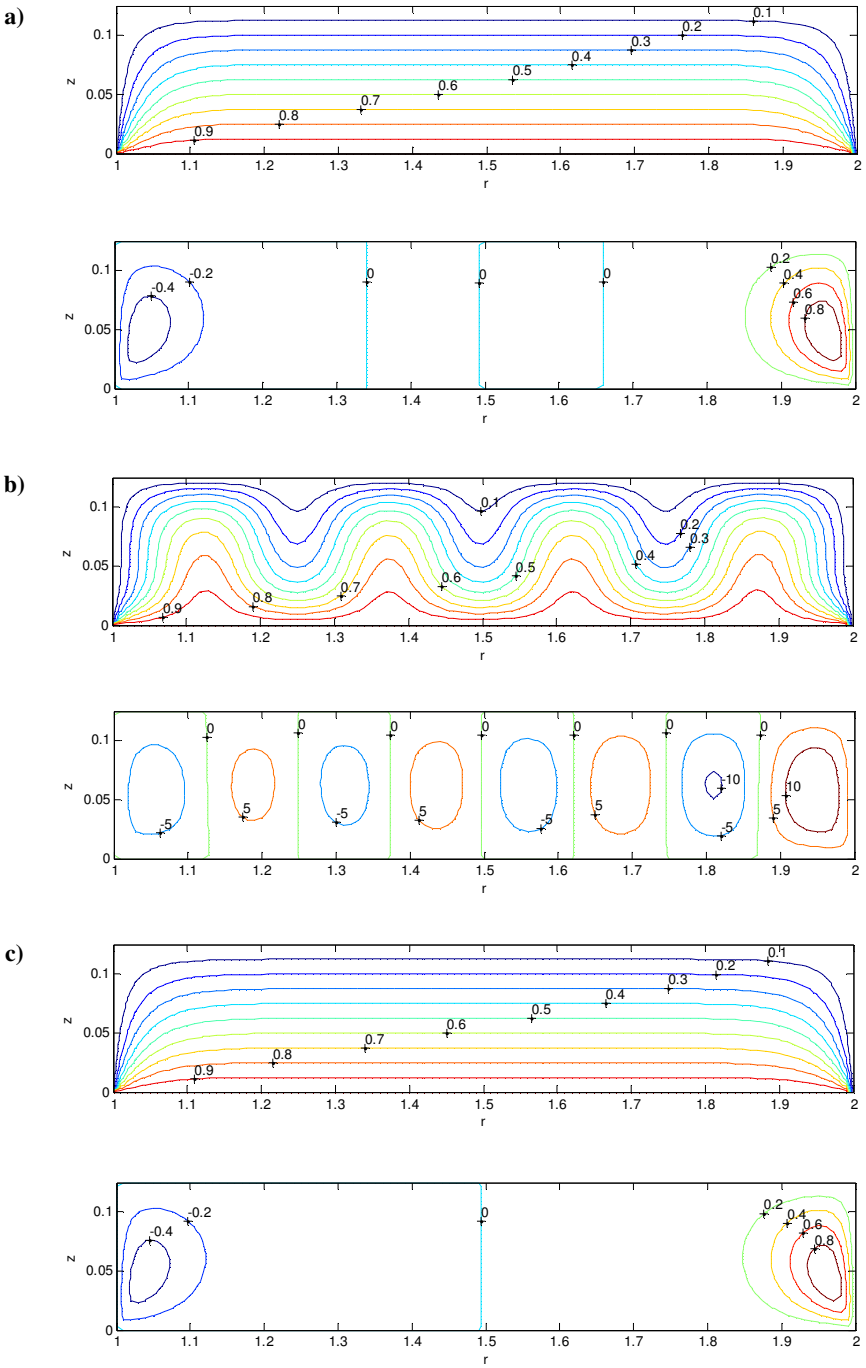

Figure 26: Isotherms and streamlines for a flat geometry (*Ar* = 0.125 and *Rr* = 1) a) *Ra* = 100 and *Rd* = 1; b) *Ra* = 1000, *Rd* = 1; and c) *Ra* = 100, *Rd* = 10

The increase Rayleigh number also has a major effect on the isotherms and streamlines. The effects of *Ra* are best observed in the flat geometry in *Figure 26b*. As *Ra* is increased from 100 to 1000, *Ar* = 0.125, *Rr* = 1, and *Rd* = 1. The isotherms transform from linear gradients to a wave pattern as *Ra* increases. The flat isotherms

at Ra = 100 transform in to a two-peak wave at Ra = 600 and then a four-peak wave at $Ra \geq 800$. This is a result of an imbalance in the buoyancy and viscous effects as reported by Silano et al. [19] who conducted numerical simulations of Rayleigh-Bénard convection for a range of Rayleigh numbers. Rayleigh number is related to the fluid layer thickness which results in a temperature difference. A rise in Ra indicates a break down in fluid layers forming smaller counter rotating cells. Each interface of two cells either raises hot fluid or lowers the cold fluid. This results in a wave like pattern of isotherms with successive concentrations of hot and cold pockets. The wave pattern is also reported by Sezai et al. [21] for a flat rectangular cavity heated from below and cooled from all other boundaries. The number of peaks in the isotherms is related to the number of cells present in the flow. The correlation can be seen in *Figure 26b*. Additionally, the wave pattern exists in local Nu for top and bottom walls also. It shows that a point of high heat transfer at the hot wall corresponds to a low heat transfer at the top wall (see *Figure 41*). It should be noted that since there was no external heat flux, all temperatures are within 1 and 0. Although the asymmetry still exists with the stronger flows at the outer boundary compared to the inner, the flow intensity in the middle of the cavity is much less compared to the side walls. This is explained by looking at the average Nusselt numbers for the inner, outer, and top walls. The $\overline{Nu}_o$.is 1.7% less than $\overline{Nu}_i$.while it is 56.1% greater than $\overline{Nu}_t$. The heat flux at the inner and outer boundaries is much higher compared to the top. This is rightly so because the surface area of the side walls is much smaller compared to the top wall. Therefore, the convection near the outer and inner boundaries is much greater compared to the middle of the cavity.

It is also interesting to note that the increase in *Ra* has the biggest effect on $\overline{Nu}_t$. After all, the top wall has the biggest surface area to reject heat. As *Ra* increases, the Nusselt number at the top wall increases 6.7 times while only increasing by 1.2 times at the side walls for the square geometry (see *Figure 28*).

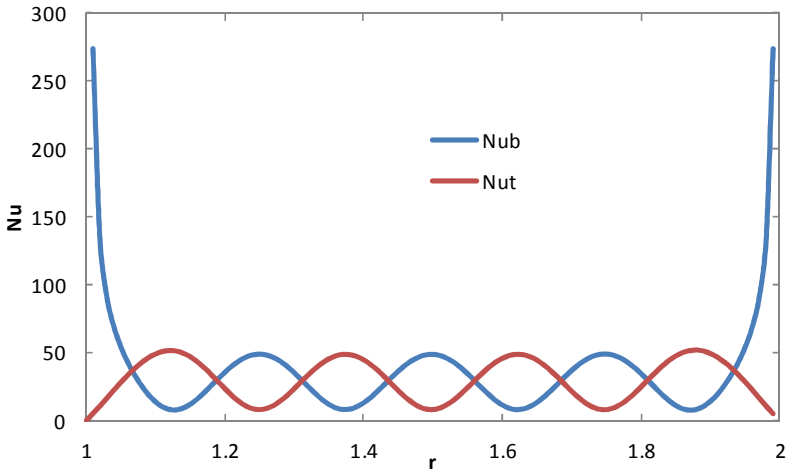

Figure 27: Local *Nui* with variation in *r* axis for the top and bottom walls.

Unlike *Ra*, the effects of *Rd* are best observed in the square geometry with $Ar = 1$ and $Ra = 100$ while *Rd* is varied from 1 to 10. The increase in *Rd* causes the isotherms to move closer to the bottom wall as seen in *Figure 25c*. The temperature gradient in the upper half of the cavity decreases while the opposite is true for the bottom half. The temperature gradient in the horizontal direction decreases slightly as well. Increase in *Rd* increases the effects of conduction resulting in quick heat rejection at the top and side walls. The uniformity in temperature gradient results from the conduction effects.

As conduction effects grow, convection effects diminish. This is clearly evident by the decrease in intensity of the flow. The cells shrink about 20% in from $Rd = 1$ to $Rd = 10$. The *u* velocities in the top region decrease about 50% while the velocities on the sides and below the cell remain constant. There is no change in the number of

cells from the original two cells. Although in the flat geometry, the flow reduces from a four cell flow to two cells. This is an indication of a reduction in conduction effects as well. There is a sharp increase in Nusselt numbers with the increase of *Rd*. For the flat geometry, the average Nusselt numbers for all four walls jump by a factor of 6.2 as seen in *Figure 29*. This is a verification of an increase in conduction throughout the cavity.

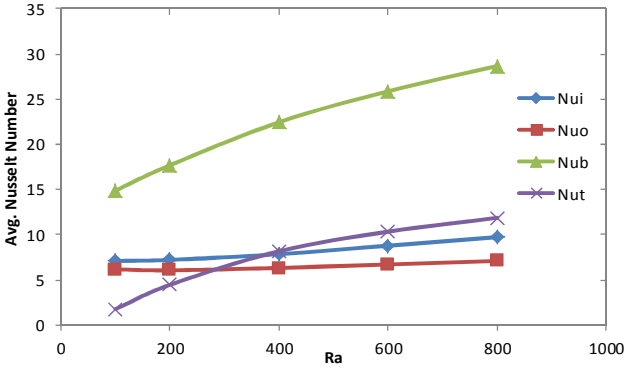

Figure 28: $\overline{Nu}$ with varying *Ra* for all four walls.

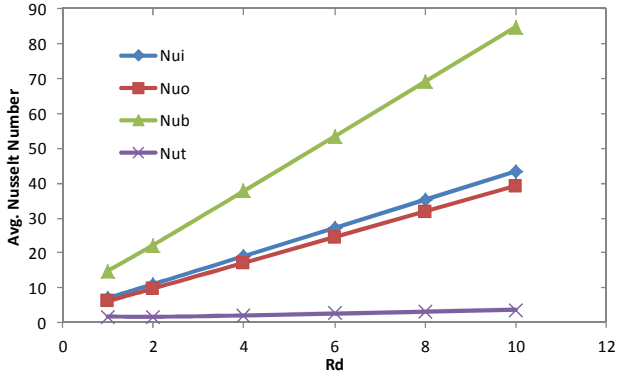

Figure 29: $\overline{Nu}$ with varying *Rd* for all four walls.

The Rayleigh- Bénard problem demonstrates the effect of conduction and convection very clearly. The variation in Rayleigh number shows how convection can affect the heat transfer inside the cavity while variation in *Rd* shows the effects of conduction. In this problem the effects of conduction produce about 6.2 times higher heat flux averaged over the top and side walls compared to convection.

6.1.2 Modified Rayleigh-Bénard Problem

The next step in the axial heating study is to modify the Rayleigh- Bénard problem by replacing the constant temperature T_H on the bottom wall with a non-dimensional heat flux $\bar{q}$. The schematic is shown below.

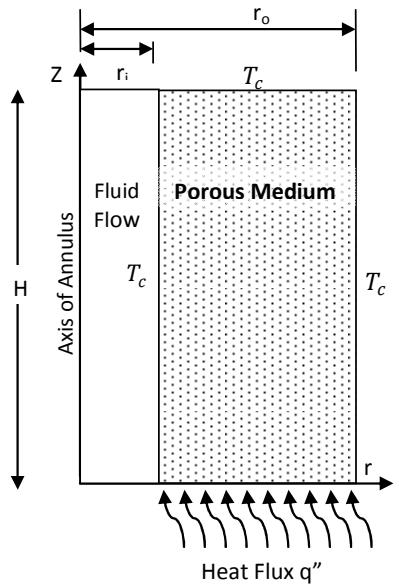

Figure 30: Modified Rayleigh- Bénard Problem

The boundary conditions for this experiment are listed below:

$$\text{At } \bar{r} = \bar{r}_i, \quad \text{and} \quad \bar{r} = \bar{r}_o \qquad \bar{T} = 0, \qquad \bar{\psi} = 0 \tag{6.4}$$

$$\text{At } \bar{z} = 0 \qquad \frac{\partial \bar{T}}{\partial \bar{r}} = \bar{q} \qquad \bar{\psi} = 0 \tag{6.5}$$

$$\text{At } \bar{z} = Ar \qquad \bar{T} = 0, \qquad \bar{\psi} = 0 \tag{6.6}$$

In these boundary conditions, $\bar{q} = -1$ since there is a heat flux present in this experiment. The ΔT is based on *Equation 3.12*. The square and flat geometries are sufficient in demonstrating the effects of conduction and convection. Some very interesting behavior is observed in the local Nusselt number at the walls as geometries are changed. The values used for all the parameters in this experiment are shown below.

Table 5: Values for non-dimensional parameters.

Ar	0.125	0.2	0.25	0.5	1	
Rr	1					
Ra	100	200	400	600	800	1000
Rd	1	2	4	6	8	10

The discussion begins by observing the reference square geometry ($Ar = 1$). Compared to the original Rayleigh- Bénard problem, the current results show isotherms in a more circular pattern. It can be seen in *Figure 31a*, that a temperature gradient exists in the bottom 70% of the cavity. The maximum temperature for this simulation is $\bar{T}_{max} = 0.4$.

The flow is in a bi cellular counter rotating regime with a stagnation point at the interface of the two cells. The average magnitude of the *u* velocities above both cells is about 66.67% greater in the outer region compared to the inner. The size of outer cell is about 23% greater than the inner cell.

The general behavior of this simulation can be understood by comparing the boundary conditions between the current problem and the original Rayleigh- Bénard problem. At the bottom wall, the heat flux is held constant in this problem while the temperature was held constant in the previous problem. Maintaining a constant temperature requires much more energy input compared to maintaining a constant heat flux. This is because the other three walls are rejecting heat at an equivalent rate and therefore there is minimal room for energy storage. This is evident by the $\overline{Nu}_b$ value which is 7 times less compared to the previous problem. The current *En* value for the bottom wall of 9.307 is compared to $En_b = 60.36$ in the previous problem. A low maximum temperature of $\bar{T}_{max} = 0.4$ is also a proof that there is minimal heat storage within the cavity. Additionally, a lower heat flux is the reason for smoother isothermal patterns within the cavity.

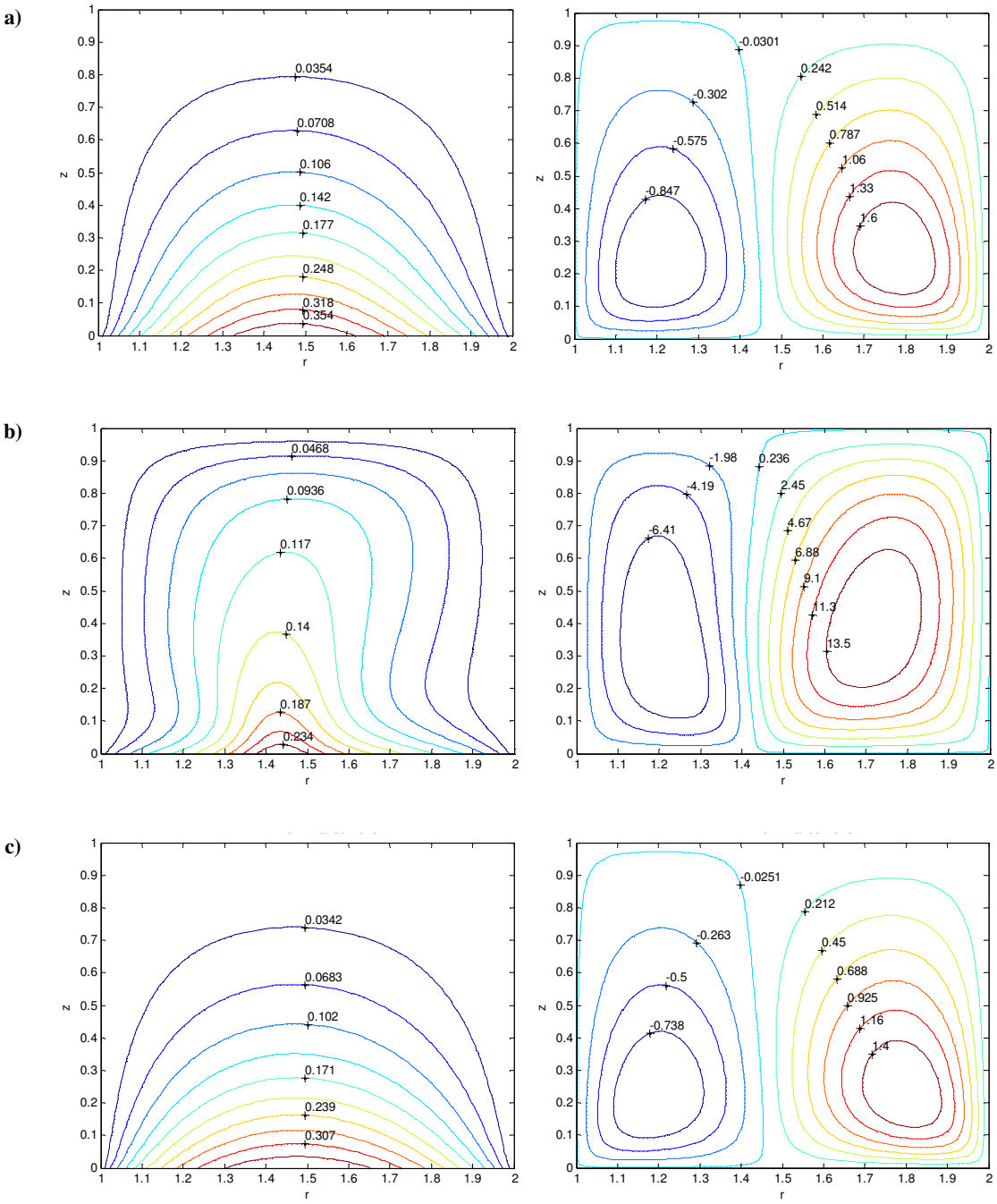

Figure 31: Isotherms and Streamlines for a square geometry (*Ar* = 1, *Rr* = 1) with a) *Ra*=100, *Rd*=1; b) *Ra*=1000, *Rd*=1; and c) *Ra*=100; *Rd*=10

As the *Ar* decreases, the isotherms flatten out. At *Ar* = 0.125, the isotherms lie flat in the *r* direction for almost 80% of the inner region while only curving near each of the side walls (*Figure 34*). Uniformly structured thermal layers in the fluid are clearly visible. As *Ar* changes, these fluid layers stay intact and do not mix at all. This is

because the incoming heat flux is so small that there is not a big density gradient in the cavity. The relatively small size of the side walls results in minimal heat transfer from those walls. Therefore the temperature gradient in the horizontal direction is almost non-existent.

The flow remains bi cellular. Unlike the Rayleigh- Bénard convection, there is no further bifurcation in the flow based on *Ar*. This is due to the same reason explained above. The vertical temperature gradient is 6.85 times smaller than for Rayleigh-Bénard problem. The density gradient in the fluid is not strong enough to overcome viscous and gravitational effects of the system. The *w* velocities in the middle of the cavity decrease by a factor of .007 while the *u* velocities above the cells increase by a factor1.32. The *w* velocities are the most sensitive to height change.

The effect of *Ra* and *Rd* can be best observed in the square geometry show in *Figure 31*. There is not much change in the square geometry due to the low heat flux. The Rayleigh number is increased from 100 to 1000 while $Ar = 1$, $Rr = 1$, and $Rd = 1$. Similar to the Rayleigh-Bénard problem, the isotherms start off in a parabolic shape. As *Ra* increases, the shape transforms into a one-peak wave pattern. Hot fluid rises quickly reaching up to $z = 0.9$ (as can be seen in *Figure 31b*). The temperature on sides quickly escapes the through the side walls. A cold spot emerges near the bottom of both side walls due to the mixing of descending cold fluid from the top and drastic cooling of the fluid at the bottom wall next to the cold wall. The cell in the outer half of the annulus is about 2.5 times the size of the inner cell. The *w* velocities increase by a factor of 8 while *u* velocities increase by 2 as *Ra* increases from 100 - 1000.

The increased intensity of the flow affects the heat transfer at the top and side walls. The bottom wall maintains a constant Nusselt number since it experiences a constant heat flux. The Nusselt number at the top wall increases by a factor of 3.51. As the fluid rises from the middle of the cavity, it first contacts the top wall and then the side wall. Therefore, the increase in *Ra* leads to higher velocities and in turn leads an increase in thermal transport to the top wall. Furthermore, as $\overline{Nu}_t$ increases, $\overline{Nu}_i$ and $\overline{Nu}_o$ decrease by 22% and 30% respectively to maintain energy balance (see *Figure 32*). Despite the decrease, the highest heat transfer happens through the outer wall since it has largest the surface area in the square geometry.

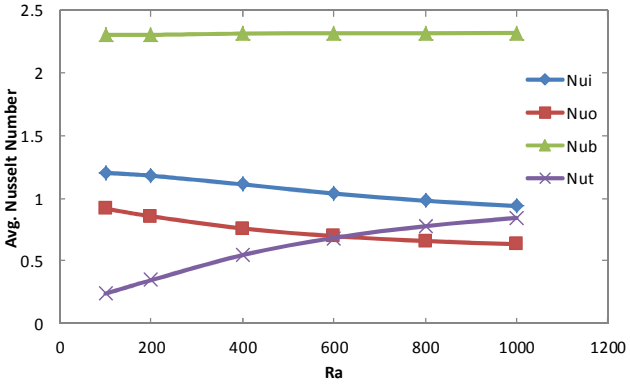

Figure 32: $\overline{Nu}$ with variations in *Ra* for all four walls.

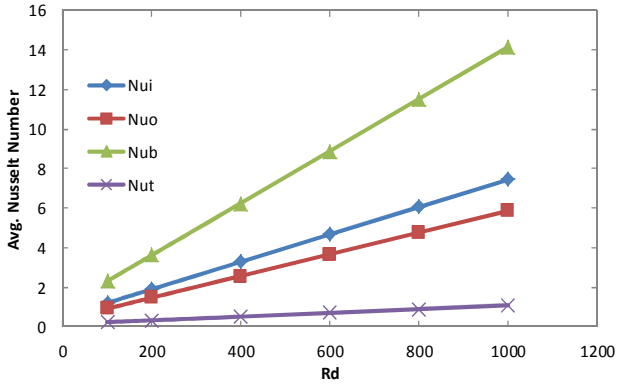

Figure 33: $\overline{Nu}$ with variations in *Rd* for all four walls

The Radiation parameter is increased from 1 to 10 while $Ar = 1$, $Rr = 1$, and $Ra = 100$. Similar to the previous problem, the isotherms contract and move closer to the bottom wall. This is because an increase of *Rd* causes an increase in conduction effects which causes the temperature gradient to become more uniform in all directions. The intensity of the flow decreases. Both cells' sizes decrease by 20%. The Nusselt number at the bottom wall increases by 6.14 while the maximum temperature increases by about 3% which can be considered a negligible a change. This increase in $\overline{Nu}_b$ is due to the *Rd* in the k_{eff} equation. The change in temperature

is due to the ΔT equation. As Rd increase, ΔT decreases, which ultimately results in a rise in $\bar{T}$.

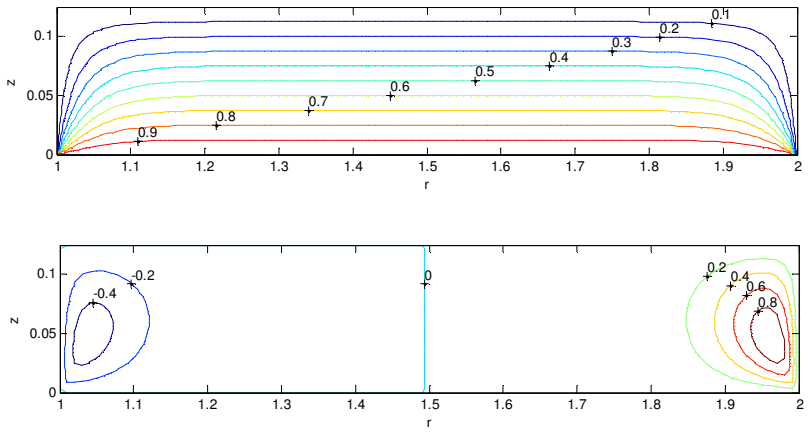

Figure 34: Isotherms and Streamlines for a flat geometry (Ar = 0.125, Rr = 1) with Ra=100 and Rd=1.

If there is an increase in the heat flux at the bottom wall, then the heat flux at the other walls has to increase as well. The Nusselt number at the top wall increases by a factor of 4.51. While $\overline{Nu}_i$ and $\overline{Nu}_o$ increase about 6.2 times (see *Figure 33*). This shows that unlike convection, conduction effects spread out in all directions despite flow patterns. The heat flux at the side walls grows more than the top wall because the side walls are closer to the bottom wall compared to the top wall. More heat escapes through the side walls.

The modified Rayleigh Bénard problem shows how the behavior of natural convection can change when a heat flux is added to the bottom wall. A constant heat flux at the bottom wall results in lower regional temperatures compared to a constant temperature. It is also interesting to note that the increase of Rd brought negligible change in ΔT. The increase of Ra lowered the maximum temperatures by 33%. The Rayleigh number mostly affected the heat transfer at the top wall while Rd directly affected the heat transfer at the bottom wall and therefore indirectly affecting the heat transfer at the other walls.

6.2 Main Analysis Bottom Heating

This experiment is the main part of the bottom heating analysis. The bottom surface is heated in the positive z direction. The outer and top boundaries are adiabatic while the inner surface is held constant at temperature T_c.

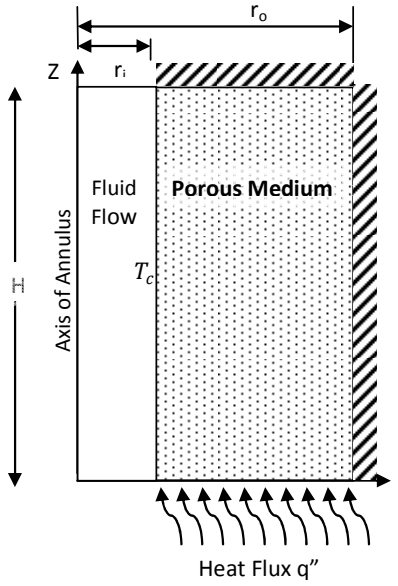

Figure 35: Vertical porous annulus with bottom heating.

The boundary conditions for this experiment are listed below:

$$\text{At } \bar{r} = \bar{r}_i, \qquad \bar{T} = 0, \qquad \bar{\psi} = 0 \tag{6.7}$$

$$\text{At } \bar{r} = \bar{r}_o, \qquad \frac{\partial \bar{T}}{\partial \bar{z}} = 0 \qquad \bar{\psi} = 0 \tag{6.8}$$

$$\text{At } \bar{z} = 0 \qquad \frac{\partial \bar{T}}{\partial \bar{r}} = \bar{q} \qquad \bar{\psi} = 0 \tag{6.9}$$

$$\text{At } \bar{z} = Ar \qquad \frac{\partial \bar{T}}{\partial \bar{z}} = 0 \qquad \bar{\psi} = 0 \tag{6.10}$$

This experiment was conducted for variations in *Ar, Ra*, *Rd* and *Rr* while $\bar{q}$ = -1. The standard grid size was 81 nodes per axis. It was varied from 41 to 161 nodes per axis depending on the axis length and the value of *Ra*. Higher *Ra* values required higher grid sizes for proper convergence. Similar to the modified Rayleigh-Bénard analysis,

the flow in this study is driven by a temperature gradient created by an incident heat flux (see *Equation 3.12*). The table below shows the range of all the variables used.

Table 6: Values for non-dimensional parameters.

Ar	0.125	0.2	0.5	1	2	4	6	8	10
Ra	100	200	400	600	800	1000			
Rd	1	2	4	6	8	10			
Rr	0.25	0.5	1	2					

This particular study involves three geometries (square, flat, and tall). Comparison of the three geometries will allow for a more broad analysis. The discussion will begin with the analysis of variations in *Ar*, then move on to the effects of *Ra* and *Rd* on the three geometries, and finally the effects of *Rr* are analyzed.

6.2.1 Aspect Ratio Analysis

This experiment analyzes the effect of height on the heat transfer within the cavity. In this analysis, heat is entering from the bottom wall and exiting at the inner wall since the top and side walls are adiabatic. Therefore, the temperature gradient in the inner half of the annulus is higher compared to the outer half. Moving up the z axis in the inner half, the isotherms first run toward the outer wall then suddenly change direction towards the inner wall (as seen in *Figure 36a*). Studies on natural convection in rectangular enclosures with bottom heating by November et al. and Ganzarolli et al. [24], [32] state that the isotherms spread in the lower outer quadrant due to the rise of the warm fluid along the adiabatic wall away from the hot surface (similar to *Figure 36a*). The outer top quadrant of the cavity maintains a uniform temperature due to the junction of two adiabatic walls at that corner. The maximum temperature is $\overline{T}_{max} = 0.812$ located in the outer bottom corner because it is the junction of the incident heat flux and the insulated boundary.

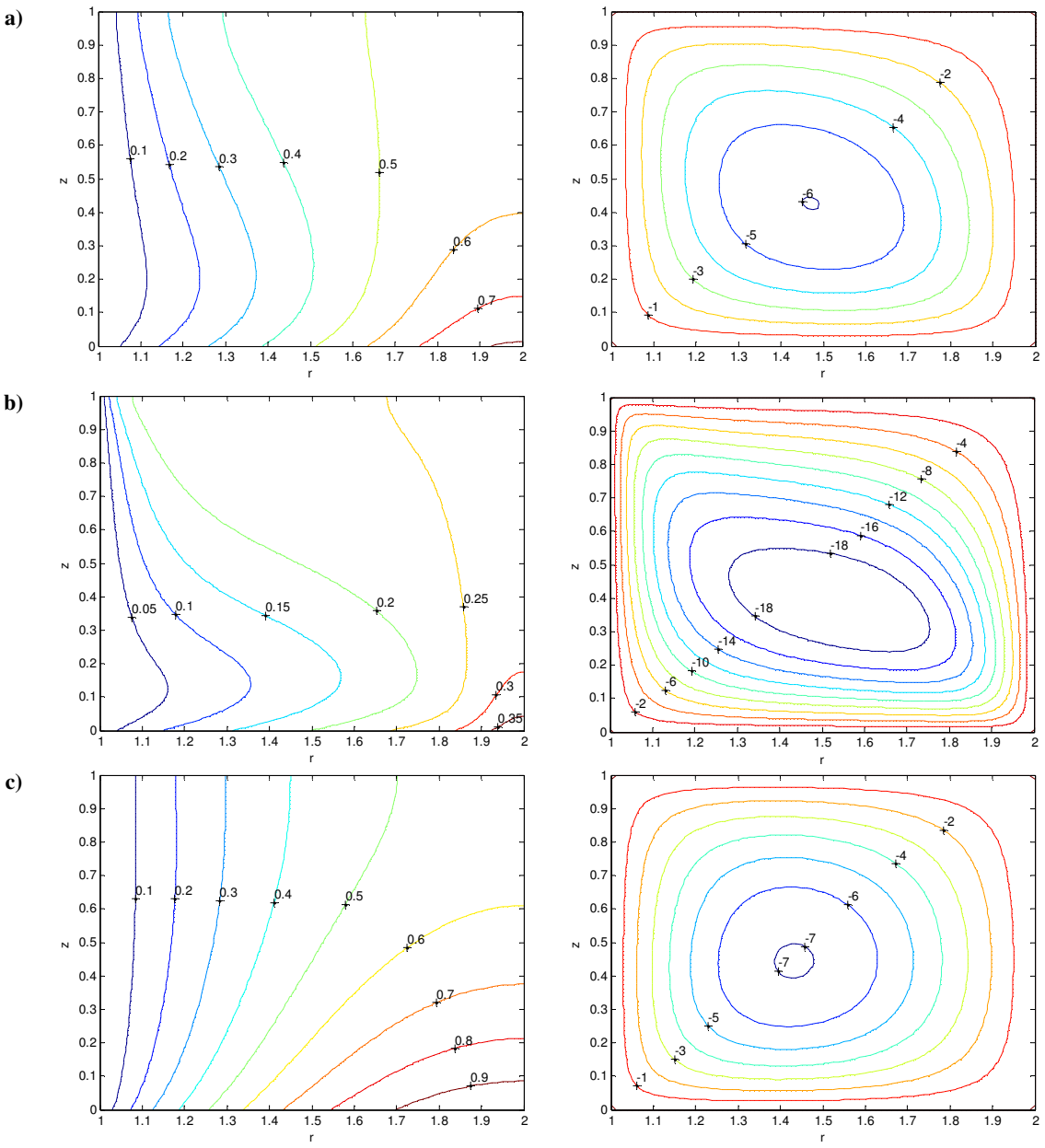

Figure 36: Isotherms and streamlines for a square geometry (*Ar* = 1 and *Rr* = 1) a) *Ra* = 100 and *Rd* = 1; b) *Ra* = 1000, *Rd* = 1; and c) *Ra* = 100, *Rd* = 10.

The flow is unicellular with the hot fluid rising at the outer wall and falling at the inner wall as it cools down. The center of the cell is stretched in the diagonal direction towards the top cold wall and bottom outer wall [32]. The cell is located at $z = 0.4$. For $z > 0.4$, the fluid flows towards the inner wall causing the isotherms to fall back towards the inner wall. The strongest velocities are present at the outer boundaries. The magnitude of the average u velocity in the bottom region is about 1.3

times greater than its counterpart in the top region. This is due to the heat flux located at the bottom wall. Similarly, the magnitude of the average *w* velocity in the inner region is about 1.25 times greater compared to the outer region.

The high temperature gradient near the inner wall indicates that a high heat flux is present at the inner wall. This is confirmed by looking at the Nusselt numbers $\overline{Nu}_i$ is about 50% greater than $\overline{Nu}_b$. This is the result of the difference in the bottom and inner wall surface areas. The surface area of the inner wall is 50% less than the bottom therefore it needs to have a 50% higher heat flux to maintain a zero net energy balance. The *En* number remains constant for all *Ar* values since neither the heat flux nor the effective area changed (see *Figure 37*). The accuracy of the results is noted by the error for energy balance in this experiment of 0.17%.

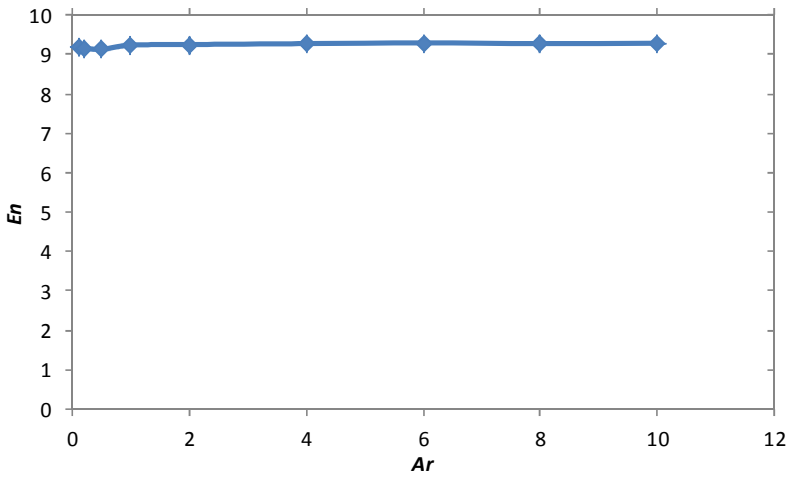

Figure 37:*En* number with variations in *Ar*.

The local heat fluxes in *Figure 41* show a pattern very similar to the isotherms. The heat flux begins at *Nui* = 5.54 at z = 0.125 and decrease to *Nui* = 2.15 at z = 0.2, then increases to *Nui* = 5.89 at z = 1. This shows that there is almost conduction like behavior near the bottom of the inner wall, at the junction of hot and cold boundaries. Then the heat flux reduces due to convection effects moving the fluid away from the

cold wall. Finally, the highest heat flux is present near the top of the inner wall where hot fluid meets the cold wall.

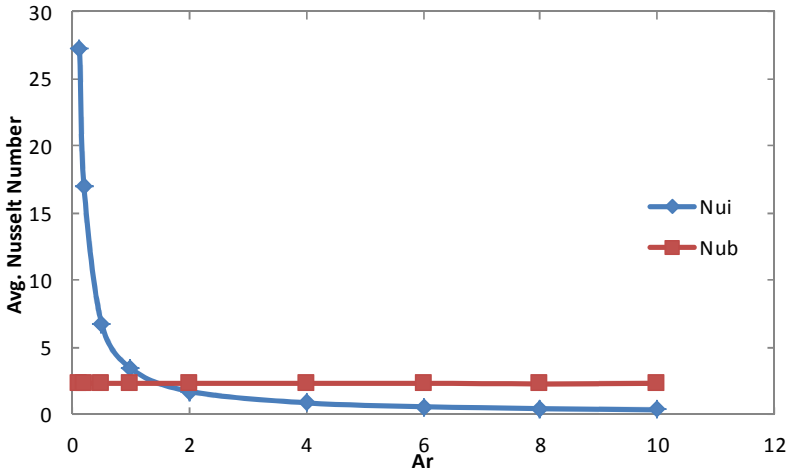

Figure 38: $\overline{Nu}$ with variations in *Ar*

As *Ar* decreases from 1 to 0.125, the isotherms shift towards the inner wall and straighten out vertically. Due to the heat flux on the bottom wall and a small height, the entire cavity becomes thermally active. The temperature gradient is higher near the inner boundary [24]. As seen in *Figure 42a*, the maximum temperature rises by a factor of 5.8 to $\bar{T}_{max} = 4.69$. The reason for this behavior is the decrease in height of the inner wall. As the surface area of the inner wall decreases the heat flux at that wall has to increase to compensate for the incoming heat. Keep in mind that neither the heat flux nor the surface area at the bottom wall is changed. The result is an almost conduction like behavior where the heat is escaping out the inner wall with a uniform temperature gradient along the z axis. This behavior is confirmed with an increase in $\overline{Nu}_i$ by a factor of 8, as *Ar* decreases from 1 to 0.125. At the same time, $\overline{Nu}_b$ has negligible change (*see Figure 38*). Additionally, *Figure 43* shows that *Nui* rises by 77% travelling in the positive z axis at the inner wall. Although a slight dip in *Nui* is present for low z ($z \approx 0.01$). This means there is very little heat escaping from the hot

and cold wall corner. Most of the heat in the outer half of the annulus rises and travels the upper wall towards the cold wall.

This behavior is also reflected in the flow profile. The core of the cell moves close to the inner wall although the entire cavity experiences a flow [32]. On average, the magnitude of u velocities in the bottom and top regions increases by a factor of 1.25. On the other hand, the magnitude of average w velocities decreases by a factor of 1.2 in the inner region and a factor of 8.75 in the outer region. Due to the large radius to height ratio and the insulated top and outer walls, about 70% of the region from the outer boundary only experiences fluid buoyancy while the rotation happens in the rest 30% of the cavity closest to the inner wall. The decrease in the average magnitude of velocities indicates that there is not enough vertical area for the flow to develop. Secondly, as Ar increases from 1 to 10, the isotherms contract and move closer to the outer bottom corner. As seen in *Figure 45a*, about 65% of the cavity is at a uniform temperature $\bar{T} = 0.1$. The temperature gradient is mostly concentrated in the outer bottom corner as well. The maximum temperature falls by 7% to $\bar{T}_{max} = 0.75$. The temperature gradient in the bottom region $0 \leq z \leq 1$ looks very similar to that of a square cavity. For $1 \leq z \leq 2.8$, the isotherms bend towards the adiabatic wall. Finally for $2.8 \leq z \leq 8$, a uniform temperature of $\bar{T} = 0.1$ is present. For Ar values from 1-10, the temperature gradient is always concentrated between $0 \leq z \leq 3$. This means that heat transfer is only happening in that region while everywhere else on the boundary the heat flux equals zero. This behavior can be seen in the *Nui* plots in *Figure 44* where *Nui* drops to almost 0 for $z \geq 4$.

In conclusion, $\overline{Nu_i}$ is the highest for the flat geometry and drastically decreases until $Ar = 1$ then decreases at a very slow rate for $Ar \geq 1$. This is because for $Ar \geq 4$, the area of the inner wall becomes more than 2.5 times greater than the area of the bottom wall. For $0.125 \leq Ar \leq 1$, the $\overline{Nu_i}$ gradient, which is defined as $(\Delta\overline{Nu_i}/\Delta l)$ where l is the respective distance, is 27.28 while for $1 \leq Ar \leq 8$, the $\overline{Nu_i}$ gradient is 0.34. Overall $\overline{Nu_i}$ decreases by 89% for $1 \leq Ar \leq 10$. The bottom Nusselt number on the other hand remains constant for all Ar. The Energy number for both walls remains constant for all Ar values.

The maximum temperature is the highest for the flat cavity (see *Figure 39*). The temperature curve for all Ar values can be seen here. The curve is very similar to the $\overline{Nu_i}$ curve. This is because as the inner wall increases, the heat removal area increases allowing for higher bulk heat removal and reducing heat storage within the cavity.

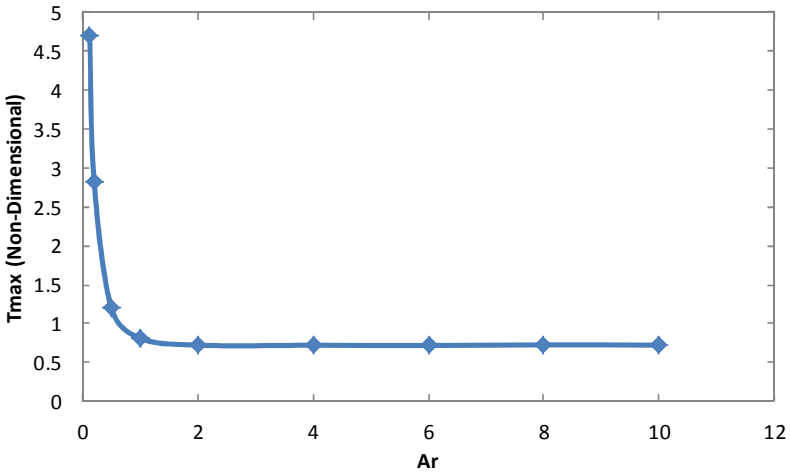

Figure 39: $\bar{T}_{max}$ with variations in Ar.

Although the flat cavity has a high $\overline{Nu}$, its small effective height makes it inefficient to use. On the other hand, it can be seen by inspection of the isotherms and local *Nui*, that the tall geometry is very inefficient. The temperature gradient only exists for the bottom 30% of the cavity. For the solar tower receiver application, Aspect ratio

between $0.25 \leq Ar \leq 1$ seems to deliver sufficient heat flux with an appropriate sized effective boundary.

6.2.2 Rayleigh Analysis

The Rayleigh number is increased from 100 to 1000 while $Rr = 1$ and $Rd = 1$ for the three geometries. Similar to the Ar analysis, the reference analysis is done on the square cavity where $Ar = 1$. The increase of Ra results in an intensification of the convection effect on cavity. This is clearly evident by the bending of the isotherms. From visual inspection of *Figure 36b*, the slope of the isotherms between $0 \leq z \leq 0.15$ decreases about 70%. The opposite happens from $z > 0.2$.This is due to the reaction of isotherms to the rapid changing in the flow [32]. Although the overall temperatures of cavity also decrease, the temperatures near the cold boundary remain relatively constant [24]. The maximum temperature decreases 53%. As mentioned before, this is due to the interaction of Ra and ΔT. As Ra increases, ΔT increases, resulting in a decrease in local $\bar{T}$.

The high temperature gradient near the bottom and inner walls is due to the increased convection effects. On this topic, [32], [24], report that for natural convection in a clear fluid, there is a bottom heat layer that remains intact for the entire bottom wall for all Ra values whereas in the present case there is a clear temperature gradient on the bottom heated wall.

The flow starts with warm fluid rising along the hot wall and then turns toward the cold wall and descends along it. This flow causes pockets of high and low temperatures to occur in the bottom outer corner and the upper inner corner of the cavity respectively [32]. This is due to the warm fluid rising and compressing the

isotherms near the cold wall [24]. At very high values, *Ra* = 1000, the velocities increase so much that clear thermal boundaries are apparent (*Figure 36b*).

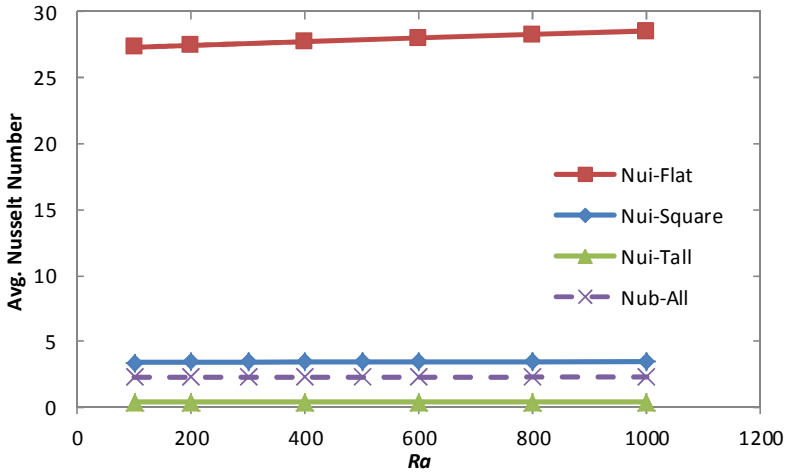

Figure 40: $\overline{Nu}_i$ with variations in *Ra*.

The velocities in the *w* direction increase by 5 times on average while the *u* velocities increase by about 4.5 times on average. There is an emergence of a boundary layer for $Ra \geq 600$ as the cell stretches diagonally to the top cold wall and the outer hot wall regions [32].

There is a negligible change of 1.26% in $\overline{Nu}_i$ and 0.42% in $\overline{Nu}_b$ as can be seen in *Figure 40*. At the bottom wall, $\overline{Nu}_b$ does not change since the heat flux there is held constant. Additionally, $\overline{Nu}_i$ also remains constant for the same reason as in the *Side Heating Analysis*.

As seen in *Figure 41*, in comparison to *Ra* = 100, Nu_i decreases in about the bottom half region of the inner wall but then increases in the top region, for *Ra* = 1000. This behavior is due the fact that higher convection effects lead to more hot fluid reaching the top of the inner wall. This behavior is similar to the one in *Radial Heating Analysis* for variation in *Ra*. There is a little increase in *Nui* at $z = 0.125$, indicating the conduction effects at the junction of hot and cold wall. The *En* number remains

constant for all *Ra* and *Rd* values for all geometries similar to the previous chapter (see *Figure 47*). The error in energy balance for this analysis is 0.28%.

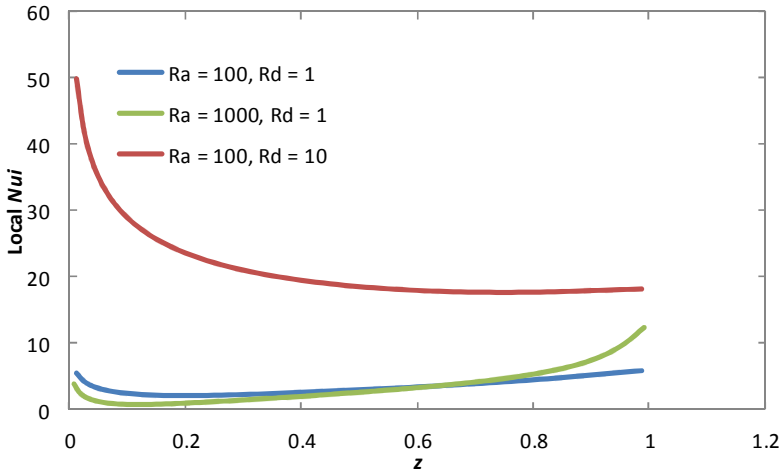

Figure 41: Local *Nui* along the *z* axis for a square geometry (*Ar* = 1).

The increase in *Ra* has similar results for the flat geometry ($Ar = 0.125$) compared the square geometry. Due to the small height, the flow expands to the entire cavity horizontally. As seen before, at $Ar = 0.125$, $Rr = 1$, $Ra = 100$, and $Rd = 1$, the isotherms are vertically straight with a high temperature gradient in the inner half of the region and core of the cell is right next to the inner wall. As $Ra \rightarrow 1000$, the isotherms bend towards the inner wall forming an "S" shape pattern similar to the square geometry. The flow in the upper part of the cavity compresses the flow in the lower part. The result is a stabilization of the vertical temperature gradient near the bottom wall where heat flux is present [24]. The maximum temperature decreases by 53%. The maximum temperature averaged for all *Ra* values is $\bar{T}_{max} = 3.22$; about six times greater compared to the one for square geometry. This overall increase of $\bar{T}_{max}$is due to characteristics of the flat geometry described in the previous analysis.

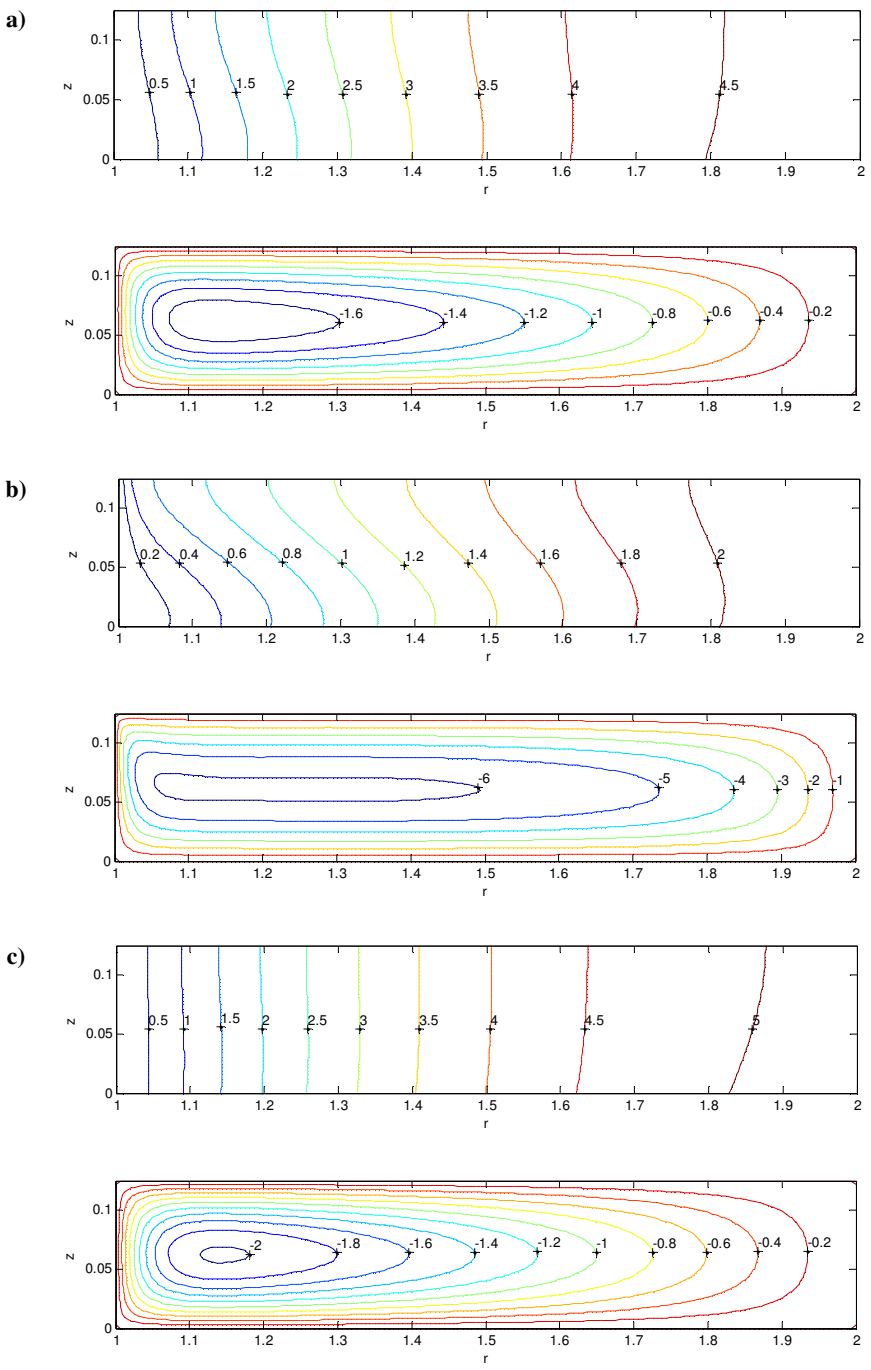

Figure 42: Isotherms and streamlines for a flat geometry (*Ar* = 0.125 and *Rr* = 1) a) *Ra* = 100 and *Rd* = 1; b) *Ra* = 1000, *Rd* = 1; and c) *Ra* = 100, *Rd* = 10.

As $Ra \rightarrow 1000$, the core of the flow intensifies and expands horizontally towards the outer wall. As seen in *Figure 42b*, the bump that appears in the inner upper region of cell is also seen in [24]. The gradient for *w* velocity is much higher at the inner wall compared to the outer wall. The effects of convection can be seen in the shift of the

core of the cell towards the inner wall. While the gradient for u velocity is the same at top and bottom walls. The w velocities near the cold wall are 10 times higher than the velocities on the outer side of the core. The magnitude of the u velocities is about the same on the top and bottom of the core. As $Ra = 100 \rightarrow 1000$, the velocities maintain the same ratio but decrease overall by a factor of 5.26. There is a 4.5% increase in $\overline{Nu}_i$ for the same change Ra (see *Figure 40*). Similar to the square geometry this change is negligible as well. The numerical error for flat geometry is higher since $\overline{Nu}_i$ is generally eight times greater for a flat geometry compared to the square geometry. The convections effects can be observed in *Nui* plots seen below in *Figure 43*. There is a drastic increase in *Nui* for $z \geq 0.08$. The *Nui* gradient for $0.08 \leq z \leq 0.125$ is 3.5 times greater than the gradient for $0 \leq z \leq 0.08$.

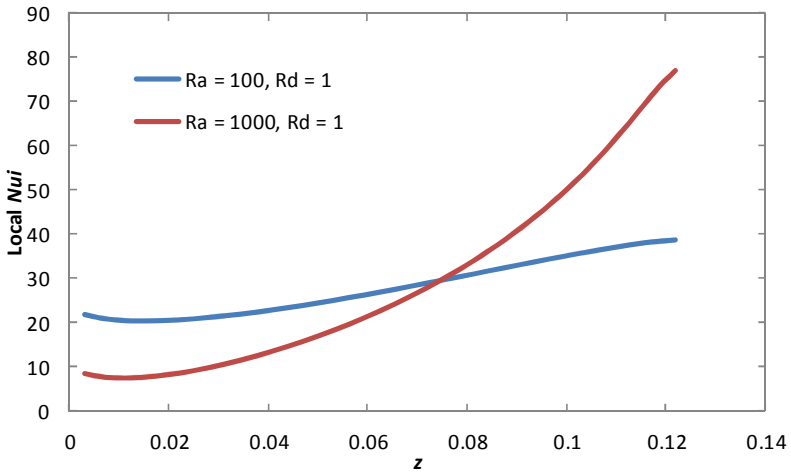

Figure 43: Local *Nui* along the z axis for a flat geometry ($Ar = 0.125$).

The effect of *Ra* on natural convection in the tall geometry ($Ar = 8$) causes the isotherms to spread out. This makes sense intuitively because as *Ra* increases from $100 \rightarrow 1000$, the fluid is able to rise higher. The isotherms in *Figure 45b* are almost flat near the bottom boundary then suddenly shift direction and run vertically going up the z mid plane. The reason for this behavior is due to the flow pattern described

later. Similar to the previous geometries, the increase in *Ra* causes the overall temperatures to fall. The maximum temperature falls by 55% ($\bar{T}_{max}$ = 0.72 → 0.32). The temperature gradient is high near the bottom wall. A ΔT of 0.15 exists for about upper 93% of the cavity.

The vertical velocity gradient expands by 2.3 times as *Ra* = 100 → 1000. The *u* velocities above the core increase by 5.5 times and 4.1 times below the core. The *w* velocities increase 4.1 times as well. The core of the cell remains near the bottom wall. This is because the fluid heats up near the bottom wall and rises up along the outer boundary. Due to the large surface area of the inner wall, the heat is extracted from the fluid before it even reaches half of the height of the annulus. Therefore the fluid cools down and begins to fall along the inner wall. This flow pattern is the reason for the almost horizontal isotherms near the bottom wall. The horizontal transport effect of *u* velocities near the bottom wall over power the vertical buoyancy effects. Additionally, boundary layers emerge at the inner and outer walls with high velocities at the bottom.

The change in $\overline{Nu_i}$ is negligible with an increase of 1.4%. The median Nusselt number for all *Ra* values is 0.43 as seen in *Figure 40*. While the bottom Nusselt number stays constant at 2.3. The ratio of $\overline{Nu_i}$ and $\overline{Nu_b}$ is in proportion with the surface areas of the respective surfaces. The most interesting plots are of the *Nui*. The curves seen in *Figure 44*, show that a substantial heat flux is only present up until *z* = 4 for *Ra* = 100. Unlike other geometries, the increase to *Ra* = 1000 causes the heat flux to gradually decrease across the entire *z* axis. This suggests that bottom heating is

not sufficient for a tall geometry. Most of the cavity has minimal heat transfer less $Nui = 0.5$.

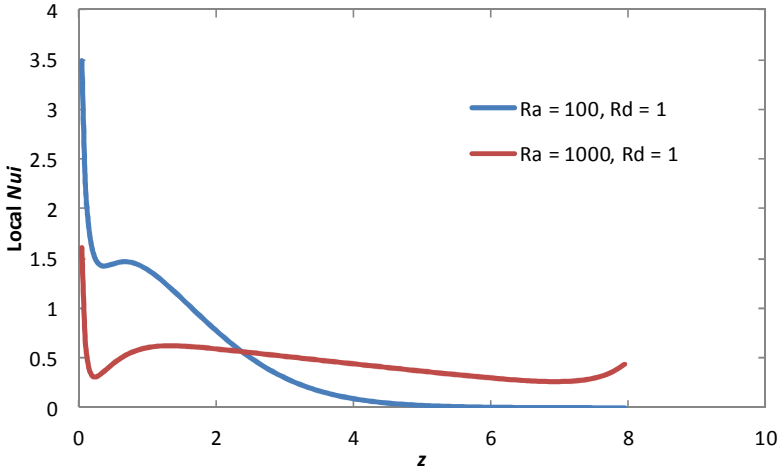

Figure 44: Local *Nui* along the *z* axis for a tall geometry (*Ar* = 8).

The increase of *Ra* has very similar results for all three geometries. The temperatures in all three geometries decrease by the same percentage. The velocities increase for all three geometries. The Nusselt numbers remain relatively constant for all boundaries in a particular geometry. The effects of convection are apparent for all three geometries. There is a major change in flow as *Ra* increases to 1000.

The local heat flux increases the most for the tall geometry. It can be seen in *Figure 44*, that *Nui* for *Ra* = 1000 is higher than the curve for *Ra* = 100 from $z \geq 2.5$. This is due to the expansion of the flow vertically in the tall geometry. It should also be noted that the magnitude of the heat fluxes for tall geometry about 80 times less than the flux for flat geometry.

The most favorable conditions for the current system would be to have high *Ra* values for geometries of $0.125 \leq Ar \leq 1$, where high heat fluxes can be achieved with a moderate size of effective surface.

6.2.3 Radiation Analysis

This analysis is conducted with range of $1 \leq Rd \geq 10$, with Rr =1, and Ra = 100. The reference square geometry (Ar = 1) is first analyzed then the extreme cases of flat (Ar = 0.125) and tall (Ar = 8). As $Rd \rightarrow 10$, the temperature gradient evens out throughout the cavity. It can be seen in *Figure 36c*, that at Rd = 10 the isotherms are in a diagonally symmetric distribution [32]. This is a clear indication of conduction improving in both r and z directions in the cavity. The heat enters from the bottom boundary then travels in a diagonal direction to the inner wall. The highest temperatures are concentrated in the bottom outer corner similar to previous analyses in this orientation. The maximum temperature rises 20% from $\bar{T}_{max}$= 0.812 → 0.9794. The reason for increase in $\bar{T}_{max}$ is the same as provided in the *Side Heating Analysis*, although in this case Rd does not increase the local temperatures, the effects of convection do.

The flow is in a unicellular regime. The core remains in the same place as the fluid heats up at the bottom wall then rises along the outer wall, then cools near the inner wall, and falls back to the bottom. The core transforms into a uniform circle which signifies the dominance of conduction effects [32]. The magnitude of u velocities increases 1.2 times on average while the magnitude of w velocities increases by 1.3 times on average. There is no change in velocities near the boundary.

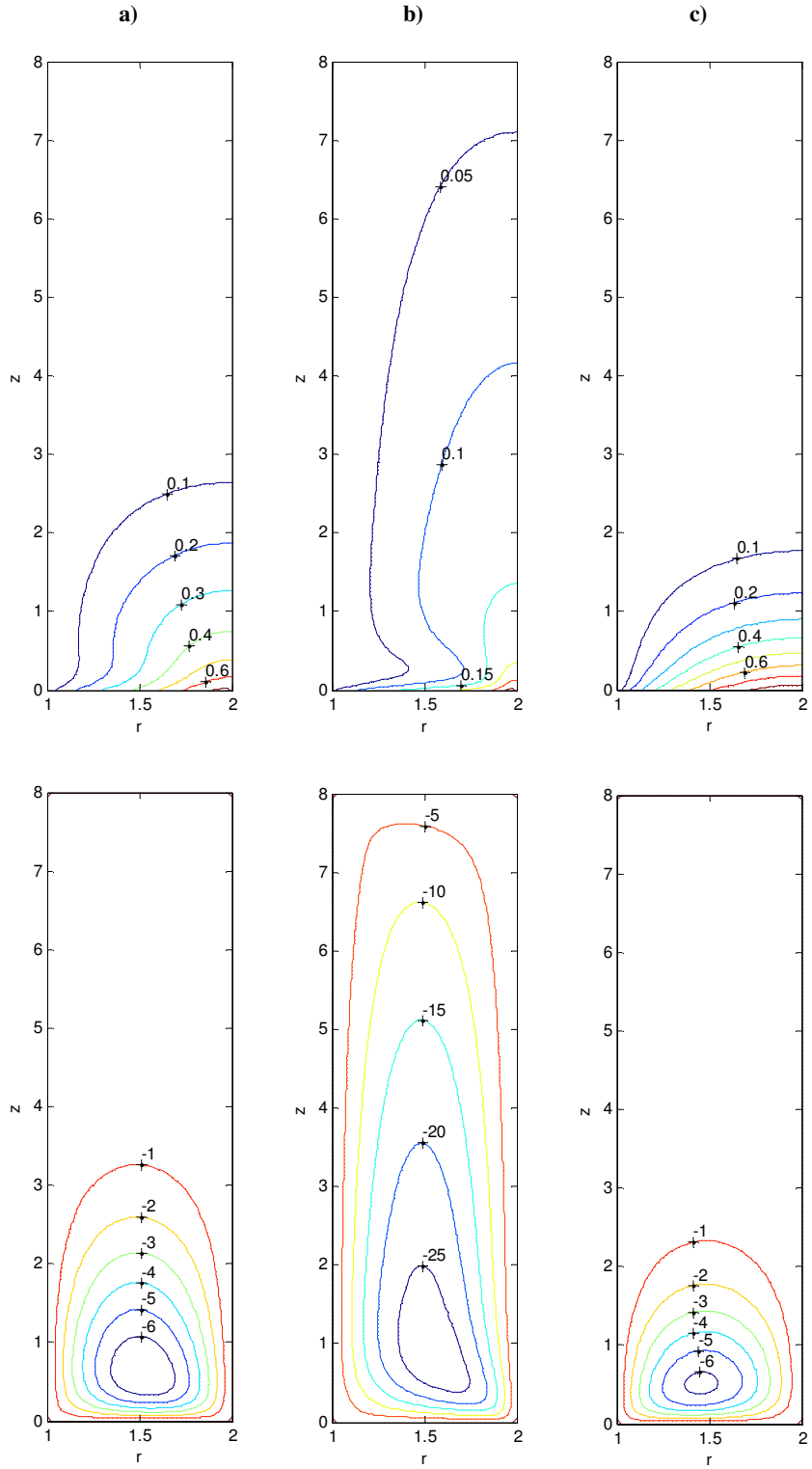

Figure 45: Isotherms and streamlines for a tall geometry (*Ar* = 8 and *Rr* = 1) a) *Ra* = 100 and *Rd* = 1; b) *Ra* = 1000, *Rd* = 1; and c) *Ra* = 100, *Rd* = 10

Both $\overline{Nu}_i$ and $\overline{Nu}_b$ increase by a factor of 6.14 as *Rd* increases from 1 → 10 (see *Figure 46*). This is because the term (1 + 4Rd/3) in the Nusselt number equation

increases 6.14 times for the same range of *Rd*. It can be seen in *Figure 38*, that the ratio of $\overline{Nu}_i$ /$\overline{Nu}_b$ = 1.5 and it remains constant for all *Rd* values. Additionally, it can be seen in *Figure 41* that *Nui* gradually decreases as z increases. This is a sign that most of the heat flux happens in lower region of the inner wall closest to the hot wall. When increasing between $0 \leq z \leq 2$, the heat flux reduces by 63.5%. The heat flux at z = 0.125 is *Nui* = 49.89, 9 times greater for *Rd* = 10 compared to *Rd* = 1. Similar to the *Rayleigh Analysis*, *En* remains constant as seen in *Figure 47*. Finally, the error of energy balance for this analysis averages at 0.84%.

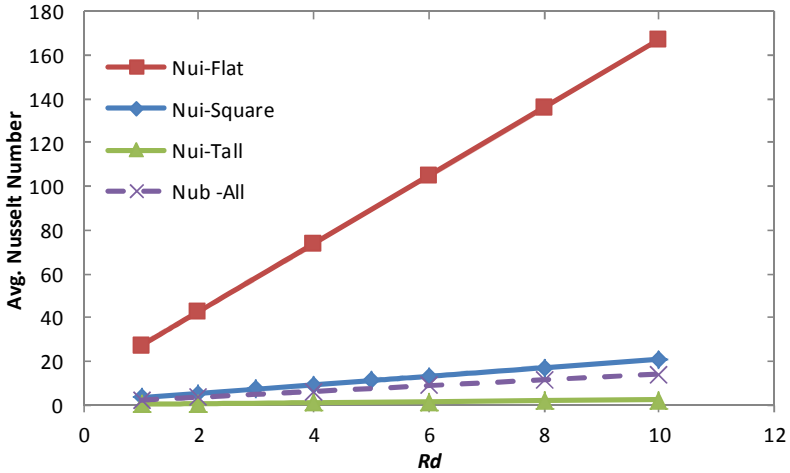

Figure 46: $\overline{Nu}_i$ with variations in *Rd*

The effect of *Rd* on the flat geometry in *Bottom Heating* is somewhat similar to the one in *Side Heating Analysis*. Rather than a fan shaped pattern, the isotherms become vertical spread out in the horizontal direction. The temperature gradient only exists in the horizontal direction and is higher in the inner half of the annulus. This is because of the limitations presented by small *Ar*. The heat enters the cavity through the bottom wall filling up the volume, and then collectively exits from the inner wall. This shows that high temperatures collect in the outer half due to insulation of the

outer and top walls. The maximum temperature is located at the outer boundary and increases by 9.2% ($\bar{T}_{max}$= 4.7 → 5.1).

The flow remains in a unicellular regime, with the core of the cell near the inner boundary. The *w* velocities along the inner wall are about 8 times greater than their counter parts to the right of the core. The magnitude of the *w* velocities increases 1.2 times on average as *Rd* increases from 1 to 10. On the other hand, the magnitude of *u* velocities is about the same for above and below the core. The average increase in magnitude of *u* velocities is by a factor of 1.7. The highest velocities are present near the inner wall verifying that the highest temperature gradient is located there. The outer half of the cavity experiences a low temperature gradient and therefore low velocities.

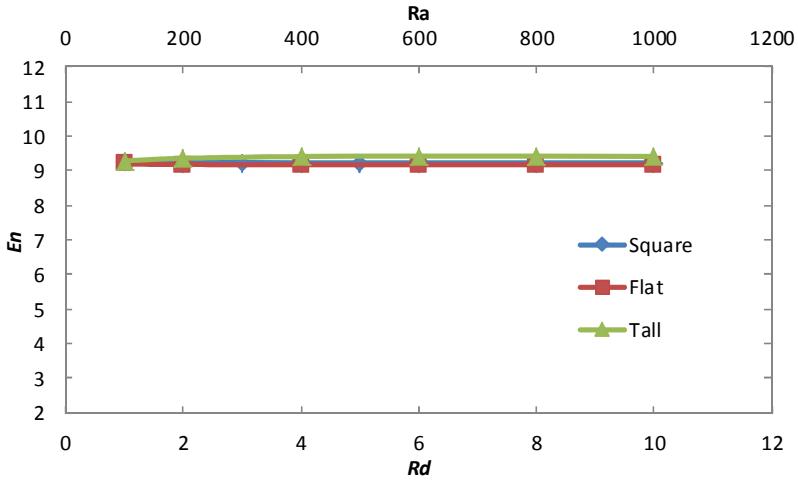

Figure 47: *En* number with variations in *Ra* and *Rd*.

Both Nusselt numbers for this geometry also increase 6.14 times. As usual, $\overline{Nu}_i$ is 11 times greater than $\overline{Nu}_b$ due to the decrease in *Ar*. Additionally, $\overline{Nu}_i$ and $\overline{Nu}_b$ stay in proportion to each other for all *Rd* values. The uniformity of the local heat flux can be seen in the *Nui* plots seen below in *Figure 48*. There is a slight decrease in the heat flux from $0 \leq z \leq 0.037$. This is because of the conduction effects at the inner bottom

corner. The increase in *Rd* causes the conduction at that corner to increase. This experiment is verified for accuracy by an average of 2% error in the energy balance.

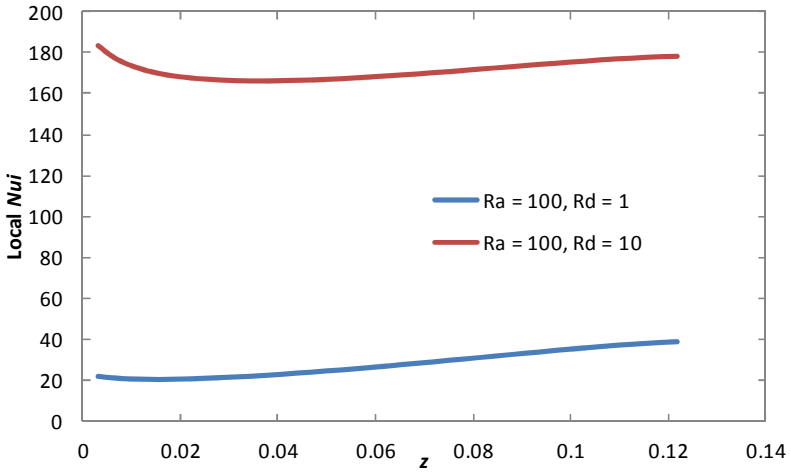

Figure 48: Local *Nui* along the *z* axis for a flat geometry (*Ar* = 0.125).

The fan shaped pattern of the isotherms in the square geometry is also seen in the tall geometry albeit, in the case of tall geometry, the isotherms are all concentrated on the bottom between $0 \leq z \leq 2$. As $Rd \rightarrow 10$, the isotherms contract by 21%. The temperature gradient is nonexistent for $z \geq 2$. As seen in *Figure 45c*, for $z \leq 2$, the temperature gradient is mostly vertical although a slight horizontal temperature gradient is observed near the inner wall due to heat escaping directly from the bottom wall to the inner wall. The maximum temperature increases by 18.4% ($\bar{T}_{max}$= 0.72 → 0.85).

The flow also shrinks about 28% for the tall geometry as *Rd* increases from 1 to 10. The core of the cell is near the bottom boundary. The *u* velocities increase about 28% between $6 \leq \psi \leq 1$, above the core. While decreasing 17.7 % between $1 \leq \psi \leq 0$ at the top wall. The magnitude of *w* velocities decreases about 25% on both sides of the core.

The average inner Nusselt number increases by 6 times while $\overline{Nu}_b$ increases by 6.14. The increase of $\overline{Nu}_i$ in tall geometry is less than the increase in the other two geometries because of a small vertical temperature gradient. The local *Nui* is zero for z ≥ 4. The mean value of the average Nusselt number over all *Rd* values for the tall geometry is $\overline{Nu}_i$ = 1.42. The decrease in local heat flux can be seen in *Figure 49* . The local Nusselt number decreases drastically as *z* approaches the top portion of the inner wall. The heat flux on the first node of the inner wall increases by 10.3 times for *Rd* = 10 compared to *Rd* = 1 Although the local heat flux is incredibly high for the lower region of the inner wall, the rest of wall from $z \geq 4$ has almost no heat flux.

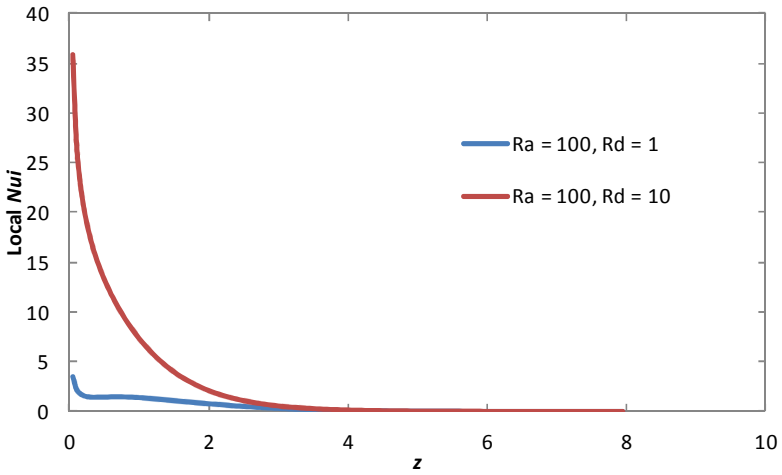

Figure 49: Local *Nui* along the *z* axis for the tall geometry (*Ar* = 8).

In conclusion, the increase of *Rd* increases the conduction effects of the system. The experiment varying *Rd* values for *Ra* = 1 was conducted for this chapter as well. The results showed that temperature should not increase as *Rd* increases. The temperature rise for all three geometries is pretty significant for bottom heating. This behavior can be attributed to the nature of buoyancy. Since buoyancy is driven in the *z* direction, having a heat flux in the *z* direction increases its effects. Therefore, even though *Rd* is increasing, the effects of convection are much higher for bottom heating compared to

radial heating. For example, the velocities in the flat geometry for bottom heating are about 2.5 times greater than velocities for side heating while all the other conditions are constant.

The maximum temperature increase twice for square and tall geometries compared to the flat one. Generally velocities increase for all three geometries as well. The $\overline{Nu}$ numbers increase by 6.14 for all geometries as *Rd* increases from 1 to 10.

The heat flux for the tall geometry increases the most in the lower region while increasing for the entire inner wall in the flat geometry. Again the best geometry would be between $0.125 \leq z \leq 1$ with highest *Rd* values so that a relatively apparent heat flux can be achieved for a mid to low size wall.

6.2.4 Radius Ratio Analysis

This analysis is conducted for $0.25 \leq Rr \geq 2$. As $Rr = 0.25 \rightarrow 2$, the cavity expands with the isotherms and streamlines expanding proportionally as well. The temperature gradient spreads from covering about 60% of the cavity at $Rr = 0.25$ to covering about 70% at $Rr = 2$. The isotherm patterns follow similar to a tall cavity. Around $z = 0$, the isotherms run diagonally towards the outer boundary then change direction run straight vertically and finally bending towards the outer wall. The 25% of the upper cavity maintains a uniform temperature. The highest temperatures are located on the outer-bottom corner. The maximum temperature rises 10% ($\overline{T}_{max} = 0.69 \rightarrow 0.76$). The streamlines behave in accordance to the isotherms. The fluid rises along the outer wall where the highest temperatures are located. The core of the cell is located in the bottom 25% of the cavity where the highest temperature gradient is found. The flow gets weaker as $z \rightarrow H$ where temperature gradient diminishes. For increase in $Rr =$

0.25 → 2, the *u* velocities above the core decrease 4.5 times. This can be explained by looking at the Nusselt numbers.

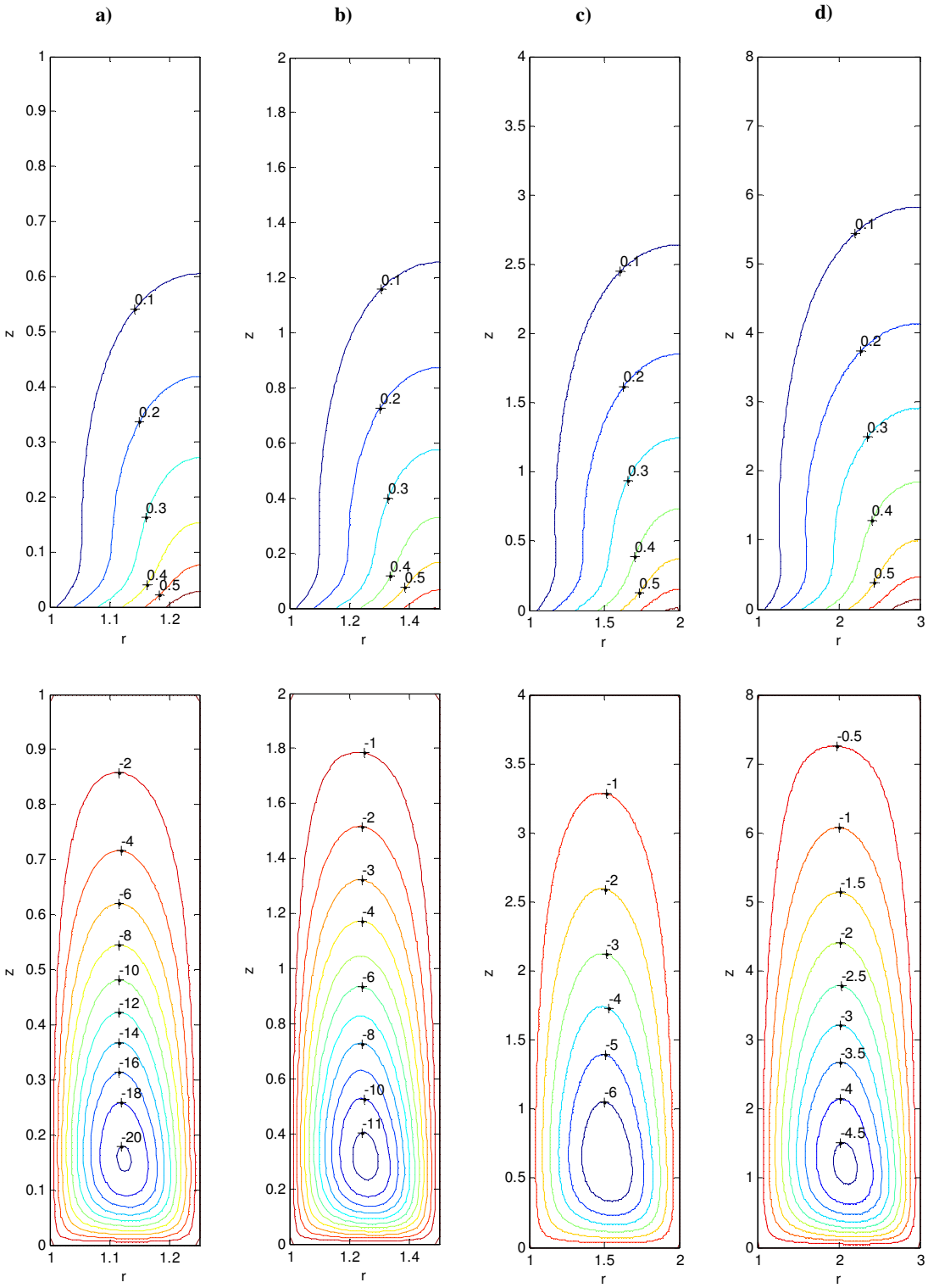

Figure 50: Isotherms and streamlines for a) *Rr* = 0.25; b) *Rr* = 0.5; c) *Rr* = 1; and d) *Rr* = 2.

The inner Nusselt number increases by 80% while $\overline{Nu}_b$ stays constant. As Rr increases, the bottom wall and the height of the annulus increase. Since the heat flux on the bottom wall is controlled, $\overline{Nu}_b$ stays constant. On the other hand, the heat transfer on the bottom wall varies due to the changes in bottom surface area. As a result, $\overline{Nu}_i$ varies in proportion to the changes in the ratio of surface are of the inner wall over the surface are of the bottom wall (A_{in}/A_{bot}) for different Rr values. From $Rr = 0.125 \rightarrow 2$, $\overline{Nu}_i$ increases by 80%. At $Rr = 0.125$, $A_{in}/A_{bot} = 3.55$, while for $Rr = 2$, $A_{in}/A_{bot} = 2$. This indicates that A_{in} decreases relative to A_{bot}. Therefore, $\overline{Nu}_i$ has to increase as A_{in} decreases.

Additionally, the ratio of Nusselt numbers of the inner and bottom walls ($\overline{Nu}_i/\overline{Nu}_b$) is inversely proportional to A_{in}/A_{bot}. As $Rr = 0.125 \rightarrow 2$, $\overline{Nu}_i$ goes from 28% → 50% of $\overline{Nu}_b$ value. While A_{in}/A_{bot} = 71% → 50% .

Overall, variations in Rr change $\overline{Nu}_i$ while keeping $\overline{Nu}_b$ constant. Although this is a desired property, it involves a change in annulus size which can be hard to accomplish in applications.

6.2.6 Conclusion

The original and modified Rayleigh-Bénard problems demonstrate the effect of conduction and convection very clearly. The variation in Rayleigh is directly related to the convection effects while Rd is related to conduction. The modified Rayleigh-Bénard problem shows that adding a heat flux on the bottom leads to lower temperatures. The increase in Rd brings negligible change in ΔT and Ra lowered the maximum temperatures by 33%.

The Rayleigh-Bénard problems provide a good understanding of the basic concepts at play in the main bottom heating analysis. The variations in Ar have no effect on the average bottom Nusselt number but have a big effect on $\overline{Nu}_i$. The effect on $\overline{Nu}_i$ is due to the change height of the inner wall. Since the heat flux and the area of the bottom wall remain constant, $\overline{Nu}_b$ and *En* remain constant. The maximum temperature is the highest for the flat cavity and reduces as Ar increases.

The increase of *Ra* has very similar results for all three geometries. The temperatures in all three geometries decrease by the same percentage. The velocities increase for all three geometries. The Nusselt numbers remain relatively constant for all boundaries in the respective geometry. The effects of convection are apparent for all three geometries as *Ra* is increased to 1000. The local heat flux increases the most for the tall geometry due to the expansion of the flow vertically in the tall geometry.

The increase of *Rd* increases the conduction effects of the system. There is a significant rise in temperatures for all three geometries. This behavior is due to convection effects described in the section. The maximum temperatures increase twice for square and tall geometries compared to the flat one. Generally velocities increase for all three geometries as well. The $\overline{Nu}$ numbers increase by 6.14 for all geometries as *Rd* increases from 1 to 10. The heat flux for the tall geometry increases the most in the lower region while increasing for the entire inner wall in the flat geometry.

Chapter 7: Conclusion

In conclusion, this study analyzes the effects of changing the system characteristics of a porous annulus with an incident external heat flux on its outer boundaries. The effects of physical dimensions, convection, and conduction effects are tested for side and bottom heat flux orientations. The conclusions of each chapter are provided below.

7.1 Chapter 1 and 2

The characteristics and functions of a solar tower power system are presented. It is reported that there are four main ways to increase the solar power tower capacity. This study focuses on increasing the receiver dimensions through the use of porous media. The motivation of the study is to vary the system characteristics and observe their effects on the local heat flux output.

The literature review shows that there have been many studies on side heating annuli with isothermal walls. The papers presented include studies on the effects of convection, radiation, and conduction on porous annuli with side heating. Overall, there are not many studies that incorporate a fixed heat flux for steady state conditions while considering convection and radiation effects.

To the best of the author's knowledge, unlike the side heating, there are even less papers on bottom heating for porous vertical annuli. Most of the papers presented are for clear fluid rectangular or annular geometries, while the porous media studies only consist of rectangular cavities heated from below.

7.2 Chapter 3 and 4

These chapters present the details of the research setup. A vertical cylindrical porous annulus is studied with a heat flux on either the outer boundary or the bottom boundary. The continuity, momentum, and energy equations based on Darcy's law and Boussinesq approximation. The equations are non-dimensionalized and the non-dimensional parameters: *Ar*, *Rr*, *Ra*, and *Rd*, are used in the analysis. The sample solid and fluid materials chosen for the porous media system are aluminum and air respectively.

7.3 Chapter 5

This chapter studies the effects of *Ar*, *Rr*, *Ra*, and *Rd* on the heat transfer in a vertical annulus with heat flux incident on the outer side wall. The summary of the effects of each variable is presented below.

The *Ar* analysis shows that the heat transfer increases as *Ar* increases. The highest heat transfer occurs at $Ar = 10$. Additionally there is no effect of *Ar* on the average Nusselt numbers. Low *Ar* values ($Ar \leq 1$) show high conduction effects. The maximum temperature is lowest for the square geometry and increase for tall and flat geometries.

The Rayleigh number directly controls the convection of the system. The velocities increase as *Ra* increases. The tall and square geometries show a great increase in heat flux due to buoyancy effects. The flat geometry is not much affected by *Ra*.

The Radiation parameter controls the conduction effects in the system. The isotherms become parallel to the outer wall. The velocities tend to decrease since conductive

heat transfer begins to increase. The tall and flat geometries are most affected by high *Rd* values. The square geometry has a mix of convection and conduction present.

The increase in *Rr* causes the entire cavity to expand. The average inner Nusselt number increases while $\overline{Nu}_b$ remains constant with the increase in *Rr*. This is a very desirable property for the system to work efficiently. Unfortunately this cannot be easily accomplished physically.

Finally some general observations for this experiment are mentioned. The local heat flux is always high for the top region of the inner wall due to buoyancy effects. The heat transfer coefficient changes the same as *Nui*. Therefore it is understood that high heat flux regions have a higher *h*. The average *MFR* number is in direct relation to *En* number. Locally, *MFR* behaves similarly to the local Nusselt number. This means the mass flow rate can be high at certain regions of the annulus and can decrease in other regions similar to *Nui*.

7.4 Chapter 6

The orientation of the incident heat flux is changed to the bottom surface. This chapter begins with a description of benchmark solutions then proceeds to describe the effects of each parameter on the heat transfer with bottom heating.

The Rayleigh- Bénard problem demonstrates that the variation in Rayleigh number is directly related to the convection effects while *Rd* is related to conduction.

Additionally, the modified Rayleigh Bénard problem shows that adding a heat flux on the bottom leads to lower temperatures. The increase in *Rd* brings negligible change in ΔT while *Ra* lowers the maximum temperatures by 33%.

The discussion for the main analysis is conducted for each variable separately. The variations in *Ar* have no effect on the bottom Nusselt number but have a big effect on $\overline{Nu}_i$. Since the heat flux and the area of the bottom wall remain constant, $\overline{Nu}_b$ and *En* remain constant. The maximum temperature is the highest for the flat cavity and reduces as *Ar* increases.

The increase in *Ra* has very similar results for all three geometries. The temperatures in all three geometries decrease by the same percentage. The velocities increase for all three geometries. The average Nusselt numbers remain relatively constant for all boundaries in the respective geometry. The local heat flux increases the most for the tall geometry due to the expansion of the flow vertically in the tall geometry.

The increase in *Rd* shows that the temperatures in all three geometries rise by 10-20%. Generally, velocities increase for all three geometries due to convection effects. The $\overline{Nu}$ numbers increase by 6.14 for all geometries as *Rd* increases from 1 to 10. The heat flux for the tall geometry increases the most in the lower region of the inner wall.

It should be noted that maximum temperatures are always located at the outer bottom corner. The *MFR* behaves in the same way as in the previous chapter.

7.5 Comparison

This analysis compares the two heating orientations to see the difference between each other. The observations show that unlike side heating, the bottom heating causes the temperatures to drop significantly. This is due to the difference in surface areas of the heated walls in both orientations and the nature of buoyancy. The heated surface area for bottom heating is 6 times bigger than the surface area for side heating.

Additionally, the effect of buoyancy is naturally in the vertical direction defying gravity. Therefore higher buoyancy effects are experienced in bottom heating leading to lower temperatures. This is evident by the fact that velocities are about 2.5 times greater for bottom heating compared to side heating.

7.6 Future Work

This study analyzed the heat transfer within a vertical cylindrical porous annulus with an external heat flux. A few recommendations are provided for furthering this research in developing an accurate model for a solar power tower receiver system.

The main work that needs to be done after this study is to test all the results in an experimental setup. Either new or provided sample values could be chosen to test the effects of *Ar*, *Ra*, *Rd*, and *Rr*.

Numerically, this study can be extended to study the combined effects of side and bottom heating on a single annulus. This will provide further understanding on how heating both surfaces can be utilized in capturing heat from heliostats.

A transient analysis would also help in studying when the system reaches steady state. It is suspected that different geometries will reach steady state in different time. Since this system works on a limited time scale per day, those results could be invaluable to making this system more efficient.

Appendix A: Nomenclature

A_r	Aspect Ratio…….…..	H/L	Rd	Radiation Parameter	
c_p	Specific Heat……..……	J Kg^{-1} K^{-1}	Rr	Radius Ratio……..	L/r_i
dp	Pore Size…….	m	r,z	Cylindrical Coordinates…….	m
En	Energy Number		$\bar{r},\bar{z}$	Non-dimensional Coordinates	
g	Gravity……...	m s^{-2}	T	Dimensional Temperature……..	K
H	Height of cylinder…….…….	m	$\bar{T}$	Non-Dimensional Temperature	
h	Heat Transfer Coefficient	W m^{-2} K^{-1}	u,w	Velocity in r and z directions.....	m s^{-1}
h_{fg}	Evaporation Enthalpy…….	KJ Kg^{-1}	$\bar{u},\bar{w}$	Non-dimensional velocity	
K	Permeability of Porous Media	m^2		**Greek Symbols**	
k	Thermal Conductivity……	W m^{-1} K^{-1}	α	Thermal Diffusivity……..	m^2 s^{-1}
kp	Porous Media (k)……..	W m^{-1} K^{-1}	β_t	Coefficient of Thermal Expansion	K^{-1}
L	Characteristic Length *(ro-ri)*..	m	β_R	Absorption Coefficient…….….	m^{-1}
$\dot{m}$	Mass Flow Rate…….....	Kg s^{-1}	ρ	Density…….…….	Kg m^{-3}
MFR	Non-Dimensional $\dot{m}$		ε	Viscous Dissipation Parameter	
$\overline{Nu}$	Average Nusselt Number		μ	Viscosity…….	Kg m s^{-1}
Nu	Local Nusselt Number		φ	Porosity	
PPI	Pores Per Inch		ν	Coefficient of Kinematic Viscosity	m^2 s^{-1}
Q	Dimensional Energy Transfer	Kg m^2 s^{-2}	σ	Stephan Boltzmann Constant..…..	$Wm^{-2}K^{-4}$
$q"$	Dimensional Heat Flux……...	Kg s^{-3}	ψ	Dimensional Stream Function	m^2 s^{-1}
q_r	Radiation Flux……..	Kg s^{-3}	$\bar{\psi}$	Non-Dimensional Stream Function	
$\bar{q}$	Non-Dimensional Heat Flux		χ	Dummy variable	
Ra	Rayleigh Number				

Subscripts

∞	Conditions at Outer Radius
c	Cold
f	Fluid
h	Hot
i,in	Inner Wall
o,out	Outer Wall
t,top	Top Wall
b, bot	Bottom Wall
w	Wall

Appendix B: Derivation

The continuity, momentum, and energy equations are derived in this section. For simplicity the equations are solved in Cartesian coordinates and vector form. Only the final equations are expanded and expressed in polar coordinates as used in the text.

B.1 Continuity equation:

The continuity equation in its general form without any modifications is

$$\nabla \cdot \bar{u} = 0$$

where $\bar{u}$ is the velocity in vector form. The expanded equation looks like

$$\frac{\partial(u)}{\partial x} + \frac{\partial(v)}{\partial y} = 0$$

In polar coordinates the equation looks like

$$\frac{\partial(ru)}{\partial r} + \frac{\partial(rw)}{\partial z} = 0$$

B.2 Derivation of momentum equation for porous media.

The momentum equation can be solved by using both the Darcy model and the Boussinesq approximation [16]. The Darcy flow for the *x* and *y* velocities, respectively, can be expressed as:

$$u = -\frac{K}{\mu}\frac{dP}{dx}$$

$$v = -\frac{K}{\mu}\left(\frac{dP}{dy} - \rho g\right)$$

where $\frac{dP}{dx}$ and $\frac{dP}{dy}$ represent the pressure gradients in the x and y directions, respectively [3].

The Boussinesq approximation is defined as

$(\rho_\infty - \rho) \approx \rho\beta(T - T_\infty)$

It is the measure of the amount by which the density changes in response to a change in temperature at constant pressure [8].

The $-\rho g$ term represents [33] the body (buoyancy) forces in the y direction. By applying the curl operator to both sides of Darcy's law, thus removing the explicit dependence on the pressure field [33], the momentum equation can be expressed as:

$$\frac{du}{dy} - \frac{dv}{dx} = -\frac{g\beta K}{\nu}\frac{dT}{dx}$$

In polar coordinate system the momentum equation is expressed as:

$$\frac{\partial(w)}{\partial r} - \frac{\partial(u)}{\partial z} = \frac{gK\beta}{\nu}\frac{\partial T}{\partial r}$$

B.3 Derivation of the energy equation for porous media.

The basic governing energy equation is

$\rho c_p \bar{u} \cdot (\nabla \cdot T) = \nabla \cdot (k\nabla \cdot T) + \nabla \cdot (\bar{q}_r) + \varphi + \dot{q}$

where $\dot{q}$ is the heat generation within the cavity, q_r is the isotropic energy from radiation, and φ is the coefficient for viscous dissipation.

B.3.1 Viscous Dissipation

Viscous dissipation gives the rate at which mechanical energy is converted into heat in a viscous fluid due to friction against the porous material [26].

$\varphi = \bar{u} \cdot \bar{F}$

where $\bar{u}$ is the velocity vector, $\bar{F}$ is the Darcy force vector caused by the porous media and defined as:

$$\bar{F} = \mu K^{-1} \cdot (\bar{u})$$

where μ is the viscosity, K is the permeability of the porous medium, and again $\bar{u}$ is the velocity vector. Combining the above equations leads to an updated viscous dissipation term which takes the form:

$$\varphi = \mu K^{-1} \bar{u}^2$$

Finally the basic energy equation modified to account for Darcy flow and viscous dissipation can be expressed as:

$$\rho C_p \bar{u} \nabla T = \nabla \cdot (k \nabla \cdot T) + \nabla \cdot (\bar{q}_r) + \mu K^{-1} \bar{u}^2 + \dot{q}$$

B.3.2 Radiation

The thermal radiation within the porous solid is accounted in the energy equation through the radiation term. The term q_r is derived using the Rosseland approximation [16]:

$$\overline{q_r} = -\frac{4\sigma}{3\beta_R} \nabla \cdot T^4$$

Where σ is the Stephan Boltzmann constant and β_R is the absorption coefficient. The T^4 can be expanded using Taylor series expansion.

$$T^4 \approx 4TT_\infty^3 - 3T_\infty^4$$

Therefore $\overline{q_r}$ becomes

$$\overline{q_r} = -\frac{4\sigma}{3\beta_R} 4T_\infty^3 (\nabla \cdot T), \qquad and \qquad \nabla \cdot q_r = -\frac{4\sigma}{3\beta_R} 4T_\infty^3 (\nabla \cdot \nabla \cdot T)$$

By incorporating $\overline{q_r}$, the equation becomes

$$\rho C_p \bar{u} \nabla T = \nabla \cdot (k \nabla \cdot T) - \frac{4\sigma}{3\beta_R} 4T_\infty^3 (\nabla \cdot \nabla \cdot T) + \mu K^{-1} \bar{u}^2 + \dot{q}$$

B.3.3 Final Energy Equation

The equation is simplified by dividing ρc_p. The material has isotropic thermal conductivity and there is no heat generation in the cavity so $\dot{q}$ is cancelled out. Therefore the energy equation for porous media is express as:

$$\left(u\frac{\partial T}{\partial x}+v\frac{\partial T}{\partial y}\right)=\alpha\left(\frac{\partial^2 T}{\partial x^2}+\frac{\partial^2 T}{\partial y^2}\right)-\frac{4\sigma}{3\beta_R\rho c_p}4T_\infty^3\left(\frac{\partial^2 T}{\partial x^2}+\frac{\partial^2 T}{\partial y^2}\right)++\frac{\mu}{K}(u^2+v^2)$$

In polar coordinates the energy equations can be expressed as:

$$u\frac{\partial T}{\partial r}+w\frac{\partial T}{\partial z}=\alpha\left(\frac{1}{r}\frac{\partial}{\partial r}\left(r\frac{\partial T}{\partial r}\right)+\frac{\partial^2 T}{\partial z^2}\right)-\frac{4\sigma}{3\beta_R\rho c_p}4T_\infty^3\left(\frac{1}{r}\frac{\partial}{\partial r}\left(r\frac{\partial T}{\partial r}\right)+\frac{\partial^2 T}{\partial z^2}\right)$$
$$+\frac{\mu}{K\rho_o c_p}(u^2+w^2)$$

B.4 Derivation of Boundary Conditions

The only two boundary conditions that are of importance are the adiabatic and heat flux conditions. The rest are of constant temperature. The variable χ is used as a dummy variable for the respective axis that the boundary condition is being applied to

B.4.1 Adiabatic Boundary Condition

$$k\frac{\partial T}{\partial \chi}=0$$

B.4.2 Heat Flux Boundary Condition

The incident heat flux on the boundary is equated to condition and radiation within the porous region.

$$q"=-k\frac{\partial T}{\partial \chi}+q_r$$

Expand q_r

$$q" = -k\frac{\partial T}{\partial \chi} - \frac{4\sigma}{3\beta_R \rho c_p} 4T_\infty^3 \frac{\partial T}{\partial \chi}$$

$$q" = \left(-k - \frac{4\sigma}{3\beta_R \rho c_p} 4T_\infty^3\right)\frac{\partial T}{\partial \chi}$$

$$\frac{q"}{\left(-k - \frac{4\sigma}{3\beta_R \rho c_p} 4T_\infty^3\right)} = \frac{\partial T}{\partial \chi}$$

Appendix C: Non-Dimensionalization

The derived continuity, momentum, and energy equations are non-dimensionalized using following the steps below.

C.1 Non-Dimensional variables

Following non-dimensional variables are established.

$$\bar{r} = \frac{r}{L}; \qquad \bar{z} = \frac{z}{L}; \qquad \bar{\psi} = \frac{\psi}{\alpha L}; \qquad \bar{T} = \frac{(T - T_c)}{(\Delta T)}; \qquad \Delta T = \frac{q"L}{k\left(1 + \frac{4}{3}R_d\right)}$$

C.2 The Continuity Equation

The continuity equation is only used to derive the momentum equation. It is not used in the coding process.

$$\frac{\partial(ru)}{\partial r} + \frac{\partial(w)}{\partial z} = 0$$

Continuity equation is satisfied by introducing the stream function:

$$u = -\frac{1}{r}\frac{\partial \psi}{\partial z}; \qquad\qquad w = \frac{1}{r}\frac{\partial \psi}{\partial r}$$

C.3 The Momentum Equation

$$\frac{\partial(w)}{\partial r} - \frac{\partial(u)}{\partial z} = \frac{gK\beta}{\nu}\frac{\partial T}{\partial r}$$

The momentum equation can be solved by plugging in for *u* and *w*.

$$\frac{\partial}{\partial r}\left(\frac{1}{r}\frac{\partial \psi}{\partial r}\right) + \frac{\partial}{\partial z}\left(\frac{1}{r}\frac{\partial \psi}{\partial z}\right) = \frac{gK\beta}{\nu}\frac{\partial T}{\partial r}$$

Non dimensionalize using the above non-dimensional parameters

$$\frac{\partial}{\partial \bar{r}L}\left(\frac{1}{\bar{r}L}\frac{\partial \bar{\psi}\alpha L}{\partial \bar{r}L}\right) + \frac{\partial}{\partial \bar{z}L}\left(\frac{1}{\bar{r}L}\frac{\partial \bar{\psi}\alpha L}{\partial \bar{r}L}\right) = \frac{gK\beta_T}{\nu}\frac{\partial \bar{T}\Delta T}{\partial \bar{r}L}$$

Simplify to extract non dimensional variable

$$Ra = \frac{gK\beta_T \Delta T L}{\nu\alpha}$$

The final momentum equation:

$$\frac{\partial}{\partial \bar{r}}\left(\frac{1}{\bar{r}}\frac{\partial \bar{\psi}}{\partial \bar{r}}\right) + \frac{\partial}{\partial \bar{z}}\left(\frac{1}{\bar{r}}\frac{\partial \bar{\psi}}{\partial \bar{r}}\right) = Ra\frac{\partial \bar{T}}{\partial \bar{r}}$$

C.4 The Energy Equation

$$u\frac{\partial T}{\partial r} + w\frac{\partial T}{\partial z} = \alpha\left[\frac{1}{r}\frac{\partial}{\partial r}\left(r\frac{\partial T}{\partial r}\right) + \frac{\partial^2 T}{\partial z^2}\right] - \frac{1}{\rho c_p}\left[\frac{1}{r}\frac{\partial}{\partial r}(rq_r) + \frac{\partial}{\partial z}(q_z)\right] + \frac{\mu}{K\rho_o c_p}(u^2 + w^2)$$

Similar to the momentum equation, the energy equation can be solved. First, plug in for *u* and *w*.

$$-\frac{1}{r}\frac{\partial \psi}{\partial z}\frac{\partial T}{\partial r} + \frac{1}{r}\frac{\partial \psi}{\partial r}\frac{\partial T}{\partial z} = \alpha\left[\frac{1}{r}\frac{\partial}{\partial r}\left(r\frac{\partial T}{\partial r}\right) + \frac{\partial^2 T}{\partial z^2}\right] - \frac{1}{\rho c_p}\left[\left(\frac{q_r}{r}\right) - \frac{\partial q_r}{\partial r} - \frac{\partial q_z}{\partial z}\right] + \frac{\mu}{K\rho_o c_p}\left[\left(-\frac{1}{r}\frac{\partial \psi}{\partial z}\right)^2 + \left(\frac{1}{r}\frac{\partial \psi}{\partial r}\right)^2\right]$$

Plug in q_r and non-dimensionalize the equation using the above non-dimensional parameters.

$$\frac{1}{\bar{r}L}\left[\frac{\partial\bar{\psi}\alpha L}{\partial\bar{r}L}\frac{\partial\bar{T}\Delta T}{\partial\bar{z}L}-\frac{\partial\bar{\psi}\alpha L}{\partial\bar{z}L}\frac{\partial\bar{T}\Delta T}{\partial\bar{r}L}\right]$$

$$=\alpha\left[\frac{1}{\bar{r}L}\frac{\partial\bar{T}\Delta T}{\partial\bar{r}L}+\frac{\partial^2\bar{T}\Delta T}{\partial\bar{r}^2L^2}+\frac{\partial^2\bar{T}\Delta T}{\partial\bar{z}^2L^2}\right]+\frac{1}{\rho c_p}\frac{1}{\bar{r}L}\left[\left(\frac{4}{3}\right)\left(\frac{4\sigma}{3\beta_R}\right)\frac{\partial\bar{T}\Delta TT_\infty^3}{\partial\bar{r}L}\right]$$

$$+\frac{1}{\rho c_p}\left[\left(\frac{4}{3}\right)\left(\frac{4\sigma}{3\beta_R}\right)\frac{\partial^2\bar{T}\Delta TT_\infty^3}{\partial\bar{r}^2L^2}\right]+\frac{1}{\rho c_p}\left[\left(\frac{4}{3}\right)\left(\frac{4\sigma}{3\beta_R}\right)\frac{\partial^2\bar{T}\Delta TT_\infty^3}{\partial\bar{z}^2L^2}\right]$$

$$+\frac{\mu}{K\rho_o c_p}\left(\frac{1}{\bar{r}^2L^2}\right)\left[\left(\frac{\partial\bar{\psi}\alpha L}{\partial\bar{z}L}\right)^2+\left(\frac{\partial\bar{\psi}\alpha L}{\partial\bar{r}L}\right)^2\right]$$

Simplify to extract non dimensional variables

$$Rd=\frac{4\sigma T_\infty^3}{\beta_R k},\qquad \varepsilon=\frac{\alpha\mu}{\Delta TK\left(\rho c_p\right)_f},$$

Multiply by:

$$-\frac{L^2}{\alpha\Delta T}$$

The non dimensionalized forms for Equations (1) and (2) are

$$\frac{1}{\bar{r}}\left[\frac{\partial\bar{\psi}}{\partial\bar{r}}\frac{\partial\bar{T}}{\partial\bar{z}}-\frac{\partial\bar{\psi}}{\partial\bar{z}}\frac{\partial\bar{T}}{\partial\bar{r}}\right]$$

$$=\left[\frac{1}{\bar{r}}\frac{\partial\bar{T}}{\partial\bar{r}}+\frac{\partial^2\bar{T}}{\partial\bar{r}^2}+\frac{\partial^2\bar{T}}{\partial\bar{z}^2}\right]+\frac{1}{\bar{r}}\left[\left(\frac{4}{3}\right)R_d\frac{\partial\bar{T}}{\partial\bar{r}}\right]+\left[\left(\frac{4}{3}\right)R_d\frac{\partial^2\bar{T}}{\partial\bar{r}^2}\right]$$

$$+\left[\left(\frac{4}{3}\right)R_d\frac{\partial^2\bar{T}}{\partial\bar{z}^2}\right]+\varepsilon\left[\left(\frac{\partial\bar{\psi}}{\partial\bar{z}}\right)^2+\left(\frac{\partial\bar{\psi}}{\partial\bar{r}}\right)^2\right]$$

Final non dimensional energy equation:

$$\frac{1}{\bar{r}}\left[\frac{\partial\bar{\psi}}{\partial\bar{r}}\frac{\partial\bar{T}}{\partial\bar{z}}-\frac{\partial\bar{\psi}}{\partial\bar{z}}\frac{\partial\bar{T}}{\partial\bar{r}}\right]=\left(1+\frac{4}{3}R_d\right)\left[\frac{1}{\bar{r}}\frac{\partial\bar{T}}{\partial\bar{r}}+\frac{\partial^2\bar{T}}{\partial\bar{r}^2}+\frac{\partial^2\bar{T}}{\partial\bar{z}^2}\right]+\varepsilon\left[\left(\frac{\partial\bar{\psi}}{\partial\bar{z}}\right)^2+\left(\frac{\partial\bar{\psi}}{\partial\bar{r}}\right)^2\right]$$

C.5 Boundary Conditions

The boundary conditions are non-dimensionalized:

C.5.1 Adiabatic Boundary Condition

$$k\frac{\partial \bar{T}\Delta T}{\partial \bar{r}L} = 0$$

C.5.2 Heat Flux Boundary Condition

The incident heat flux on the boundary is equated to condition and radiation within the porous region.

$$q" = -k\frac{\partial \bar{T}\Delta T}{\partial \bar{r}L} + q_r$$

$$q" = -k\frac{\partial \bar{T}\Delta T}{\partial \bar{r}L} - \frac{4\sigma}{3\beta_R \rho c_p}4T_\infty^3\frac{\partial \bar{T}\Delta T}{\partial \bar{r}L}$$

$$q" = \left(-k - \frac{4\sigma}{3\beta_R \rho c_p}4T_\infty^3\right)\frac{\partial \bar{T}\Delta T}{\partial \bar{r}L}$$

Plug in the Radiation constant derived above:

$$-q" = k\left(1 + \frac{4}{3}R_d\right)\frac{\partial \bar{T}\Delta T}{\partial \bar{r}L}$$

$$-\frac{q"L}{k\Delta T}\frac{1}{\left(1 + \frac{4}{3}R_d\right)} = \frac{\partial \bar{T}}{\partial \bar{r}}$$

The non-dimensional flux constant is extracted

$$\bar{q} = \frac{q"L}{k\Delta T}\frac{1}{\left(1 + \frac{4}{3}R_d\right)}$$

Final non-dimensional flux boundary condition

$$-\bar{q}" = \frac{\partial \bar{T}}{\partial \bar{r}} = -1$$

C.6 Nusselt and Energy Number

The Nusselt numbers for the isothermal and the incident heat flux boundary are derived here.

C.6.1 Isothermal Wall

The inner wall is kept at a constant temperature T_c throughout the experiment. The outside environment temperature is T_{∞}.

$$h(T_{in} - T_{\infty}) = -k_{eff}\left(\frac{\partial T}{\partial r}\right)$$

This equation does not work since T_c and T_{∞} are always constant. Since non-dimensionalization is conducted for (T_{∞}- T_c). Therefore T_c and T_{∞} are switched so that $\bar{T}_{\infty}$ can be changed. The new equation is:

$$-h(T_{\infty} - T_c) = -k_{eff}\left(\frac{\partial T}{\partial r}\right)$$

Therefore

$$\frac{h(T_{\infty} - T_c)}{k} = \left(1 + \frac{4Rd}{3}\right)\left(\frac{\partial T}{\partial r}\right)$$

The equation is non-dimensionalized through the previous definitions. A new definition is derived for the difference in the temperature of the isothermal wall and the environment:

$$\bar{T}_{\infty} = \frac{(T_{\infty} - T_c)}{\Delta T}$$

Therefore:

$$h(\Delta T\bar{T}_{\infty}) = k_{eff}\left(\frac{\partial \bar{T}}{\partial \bar{r}}\right)\left(\frac{\Delta T}{L}\right)$$

Finally the local Nusselt number equation is:

$$Nui = \frac{hL(\bar{T}_\infty)}{k} = \left(1 + \frac{4Rd}{3}\right)\left(\frac{\partial \bar{T}}{\partial \bar{r}}\right)$$

This equation can be averaged over the entire wall for an average Nusselt number $\overline{Nu_i}$.

$$\overline{Nu_i} = \frac{hL(\bar{T}_\infty)}{k} = \frac{\int_0^{Ar}\left(1 + \frac{4Rd}{3}\right)\left(\frac{\partial \bar{T}}{\partial \bar{r}}\right)dz}{Ar}$$

C.6.2 Heat Flux Wall

The Nusselt number for the heat flux boundary is derived differently since the temperature difference at the boundary represents the incoming heat flux.

$$\mathrm{h}(T_\infty - T_\mathrm{h}) = -k_{eff}\left(\frac{\partial \bar{T}}{\partial \bar{\chi}}\right)$$

Where χ represents the respective axis for the boundary and λ represents the axis orthogonal to χ . While λ_{ratio} is the aspect ratio for that axis. Since we can control the heat flux going into the cavity we can have:

$$\bar{q} = \frac{(T_\infty - T_\mathrm{h})}{\Delta T}$$

And since the non-dimensional heat flux = -1:

$$\mathrm{h}\Delta T = k_{eff}\left(\frac{\partial \bar{T}}{\partial \bar{\chi}}\right)\frac{\Delta T}{L}$$

Which leads to

$$\frac{\mathrm{h}L}{k} = \left(1 + \frac{4Rd}{3}\right)\left(\frac{\partial \bar{T}}{\partial \bar{\chi}}\right)$$

Therefore the local Nusselt number equals

$$Nu_{\chi} = \frac{\mathrm{h}L}{k} = \left(1 + \frac{4Rd}{3}\right)\left(\frac{\partial \bar{T}}{\partial \bar{\chi}}\right)\Big|_{\chi_{wall}} \quad 3.1$$

The average Nusselt number is

$$\overline{Nu}_{\chi} = \frac{\int_0^{\lambda_{ratio}} \left(1 + \frac{4Rd}{3}\right)\left(\frac{\partial \bar{T}}{\partial \bar{\chi}}\right) d\lambda \Big|_{\chi_{wall}}}{\lambda_{ratio}} \quad 3.2$$

C.6.3 Energy Number

The basic energy balance at any wall is:

$$\mathrm{Q} = q"A$$

Where

$$q" = k\frac{\partial T}{\partial r} + q"_r$$

and

$$A = 2\pi r_i \Delta z$$

Expand:

$$\mathrm{Q} = \left(k\frac{\partial T}{\partial r} + q"_r\right) 2\pi r_i \Delta z$$

Non-dimensionalize:

$$\mathrm{Q} = \left(k + \frac{16\sigma T_{\infty}^3}{3\beta_R}\right)\frac{\partial \bar{T}}{\partial \bar{r}}\frac{\Delta T}{L}(2\pi r_i \Delta \bar{z} L)$$

Where

$$\Delta T = \frac{q"L}{k_{eff}} \qquad \text{and} \qquad k_{eff} = k\left(1 + \frac{4Rd}{3}\right)$$

The equation becomes

$$\mathrm{Q} = k\left(1 + \frac{4\mathrm{Rd}}{3}\right)\frac{\partial \bar{T}}{\partial \bar{r}}\frac{\Delta T}{L}(2\pi r_i \Delta \bar{z} L)$$

Expand ΔT and simplify

$$\mathrm{Q} = \frac{\partial \bar{T}}{\partial \bar{r}} q"(2\pi r_i \Delta \bar{z} L)$$

Non-dimensional Energy number

$$En = \frac{\mathrm{Q}}{q"L^2} = \frac{\partial \bar{T}}{\partial \bar{r}} (2\pi r_i \Delta \bar{z})$$

C.6.4 Mass Flow Rate

The mass flow rate of the fluid flowing within the solar tower receiver can be derived using this equation.

$$\dot{m}\mathrm{h}_{fg} = q"A$$

Where

$$q" = k\frac{\partial T}{\partial r} + q"_r$$

$$A = 2\pi r_i \Delta z$$

Expand:

$$\dot{m}\mathrm{h}_{fg} = \left(k\frac{\partial T}{\partial r} + q"_r\right) 2\pi r_i \Delta z$$

Non-dimensionalize

$$\dot{m}\mathrm{h}_{fg} = \left(k + \frac{16\sigma T_\infty^3}{3\beta_R}\right)\frac{\partial \bar{T}}{\partial \bar{r}}\frac{\Delta T}{L}(2\pi r \Delta \bar{z} L)$$

Where

$$\Delta T = \frac{q"L}{k_{eff}} \qquad \text{and} \qquad k_{eff} = k\left(1 + \frac{4Rd}{3}\right)$$

The equation becomes

$$\dot{m}\mathrm{h}_{fg} = k\left(1 + \frac{4\mathrm{Rd}}{3}\right)\frac{\partial \bar{T}}{\partial \bar{r}}\frac{\Delta T}{L}(2\pi r_i \Delta \bar{z} L^2)$$

Simplify

$$\dot{m} = \frac{\partial \bar{T}}{\partial \bar{r}} \frac{q"}{\mathrm{h}_{fg}} (2\pi r_i \Delta \bar{z} L^2)$$

Mass Flow Rate (Non-dimensional number)

$$MFR = \frac{\dot{m}\mathrm{h}_{fg}}{q"L^2} = \frac{\partial \bar{T}}{\partial \bar{r}} (2\pi r_i \Delta \bar{z})$$

Bibliography

[1] **Morton, Oliver.** A New Day Dawning. *Nature.* 2006, Vol. 443, pp. 19-22.

[2] Solar Power and Chemical Energy Systems. *www.solarpaces.org.* [Online] [Cited: April 18, 2011.] www.solarpaces.org/CSP_Technology/docs/solar_tower.pdf.

[3] **Nield, D.A and Bejan, A.** *Convection in Porous Media.* 3rd Edition. New York : Springer-Verlag, 2006.

[4] **Xu, Chang, et al.** Numerical investigation on porous media heat transfer in a solar tower receiver. *Renewable Energy.* 2011, Vol. 36, pp. 1138-1144.

[5] **Kiwan, Suhi and Alzahrany, Mohammed Sabty.** EFFECT OF USING POROUS INSERTS ON NATURAL CONVECTION HEAT TRANSFER BETWEEN TWO CONCENTRIC VERTICAL CYLINDERS. *Numerical Heat Transfer Part A: Applications.* 2007, Vol. 53, 8.

[6] **Prasad, V. and Kulacki, F. A.** Natural Convection in a Vertical Porous Annulus. *Inertanational Journal of Heat and Mass Transfer.* 1984, Vol. 27, 2.

[7] **Jue, T. C.** Analysis of Thermal Convection in a Fluid Saturated Porous Cavity with Inernal Heat Generation. *Heat and Mass Transfer.* 2003, Vol. 40, 1-2, pp. 83-89.

[8] **Incropera, Frank P. and DeWitt, David P.** *Fundamentals of Heat and Mass Transfer.* New York, Ny : Jon Wiley and Sons, Inc.

[9] **Said, M. N.A. and Trupp, A. C.** Laminar Free Convection in Vertical Air Filled

Cavities with Mixed Boundary Conditions. *Chemical Engineering Communications.* 1980, Vol. 5, pp. 93-107.

[10] **Prasad, V. and Kulacki, F. A.** Convective Heat Transfer in a Rectangular Porous Cavity-Effect of Aspect Ratio on Flow Structure and Heat Transfer. *Journal of Heat Transfer.* 1983, Vol. 106, pp. 158-165.

[11] —. Natural Convection in a Rectangular Porous Cavity with Constant Heat Flux on One Vertical Wall. *Journal of Heat Transfer.* 1984, Vol. 106, pp. 152-157.

[12] —. Free Convection Heat Transfer in a Liquid Filled Vertical Annulus. *Jounal of Heat Transfer.* 1985, Vol. 107, pp. 596-602.

[13] **Saeid, Nawaf H. and Pop, I.** Viscous Dissipation Effects on Free Convection in a Porous Cavity. *Internaional Communications Heat Mass Transfer.* 2004, Vol. 31, 5, pp. 723-732.

[14] **Chen, Sheng, et al.** Natural convection and entropy generation in a vertically concentric annular space. *International Journal of Thermal Sciences.* 2010, Vol. 49, pp. 2439-2452.

[15] **Badruddin, Irfan Anjum, et al.** Heat transfer by radiation and natural convection through a vertical annulus embedded in porous medium. *International Communications in Heat and Mass Transfer.* 2006, Vol. 33, pp. 500–507.

[16] **Badruddin, Irfan Anjum, et al.** Effect of viscous dissipation and radiation on natural convection in a porous medium embedded within vertical annulus. *International Journal of Thermal Sciences.* 2007, Vol. 46, pp. 221–227.

[17] **Koschmieder, E. L.** *Benard Cells and Taylor Vortices.* New York, NY : Cambridge University Press, 1993.

[18] **Ahlers, Guenter.** Experiments with Rayleigh-Benard Convection. *Dynamics of Spatiotemporal Structures–Henri Benard Centenary Review.* 2005.

[19] **SILANO1, G., SREENIVASAN, K. R. and VERZICCO4, R.** Numerical simulations of Rayleigh–Benard convection for Prandtl numbers between 1e-1 and 1e4 and Rayleigh numbers between 1e5 and 1e9. *Journal of Fluid Mechanics.* 2010, Vol. 662, pp. 409-446.

[20] **Umla, R., et al.** Roll Convection of Binary Fluid Mixtures in Porous Media. *Journal of Fluid Mechanics.* 2010, Vol. 649, pp. 165-186.

[21] **Sezai, I. and Mohamad, A. A.** Natural convection in a rectangular cavity heated from below and cooled from top as well as the sides. *Physics of Fluids.* 2000, Vol. 12, 2, pp. 432-443.

[22] **Corcione, Massimo.** Effects of the thermal boundary conditions at the sidewalls upon natural convection in rectangular enclosures heated from below and cooled from above. *International Journal of Thermal Sciences.* 2003, Vol. 42, pp. 199-208.

[23] **Saravanan, S. and Sivaraj, C.** Natural convection in an enclosure with a localized nonuniform heat source on the bottom wall. *International Journal of Heat and Mass Transfer.* 2011, Vol. 51, pp. 2820-2828.

[24] **Ganzarolli, Marcelo M. and Milanez, Luiz F.** Natural convection in rectangular enclosures heated from below and symmetrically cooled from the

sides. *International Journal of Heat and Mass Transfer.* 1995, Vol. 38, 6, pp. 1063-1073.

[25] **Sharif, Muhammad A.R. and Mohammad, Taquiur Rahman.** Natural convection in cavities with constant flux heating at the bottom wall and isothermal cooling from the sidewalls. *International Journal of Thermal Sciences.* 2005, Vol. 44, pp. 865-878.

[26] **Kairi, R. R., Murthy, P.V.S. N. and Ng, C. O.** Effect of Viscous Dissipation on Natural Convection in a Non-Darcy Porous Medium Saturated with Non-Newtonian Fluid of Variable Viscosity. *The Open Transport Phenomena Journal.* 2011, Vol. 3, pp. 1 - 8.

[27] **Becker, M., et al.** Theoretical and numerical investigation of flow stability in porous materials applied as volumetric solar receivers. *Solar Energy.* 2006, Vol. 80, pp. 1241-1248.

[28] **Phanikumar, M. S. and Mahajan, R. L.** Non-Darcy natural convection in high porosity metal foams. *International Journal of Heat and Mass Transfer.* 2002, Vol. 45, pp. 3781-3793.

[29] **Loretz, M., et al.** Metallic foams: Radiative properties/comparison between different models. *Journal of Quantitative Spectroscopy & Radiative Transfer.* 2008, Vol. 109, pp. 16-27.

[30] **Rajmani, R. C., et al.** Convective Heat Transfer in Axisymmetric Porous Bodies. *International Journal of Numerical Methods for Heat and Fluid Flow.* 1995, Vol. 5, pp. 829-837.

[31] **Nath, S. K. and Satyamurthy, V. V.** Effect of Aspect Ratio and Radius Ratio on Free Convection Heat Transfer in a Cylindrical Annulus Filled with Porous Media. *HMT C16-85 Proceeding of 8th National Heat and Mass Transfer Conference India.* 1985, pp. 189-193.

[32] **November, M. and Nansteel, M. W.** Natural Convection in Rectangular Enclosures Heated from Below and Cooled Along One Side. *International Journal of Heat and Mass Transfer.* 1987, Vol. 30, 11, pp. 2433-2440.

[33] **Cheng, P. and Minkowycz, W. J.** Free Convection About a Vertical Flat Plate Embedded in a Saturated Porous Medium with Applications to Heat Transfer from a Dike. *Journal of Geophysical Research.* 1977, Vol. 82, 14, pp. 2040-2044.